Impact of sand nourishments on hydrodynamics and swimmer safety

Radermacher, Max

DOI
10.4233/uuid:0816cbe5-4e42-4fd3-a328-4775c5ccb633

Publication date
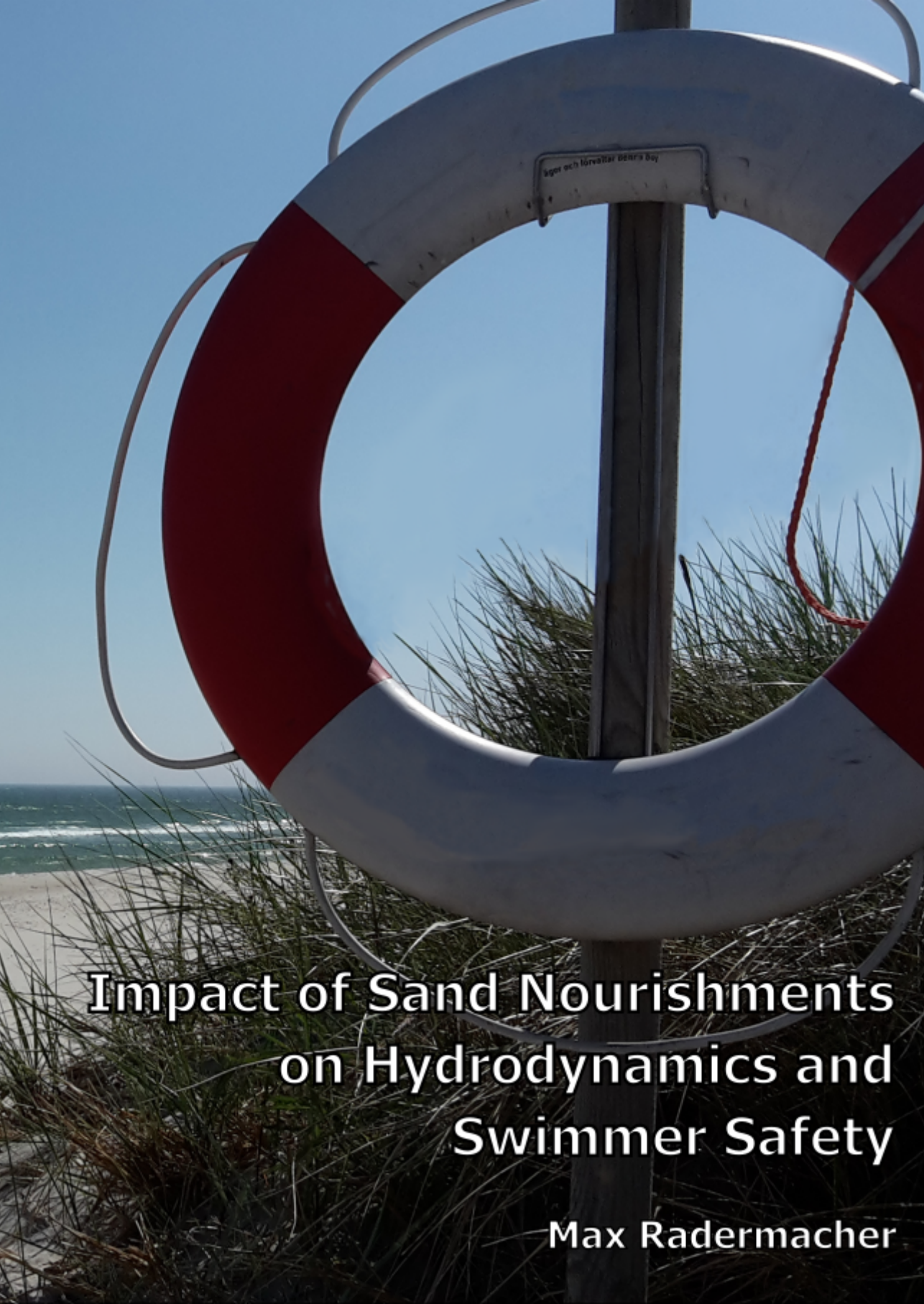2018

Document Version
Final published version

Important note
To cite this publication, please use the final published version (if applicable).
Please check the document version above.

Impact of Sand Nourishments on Hydrodynamics and Swimmer Safety

Max Radermacher

IMPACT OF SAND NOURISHMENTS ON HYDRODYNAMICS AND SWIMMER SAFETY

Dissertation

for the purpose of obtaining the degree of doctor
at Delft University of Technology,
by the authority of the Rector Magnificus, prof. dr. ir. T.H.J.J. van der Hagen,
chair of the Board for Doctorates,
to be defended publicly on
Friday, 15 June 2018 at 15:00 o'clock

by

Max RADERMACHER

Master of Science in Civil Engineering, Delft University of Technology, the Netherlands,
born in Meerssen, the Netherlands

This dissertation has been approved by the promotors.

Composition of the doctoral committee:

Rector Magnificus,	chairperson
Prof. dr. ir. M.J.F. Stive,	Technische Universiteit Delft, promotor
Prof. dr. ir. A.J.H.M. Reniers,	Technische Universiteit Delft, promotor
Dr. ir. M.A. de Schipper,	Technische Universiteit Delft, copromotor

Independent members:

Prof. dr. ir. A.E. Mynett,	Technische Universiteit Delft & IHE Delft
Prof. dr. ir. J.A. Roelvink,	Technische Universiteit Delft & IHE Delft
Prof. dr. G. Masselink,	Plymouth University
Dr. B. Castelle,	Université de Bordeaux
Prof. dr. ir. W.S.J. Uijttewaal,	Technische Universiteit Delft, reserve member

CONTENTS

SUMMARY

Sand nourishments are commonly used to mitigate coastal erosion problems. The ongoing build-up of economic value in coastal areas decreases the capacity of the coastal system to adapt to natural fluctuations in coastline position, while it aggravates the consequences of coastal flooding events. Larger nourishment volumes and longer return periods of nourishments are often suggested as a sustainable solution, resulting in the construction of the Sand Motor in 2011, a 17.5 Mm^3 pilot mega nourishment along the Delfland coast in The Netherlands. It is intended to feed sand to the adjacent coastline by natural sediment transport processes throughout the coming decades.

Sand nourishments in general and mega nourishments in particular have a positive impact on the coastal sediment budget. Their effect on other functions of the coastal zone, such as recreation, is not fully understood yet. The presence of an artificial body of sand at the coastline inevitably interacts with nearshore hydrodynamics, which might result in the formation of flow patterns that pose a risk to swimmers and bathers. An increase of recreational risk due to the implementation of a nourishment project is usually considered unwanted and unacceptable. Therefore, the main objective of this research is to determine and understand how a mega-scale sand nourishment influences nearshore hydrodynamics and thereby affects swimmer safety.

Coastal swimmer safety is associated with the likelihood of drowning of people swimming or bathing in nearshore waters. Measures to enhance coastal swimmer safety rely on prediction of swimmer safety risks, which may occur at different spatial and temporal scales. A swimmer safety risk is defined as the coincidence in space and time of hazardous hydrodynamic phenomena and the presence of beach users. Only if both aspects are present at the same time and location, an actual swimmer safety risk exists. At the Sand Motor, three potentially hazardous hydrodynamic phenomena were identified. (1) The nourishment acts as a perturbation to the alongshore tidal flow at the Dutch North Sea coast, giving rise to contraction and possibly separation of the tidal flow. Offshore directed currents around the most seaward point of the nourishment due to flow separation and eddy generation may form a hazard to swimmers and bathers. (2) Furthermore, tidal pumping in the entrance channel to the artificial Sand Motor lagoon may induce strong tidal currents. (3) Finally, the autonomous morphodynamic evolution of the nourishment might lead to the formation of alongshore variable sandbars, which in turn may lead to rip current generation. Physical hazards number 1 and 3 have been studied in more detail here, while number 2 has been taken into account in a qualitative sense when assessing swimmer safety at the Sand Motor. Addtionally, the performance of an operational rip current prediction system was studied.

The presence and characteristics of subtidal sandbars at the Delfland coast were

examined based on a 52-year bathymetric dataset. Throughout this period, the Delfland coast received over 20 sand nourishments of various types and sizes, allowing for a comparison of the influence of different nourishment types on sandbar evolution. The first 20 years of the dataset represented the unnourished regime, which was characterised by the partial presence of a subtidal sandbar along the Delfland coast. This sandbar slowly migrated offshore at an average rate of 5 m/year and was relatively straight, exhibiting very limited alongshore variability. The introduction of beach nourishments in the system from the 1980s onwards tended to promote subtidal sandbar formation, notably at the previously unbarred central section of the Delfland coast. Subsequently, the implementation of shoreface nourishments induced strong onshore migration of the nourishment (acting as an artificial sandbar), thereby forcing the pre-existing subtidal sandbar to weld onshore. Between 2009 and 2012, an extensive nourishment scheme was executed at the Delfland coast, adding 37.5 Mm^3 of sand to the coastal cell (including the Sand Motor). The pre-existing sandbars and rubble-mound groynes were largely covered by the nourished sand, allowing for the formation of new, relatively shallow subtidal sandbars. These shallow sandbars exhibited a degree of alongshore variability that was unprecedented in the 52-year dataset analysed here. Altogether, these results imply that individual nourishments can influence the formation and migration of individual sandbars, while continued nourishments can fundamentally change long-term sandbar dynamics along an entire coastal cell.

The occurrence of tidal flow separation at mega nourishments of varying size and shape was assessed in a combined field and modelling study. Tidal flow separation and eddy formation were observed at the northern side of Sand Motor during flood flow in 2014 using fixed and ship-mounted acoustic current profilers. The intensity of generated tidal eddies was found to modulate with the spring-neap tidal cycle. A numerical model of tidal currents around mega nourishments of variable size and shape was constructed and validated successfully for the Sand Motor case. It was demonstrated that the occurrence of tidal flow separation and the size and intensity of generated tidal eddies depend on the aspect ratio of the nourishment and the alongshore dimension of the nourishment compared to the tidal excursion. Tidal flow separation does not occur for very smooth nourishment shapes or nourishments that are large compared to the tidal excursion.

Prediction of rip currents with operational numerical models is highly sensitive to the accuracy of the nearshore bathymetry employed in the model. Due to its rapid morphodynamic evolution, nearshore bathymetry should be updated regularly. Theoretically, this can be achieved based on remote sensing techniques employing depth inversion. Here, the sensitivity of modelled rip currents to errors in remotely-sensed bathymetries is studied by comparing model simulations on a remotely-sensed bathymetry to model simulations on a corresponding in-situ surveyed bathymetry. Of all rip currents generated on an in-situ bathymetry, 55% were reproduced on the remotely-sensed bathymetry (true positive rip current predictions), showing that the latter has predictive value. False positive predictions of rip currents on the remotely-sensed bathymetry seldomly occurred. Positive predictions were promoted significantly by accurate reproduction of the pattern and

amplitude of nearshore bars at length scales between 200 and 400 m.

Finally, an assessment of swimmer safety at the Sand Motor was made, employing a generic framework for coastal swimmer safety. The coincidence in space and time of the three hazardous hydrodynamic phenomena and the presence of beach users was determined. At the Sand Motor, beach users tend to cluster in the transition areas between the nourishment and the adjacent coastline as a result of the spatial spreading of beach facilities. This leads to a low spatial coincidence of beach users and offshore currents due to tidal flow separation, since these currents occur around the most seaward point of the Sand Motor. In turn, the risk of rip current generation over subtidal sandbars is present along the entire coastline and therefore coincides in space with the presence of beach users. However, wave breaking over subtidal sandbars (potentially driving rip currents) only occurs if the wave height on top of the bar crest is sufficiently high. At the marginal Dutch North Sea coast, most waves are generated locally, which makes high waves typically coincide with unpleasant weather conditions. Therefore, a negative correlation exists between wave height and beach attendance, leading to a low temporal coincidence of rip currents generated over subtidal sandbars and beach users at the Dutch coast. This coincidence can be significantly higher at open ocean coasts with a swell wave climate. Tidal pumping and the associated tidal currents in the entrance channel of the lagoon constitute the highest swimmer safety risk at the Sand Motor, due to their high spatial and temporal coincidence with beach attendance. Nevertheless, the physical hazard associated with this phenomenon varies in time due to the autonomous morphodynamic evolution of the entrance channel. The generic framework for coastal swimmer safety put forward in this thesis proved to be a useful method to create an overview of swimmer safety risks at a particular beach or nourishment project. It allows for a qualitative comparison of the risks associated with various hazardous hydrodynamic phenomena at the Sand Motor. It is expected that the framework is a valuable tool during the design and evaluation stages of coastal interventions.

SAMENVATTING

Zandsuppleties worden veelvuldig gebruikt voor de bestrijding van kusterosieproblematiek. De voortgaande opbouw van economische waarde in kustgebieden vermindert de capaciteit van het kustsysteem om natuurlijke fluctuaties in kustlijnpositie te absorberen, terwijl het de gevolgen van kust-gerelateerde overstromingen verergert. Grotere suppletievolumes en een langere terugkeertijd van suppleties worden vaak genoemd als duurzame oplossing voor dit probleem, wat heeft geresulteerd in de aanleg van de Zandmotor in 2011, een pilot mega-suppletie van 17.5 Mm^3 langs de Delflandse kust in Nederland. De Zandmotor moet gedurende de komende decennia gaan dienen als een bron van zand voor de aangrenzende kustlijn.

Zandsuppleties, en mega-suppleties in het bijzonder, hebben een positief effect op het sedimentbudget van de kust. Hun invloed op andere functies van de kustzone, zoals recreatie, is tot op heden veel minder bekend. Het is onvermijdelijk dat de aanwezigheid van een artificieel zandlichaam aan de kustlijn interacteert met hydrodynamica in de ondiepe kustzone, wat mogelijkerwijs leidt tot de vorming van stromingspatronen die gevaarlijk zijn voor zwemmers en baders. Een toename van risico's voor de zwemveiligheid als gevolg van de aanleg van een zandsuppletie is doorgaans ongewild en onacceptabel. Het hoofddoel van dit onderzoek is daarom het bepalen en begrijpen van de invloed van mega-suppleties op hydrodynamica in de ondiepe kustzone en het effect dat dit heeft op de zwemveiligheid.

Kustzwemveiligheid is gerelateerd aan de waarschijnlijkheid dat zwemmers en baders verdrinken in ondiepe kustwateren. Manieren om de zwemveiligheid te verbeteren zijn gebaseerd op het voorspellen van zwemveiligheidsrisico's, die zich op verschillende tijds- en lengteschalen kunnen manifesteren. Een zwemveiligheidsrisico is gedefinieerd als het samenvallen in ruimte en tijd van gevaarlijke hydrodynamische verschijnselen en de aanwezigheid van strandgebruikers. Slechts wanneer beide aspecten tegelijkertijd op dezelfde plek aanwezig zijn, is er sprake van een daadwerkelijk zwemveiligheidsrisico. Op de Zandmotor kunnen drie potentieel gevaarlijke stromingsverschijnselen worden onderscheiden. (1) De suppletie vormt een obstakel voor de kustlangse getijstroom aan de Nederlandse Noordzeekust, wat kan leiden tot contractie en loslating van de getijstroom. Zeewaarts gerichte stromingen rond het verst uitstekende punt van de suppletie als gevolg van stromingsloslating en neervorming kunnen een gevaar vormen voor zwemmers en baders. (2) Daarnaast kan de getijslag in de artificiële lagune op de Zandmotor sterke getijstroming in de toegangsgeul van de lagune veroorzaken. (3) Tot slot kan de autonome morfodynamische ontwikkeling van de suppletie leiden tot de vorming van kustlangs variabele zandbanken, die op hun beurt in muistromen kunnen resulteren. Stromingsverschijnselen 1 en 3 worden in dit proefschrift in meer detail onderzocht, terwijl stromingsverschijnsel 2 op een kwalitatieve manier wordt meegenomen bij het beoordelen van de totale zwemveiligheid rond de Zandmo-

tor. Daarnaast wordt in dit proefschrift de werking van een operationeel muistroom voorspellingssysteem onderzocht.

The aanwezigheid en karakteristieken van subtidale zandbanken aan de Delflandse kust zijn bestudeerd op basis van een 52-jarige bathymetrische dataset. Gedurende deze periode zijn er meer dan twintig zandsuppleties van uiteenlopende types en afmetingen uitgevoerd aan de Delflandse kust, wat een vergelijking mogelijk maakt van de invloed van verschillende suppletietypes op de ontwikkeling van subtidale zandbanken. De eerste twintig jaar van de dataset representeerden het ongesuppleerde regime, dat werd gekarakteriseerd door de gedeeltelijke aanwezigheid van een subtidale zandbank langs de Delflandse kust. Deze zandbank migreerde langzaam zeewaarts met een gemiddelde migratiesnelheid van 5 m/jaar, was relatief recht en had een zeer beperkte kustlangse variabiliteit. De introductie van strandsuppleties in het kustsysteem vanaf de jaren 1980 heeft de vorming van subtidale zandbanken bevorderd, vooral langs het voordien bankloze centrale gedeelte van de Delflandse kust. In de periode daarna leidde de plaatsing van vooroeversuppleties tot een sterke kustwaartse migratie van de suppletie (die als een artificiële zandbank fungeert), waardoor de reeds bestaande zandbank het strand op werd gedrongen. Tussen 2009 en 2012 werd een uitgebreid suppletieprogramma uitgevoerd aan de Delflandse kust, waardoor 37.5 Mm^3 zand aan het kustvak werd toegevoegd (inclusief de Zandmotor). De reeds bestaande zandbanken en stenen strandhoofden werden grotendeels bedekt door het gesuppleerde zand, wat tot de vorming van nieuwe, relatief ondiepe subtidale zandbanken leidde. Deze ondiepe zandbanken hadden een mate van kustlangse variabiliteit die niet eerder vertoond was in de 52-jarige dataset. De resultaten van dit deelonderzoek impliceren dat individuele suppleties de vorming en migratie van individuele zandbanken kunnen beïnvloeden, terwijl herhaaldelijke suppleties een fundamentele verandering in het lange-termijn gedrag van zandbanken in een kustvak kunnen veroorzaken.

Loslating van de getijstroom bij mega-suppleties van variërende vorm en grootte is bestudeerd middels een combinatie van veld- en modelonderzoek. Loslating en neervorming zijn in 2014 waargenomen in de vloedstroming aan de noordzijde van de Zandmotor met vaste en varende akoestische stromingsmeters. De intensiteit van de gevormde neren bleek te variëren met de spring-doodtij cyclus. Een numeriek model van de getijstroming rond mega-suppleties van uiteenlopende vorm en grootte werd opgezet en succesvol gevalideerd met behulp van de veldmetingen bij de Zandmotor. Het werd aangetoond dat het optreden van loslating en de grootte en intensiteit van de gevormde neren afhangen van de lengte-breedte-verhouding van de suppletie en de verhouding van de kustlangse afmeting van de suppletie tot de getijweg. Loslating van de getijstroom komt niet voor wanneer de suppletie een zeer gestroomlijnde vorm heeft en/of wanneer de suppletie erg groot is ten opzichte van de getijweg.

Muistroomvoorspellingen met operationele numerieke modellen zijn erg gevoelig voor de nauwkeurigheid van de gebruikte bodem in de ondiepe kustzone. Vanwege de snelle morfodynamische ontwikkeling in die zone dient de bodem in het operationele model regelmatig te worden vernieuwd. In theorie kan dit worden gedaan door middel van remote sensing technieken die gebruik maken van diepte-

inversie. In dit deelonderzoek is de gevoeligheid van gemodelleerde muistromen op een remote sensing bodem bestudeerd door modelsimulaties op een remote sensing bodem te vergelijken met modelsimulaties op een in-situ gemeten bodem. Van alle muistromen die voorspeld werden op de in-situ bodem, werd 55% gereproduceerd op de remote sensing bodem (terecht positieve muistroomvoorspelling), wat aantoont dat muistroomsimulaties op een remote sensing bodem een voorspellende waarde hebben. Fout-positieve voorspellingen van muistromen op de remote sensing bodem kwamen zelden voor. Positieve voorspellingen werden significant bevorderd door nauwkeurige reproductie van het patroon en de amplitude van zandbanken op lengteschalen tussen de 200 en 400 meter.

Tot slot is een beschouwing gemaakt van de zwemveiligheid rond de Zandmotor, waarbij een generiek kader voor kust-gerelateerde zwemveiligheid werd gebruikt. Het samenvallen in ruimte en tijd van de drie hiervoor genoemede gevaarlijke hydrodynamische verschijnselen en de aanwezigheid van strandgebruikers werd bepaald. Vanwege de ruimtelijke spreiding van strandfaciliteiten op de Zandmotor clusteren strandgebruikers daar in de overgangsgebieden tussen de suppletie en de aangrenzende kust. Daardoor is er een zeer beperkte ruimtelijke overlap tussen strandgebruikers en zeewaarts gerichte stromingen als gevolg van loslating van de getijstroming, aangezien dit verschijnsel zich voornamelijk afspeelt rond het meest zeewaartse punt van de Zandmotor. Het risico van muivorming is daarentegen aanwezig langs het gehele kustvak en heeft daarom een grote ruimtelijke overlap met de aanwezigheid van strandgebruikers. Desalniettemin vindt golfbreking op subtidale zandbanken (en daarmee de potentiële vorming van muistromen) alleen plaats wanneer de golven boven de banktop hoog genoeg zijn. Aan de marginale Nederlandse Noordzeekust worden vrijwel alle golven lokaal opgewekt, waardoor hoge golven doorgaans samenvallen met slecht strandweer. Daarom is er een negatieve correlatie tussen golfhoogte en strandgebruik, wat leidt tot een lage overlap in de tijd van muistromen en de aanwezigheid van strandgebruikers aan de Nederlandse kust. Deze overlap kan een stuk hoger zijn aan open oceaankusten met een golfklimaat dat veel deining bevat. Getijslag in de lagune en de hieraan gerelateerde getijstroming in de toegangsgeul vormen het grootste zwemveiligheidsrisico rond de Zandmotor vanwege het samenvallen in tijd en ruimte van dit verschijnsel met de aanwezigheid van strandgebruikers. De grootte van dit risico verandert echter in de tijd door de autonome morfodynamische ontwikkeling van de toegangsgeul.

Het generieke kader voor kust-gerelateerde zwemveiligheid dat in dit proefschrift werd gebruikt, bleek een nuttige methode te zijn voor het creëren van een overzicht van zwemveiligheidsrisico's rond een speciek strand of suppletieproject. Het stond een kwalitatieve vergelijking toe van risico's die verbonden zijn aan uiteenlopende gevaarlijke stromingsverschijnselen op de Zandmotor. Naar verwachting is het kader een waardevol hulpmiddel bij het ontwerp en de evaluatie van kustinterventies.

1

INTRODUCTION

1

1.1. MOTIVATION

Sand nourishments are a commonly-used method to increase the sediment volume of a beach (Hamm et al., 2002; Hanson et al., 2002). The primary reason for execution of a nourishment is compensation of sand losses from natural beach erosion, although other motivations may exist as well (e.g. enhancement of recreational values of the coast, nature development; Temmerman et al., 2013; De Vriend et al., 2015). Structural erosion of beaches has been observed along many coastlines around the world, well-known examples being a.o. the east coast of Florida (USA; Finkl, 1996), Hoi An (Vietnam; Do et al., 2018), Durban (South Africa; Corbella and Stretch, 2012) and the Belgian, Dutch, German and Danish North Sea coast (De Wolf et al., 1993; Van Rijn, 1997; Kelletat, 1992; Aagaard et al., 2004). A common factor among these coasts is the economic value they represent (tourism, recreation) or defend (dunes as primary sea defence of densely-populated, low-lying hinterland). The tendency of humankind to employ its activities in economically interesting, fertile and tractable, but low-lying coastal areas and river deltas is still increasing at present (Kuenzer and Renaud, 2012). This drastically limits the capacity of the coastal zone to adapt to naturally varying boundary conditions, while it leads to a build-up of economic value that is at risk of coastal flooding (Doody, 2004). The basic morphological cycle of a wave-dominated coastline, consisting of erosion during storm conditions and recovery during periods of fair weather, already requires a certain capacity of the coastal zone to accommodate for variable cross-shore coastline positions, let alone the impact of the slowly but steadily rising mean sea level (Stive et al., 1991; IPCC, 2013) and possible increase in severity of storms (De Winter et al., 2012).

The combination of increasing activity in the coastal zone and climate change asks for the exploration of innovative solutions leading to sustainable coastal management. Larger nourishment volumes and longer return periods of nourishment projects are often suggested (Deltacommissie, 2008; Van Dalfsen and Aarninkhof, 2009). Against this background, a mega-scale beach nourishment was constructed in 2011 as a pilot project at the Dutch North Sea coast, just south of The Hague, along the Delfland coastal cell. This highly-concentrated Sand Motor nourishment (also referred to as Sand Engine, Stive et al., 2013) is 10 to 20 times larger than traditional sand nourishments. It is intended to (partly) compensate erosion losses at the adjacent coastline throughout the coming decades as a result of naturally occurring alongshore transport of the nourished sand.

While sand nourishments in general and mega nourishments in particular are effective measures to increase the coastal sediment budget and thereby enhance safety against flooding (De Schipper et al., 2016), their impact on other functions of the coastal zone is not fully understood yet. The presence of an artificial body of sand at the coastline inevitably interacts with nearshore hydrodynamics, which might result in the formation of flow patterns that pose a risk to swimmers and bathers. At present, it is difficult to predict whether such hazardous hydrodynamic phenomena will occur after construction of a sand nourishment, as studies into this matter are largely absent. Uncertainty about potentially adverse impacts of sand nourishments in practice is one of the main discussion topics surrounding planned

or executed nourishment projects (Van den Hoek et al., 2014b; Bontje and Slinger, 2017). This lack of knowledge often leads to public debate that is dominated by presumption, misunderstanding, feelings and hearsay, unnecessarily damaging public support for nourishment projects. Nevertheless, decent understanding of the potential recreational risks (and ways to mitigate these) of the nourishment should be a strict requirement for any planned nourishment project, as an increase of the recreational risk due to implementation of the project is usually considered unwanted and unacceptable. Therefore, the main objective of this research is to determine and understand how a mega-scale sand nourishment influences nearshore hydrodynamics and thereby affects swimmer safety.

1.2. GENERIC FRAMEWORK FOR COASTAL SWIMMER SAFETY

Although typically associated with leisure and relaxation, swimming in coastal waters can be a dangerous activity. It is estimated that the number of people that drown while bathing or swimming in coastal waters is in the order of 10,000 per year globally (see Appendix A for an overview of statistics related to coastal drowning), while many more casualties are prevented by the operations of lifeguards and other rescue services (Morgan and Ozanne-Smith, 2013; Koon et al., 2017). The causes of coastal drowning are manifold, and hazardous hydrodynamic processes do not necessarily play a primary role in every coastal drowning incident (e.g. exhaustion of an over-confident swimmer). Nevertheless, nearshore flows are a major threat to swimmers and bathers. Globally, most attention is paid to rip currents in this respect, being a primary cause of beach rescue operations along many open ocean coastlines that receive high-energy swell waves. At the Dutch coast however, as De Zeeuw et al. (2012) point out, rip currents are just one out of many hydrodynamic phenomena that are associated with beach rescue operations.

Human interest in coastal swimmer safety is typically associated with the desire to decrease the likelihood of drowning of swimmers and bathers. Measures to achieve this goal can be taken at many different levels. Here, the timeline of coastal drowning is proposed as a central framework to assess the effect of different measures (Figure 1.1). Improving swimmer safety at a particular beach can be achieved by intervening at any point along the timeline, making sure that a swimmer or bather does not reach the final stage of the timeline: drowning.

A person who has decided to visit a beach, is not necessarily visiting a hazardous beach (e.g. with many rip currents, or without a lifeguard station). If the person has knowledge of the safety levels of various nearby beaches (e.g. because such information was disseminated to the public, cf. Short, 2006; Scott, 2009), he/she could decide to avoid hazardous beaches (Figure 1.1, exit A). Likewise, if beaches are strongly influenced by coastal engineering works, engineers could have incorporated swimmer safety considerations into the design process of the intervention, thereby reducing the hazard level of that particular beach. Effectively, this could increase the probability of a person taking exit A on the timeline of drowning. Once the person arrives at the beach, he/she could decide not to swim under hazardous conditions (e.g. because he/she is able to recognise rip current locations, or is informed about hazardous conditions by lifeguards, cf. Sherker et al., 2010; Caldwell

1
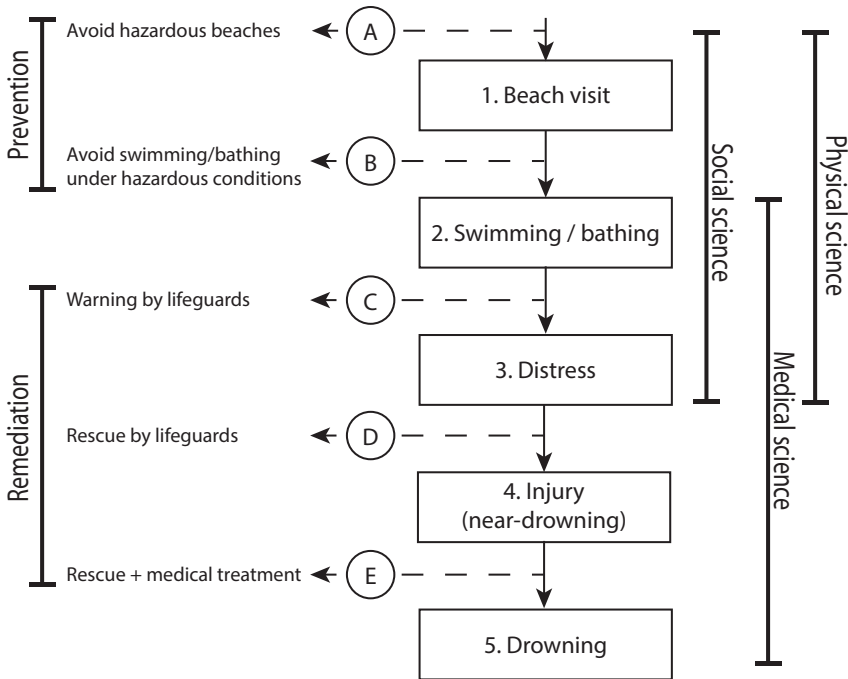
Figure 1.1: The timeline of coastal drowning, consisting of five stages (numbered 1-5) and five exits (A-E).

et al., 2013; Brannstrom et al., 2014; Gallop et al., 2016) (Figure 1.1, exit B). Again, at heavily engineered beaches, coastal engineers could try to reduce the probability of occurrence of hazardous condtions, effectively promoting exit B. Once the person is swimming or bathing, he/she could be warned by lifeguards about potentially hazardous conditions (because lifeguards may be aware of those conditions as a result of their personal experience or due to digital aids, such as nearshore hydrodynamic forecast models, cf. Alvarez-Ellacuria et al., 2010; Voulgaris et al., 2011; Austin et al., 2012) (Figure 1.1, exit C). If the swimming or bathing person is in distress (e.g. because he/she is caught in a strong alongshore current), in many cases he/she must rely on the presence and awareness of lifeguards or other beach users in order to be rescued. It is noted that a person might also be able to escape from a hazardous current independently (e.g. because he/she has been informed about rip current escape strategies, cf. McCarroll et al., 2014; Van Leeuwen et al., 2016; Castelle et al., 2016). The fourth stage of the timeline involves injury due to near-drowning (low body temperature and/or water intake leading to respiratory problems, cf. Tipton and Golden, 2006). Only rescue by lifeguards or other beach users and adequate medical treatment can prevent the victim from drowning (Figure 1.1, exits D and E).

Analysis of swimmer safety and prevention of drowning inherently is a multidisciplinary field of science, comprised of physical, social and medical aspects. Physical and social science play a role in the timeline of coastal drowning between exits

A and D, including the stages of beach visit, swimming/bathing and distress. For a coastal engineer working on projects related to swimmer safety, it is highly important to realise that the involvement of social aspects obstructs an approach that is purely based on physical logic. For example, from a physical viewpoint, determining the optimal escape strategy for a swimmer caught in a rip current implies that any swimmer, if informed about escape strategies, can get back to the beach safely. However, the response of swimmers caught in a rip current is highly variable in practice, depending on the swimmer's knowledge of coastal currents, his/her physical abilities, his/her awareness level and his/her ability to cope with stressful situations. The fact that alcohol consumption plays a significant role in drowning incidents (Driscoll et al., 2004) adds to this complexity. The final stages of the timeline of coastal drowning are purely governed by medical science. Once a swimmer reaches the near-drowning stage, he/she must rely on his/her survival instinct and on the lifesaving and medical abilities of people involved in an eventual rescue operation.

The present study primarily addresses the physical aspects of swimmer safety, while acknowledging the social and medical aspects. In order to quantify the risk of surfzone rescues and drowning, this study will employ the concept of spatio-temporal correspondence of beach users and hazardous hydrodynamic phenomena. Only if beach users and hazardous hydrodynamics coincide (i.e. both are present at the same time and location), an actual risk is established. The spatial component will largely be constrained to the alongshore dimension, similar to the approach of Houser et al. (2015), disregarding the question whether a beach user actually enters the water or not. It is assumed that the number of beach users present at a specific alongshore location is approximately proportional to the number of swimmers and bathers at that location.

Predicting when and where hazardous hydrodynamics and beach user presence will coincide plays a key role in mitigation of recreational risks. Lifeguards and other rescue services make such predictions (typically based on their expert judgment) while planning their daily operations. If a sunny day with an energetic swell is coming up, they can expect a combination of high beach attendance and hazardous surfzone currents and will schedule a large number of lifeguards. While that is a rather trivial example, (un)predictability of swimmer safety can be assessed over a range of spatial and temporal scales (Figure 1.2). Predictability at larger and longer scales plays a role at the level of coastal managers and engineers, for example when they try to minimise the adverse effects of a coastal intervention on swimmer safety. On the other hand, predictability at smaller and shorter scales is related to the level of lifeguard operations, for example when they are deciding which areas to focus on during their hourly beach patrol. Mitigation measures for recreational risks can relate to any of these scales, which is illustrated by the fact that all of the questions posed in Figure 1.2 are reflected in the chapters of this thesis.

Together, the timeline of drowning, the notion of spatio-temporal correspondence of hazardous hydrodynamics and beach users, and the notion of predictability of swimmer safety risks form the generic framework for coastal swimmer safety. The framework will be applied to the case of mega-scale beach nourishments in this
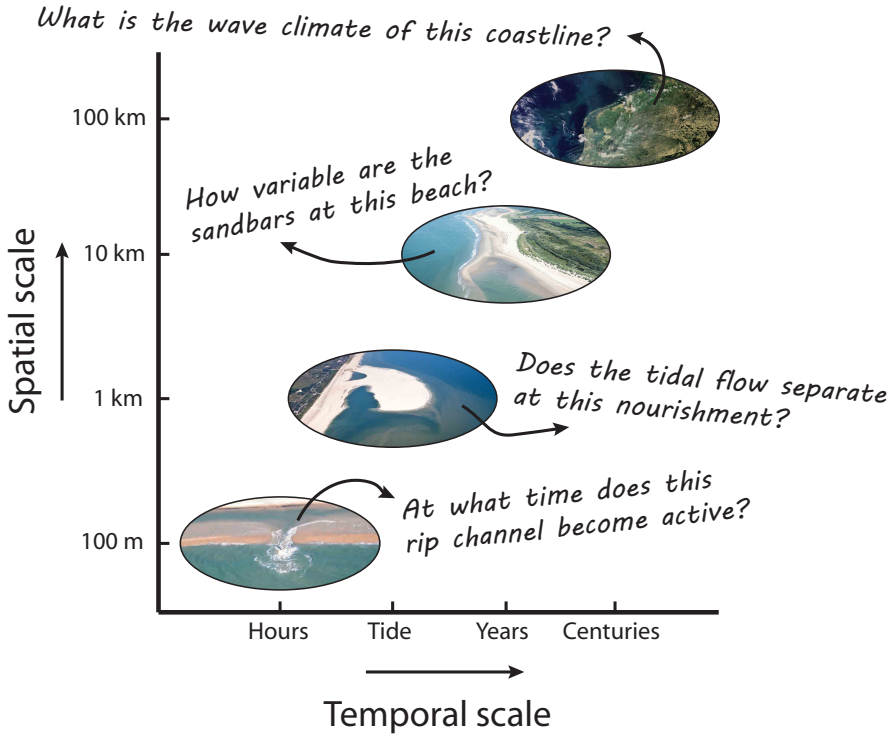
Figure 1.2: Predictability of swimmer safety over a range of spatial and temporal scales. Images (from left to right): https://aquaworld.com, Joop van Houdt/Rijkswaterstaat, Beeldbank Rijkswaterstaat, WikiMedia.

thesis. It is expected to aid coastal engineers and decision makers in minimising swimmer safety risks around such coastal interventions.

1.3. PHYSICAL HAZARDS AROUND MEGA NOURISHMENTS

As explained above, mega-scale beach nourishments (or mega nourishments in short) have been suggested and tested in recent years as a method to establish long-term sand supply to sediment-starved coastlines. Due to their large scale, they have the potential to significantly perturb coastal hydrodynamics, while their autonomous morphodynamic development over the course of their long lifetime is a potential source of uncertainty. Here, an overview is created of potentially hazardous hydrodynamic phenomena that may be caused by the presence of a mega nourishment.

The Sand Motor is the central object of this study (Figure 1.3). Its initial design contains two characteristic elements: (1) it protrudes from the shoreline over multiple surfzone widths and (2) it contains an artificial lagoon. The first element will be part of most mega nourishment designs, as it is difficult to accommodate a large

Figure 1.3: Aerial photographs of the Sand Motor after completion of its construction in 2011 (left) and after three years of morphodynamic development (right). Images by Joop van Houdt / Rijkswaterstaat.

volume of sand at a coastline without letting it protrude into the sea. The second element is rather specific for the particular design of the Sand Motor, although the formation of such lagoons has also been observed in natural systems as a result of coastline instability and spit formation (Achete and Luijendijk, 2012). At the Dutch North Sea coast, nearshore currents are primarily driven by waves and tides, both of which are taken into account here.

In total, four potentially hazardous flow patterns are identified here that can be induced by the presence of a mega nourishment (see Figure 1.4). First of all, the alongshore tidal current might contract around the most seaward point of the nourishment, giving rise to intensification of the tidal flow. A swimmer who is caught in a strong alongshore current will not be transported away from the coastline, as is the case in a rip current. However, the rapid shift of fixed orientation points on shore that is perceived by an alongshore drifting observer may cause the swimmer to panic (De Zeeuw et al., 2012). Once a swimmer panics, any strong current forms a life-threatening hazard, amongst others due to the natural human response to start swimming against the current.

Secondly, the tidal current might separate from the shoreline downstream of the nourishment. This is associated with offshore directed flow around the tip of the nourishment. Due to the large spatial extent of this flow pattern, a beach user caught in the separating tidal flow will not be transported back to the beach quickly, as is often observed in rip current circulations (MacMahan et al., 2010; McCarroll et al., 2014).

The third potentially hazardous flow pattern around a mega nourishment is associated with tidal currents in the lagoon and its entrance channel. Provided that the tidal range and surface area of the lagoon are sufficiently large, significant tidal pumping may occur, driving strong currents near the entrance of the lagoon. Due to morphodynamic evolution of the nourishment, the main dimensions of the entrance channel (length, depth, width) are expected to change over time. As was noted above, strong alongshore directed currents can cause distress to swimmers and bathers.

Finally, the autonomous morphodynamic evolution of a mega nourishment can give rise to alongshore variable sandbar patterns, which in turn may lead to the gen-
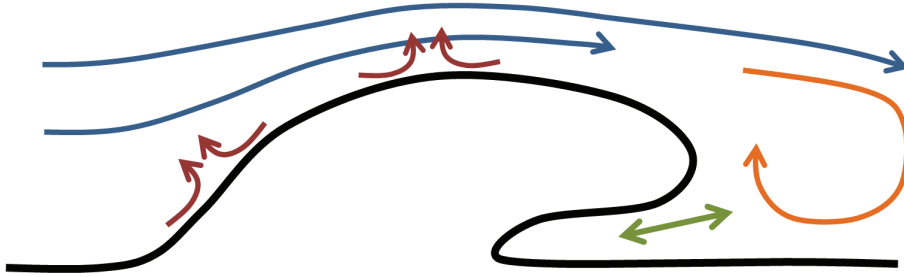
Figure 1.4: Potentially hazardous hydrodynamic features at a mega nourishment.

eration of rip currents (MacMahan et al., 2006; Dalrymple et al., 2011; McCarroll et al., 2017). The offshore directed flow in a rip current forms a major hazard to swimmers and bathers, directly leading to many drownings every year around the world (Brighton et al., 2013; Woodward et al., 2013; Arozarena et al., 2015; Barlas and Beji, 2016).

1.4. RESEARCH OBJECTIVES AND THESIS OUTLINE
The main research objective of this study is:

To determine and understand how a mega-scale sand nourishment influences nearshore hydrodynamics and thereby affects swimmer safety.

Four main research questions are addressed in this thesis:

1. **What is the influence of ongoing sand nourishments on the existence and behaviour of subtidal sandbars at the Delfland coast?** This question is addressed in Chapter 2. Amongst others, the alongshore variability of sandbars under influence of sand nourishments is analysed, which in part determines the potential for rip current formation.

2. **What are the characteristics of the tidal flow field around mega-scale beach nourishments under varying nourishment geometry and tidal conditions?** Chapter 3 focuses on the influence of sand nourishments on alongshore tidal currents, deriving the conditions that promote contraction and separation of the tidal flow.

3. **What is the influence of remotely-sensed bathymetry input on numerical simulations of nearshore hydrodynamics?** In Chapter 4, a numerical model

is combined with remotely-sensed bathymetry data to generate nearshore current predictions, particularly focusing on the added value of the remotely-sensed bathymetry. This tool may assist lifeguards and other rescue services in determing the spatial and temporal occurrence of hazardous hydrodynamics.

4. **What is the effect of the Sand Motor mega nourishment on swimmer safety?**
In Chapter 5, a synthesis of swimmer safety around sand nourishments is presented, applying the generic framework for coastal swimmer safety to the case of the Sand Motor. A key aspect of the synthesis is the spatio-temporal coincidence of the potentially hazardous hydrodynamics addressed in this introduction and the presence of beach users.

Finally, the general conclusions are presented in Chapter 6. It is noted that Chapters 2 through 4 will be or have been submitted separately as research articles to scientific journals, which might account for some redundancy in the introduction sections of these chapters.

2

BEHAVIOUR OF SUBTIDAL SANDBARS IN RESPONSE TO NOURISHMENTS

The behaviour of subtidal sandbars can be strongly influenced by the introduction of sand nourishments in the coastal system. Subtidal sandbars play an important role in wave-driven coastal evolution, as waves typically break at or near a submerged sandbar, driving nearshore currents and sediment transport. This study aims to determine the long-term behaviour of subtidal sandbars along an entire coastal cell, taking into account both the unnourished and nourished regime, and covering various types of nourishments. The analysis is based on over 50 years of sandbar evolution along the Delfland coast.

Observations reveal clearly different sandbar behaviour during the unnourished (first 20 years) and nourished periods of the dataset. In the unnourished system, subtidal sandbars are only present along a limited section of the coast and are characterized by low alongshore variability and slow offshore migration. Sandbar dynamics in the nourished system were found to depend strongly on the type of sand nourishment. Beach nourishments tended to stimulate the formation of a new sandbar within the first 3-4 years after execution. Shoreface nourishments tended to migrate shoreward rapidly, thereby forcing the pre-existing sandbar to weld to the dry beach. An abrupt transition of sandbar dynamics was observed following a major nourishment operation that covered the entire coastal cell. A new, shallow sandbar formed with a degree of alongshore variability that was unprecedented at the Delfland coast over the full study period.

These results imply that individual nourishments can influence the formation and migration of individual sandbars, while continued nourishments can fundamentally change long-term sandbar dynamics along an entire coastal cell.

2.1. INTRODUCTION

Sand nourishments are commonly used as a 'soft' engineering strategy to mitigate coastal erosion problems (Hamm et al., 2002). Nourishments are constructed in a wide variety of sizes and shapes, and in contrast to 'hard' engineering measures (e.g. groynes or breakwaters) they are eventually absorbed by surrounding morphology. Notably, the development of nearshore sandbars can be influenced by the presence of a sand nourishment (Grunnet and Ruessink, 2005; Ojeda et al., 2008). Sandbars can be found along many sandy coastlines worldwide. Their presence plays an important role in the morphodynamic evolution of a beach, as wave breaking and associated wave-driven sediment transport typically occurs at or near a submerged sandbar (Ruessink et al., 2001; Mil-Homens et al., 2013).

The natural behaviour of nearshore sandbars, in the absence of nourishments, has been studied for multiple decades based on field observations and various modelling frameworks. Typically, the behaviour of sandbars is described in terms of (1) their cross-shore migration and (2) alongshore variability. Cross-shore migration refers to the temporal evolution of cross-shore sandbar position and secondary characteristics such as sandbar volume, amplitude and crest level. At timescales from months to decades, sandbars are found to exhibit a net offshore migration (NOM; Ruessink and Kroon, 1994; Walstra et al., 2016; Plant et al., 1999; Shand and Bailey, 1999; Ruessink et al., 2003; Tătui et al., 2016). NOM can either occur at a relatively constant rate over time (mainly in wind-sea climates), or occur rapidly in response to storm events (episodic NOM, mainly in swell wave climates; Ruessink et al., 2009). Offshore migrating bars are typically found to originate near to the shoreline, migrate offshore and finally diminish outside the surf zone. The return timescale associated with this cyclic behaviour varies strongly between different sites and has been linked to the steepness of the cross-shore profile (Walstra et al., 2016). Net onshore migration has been reported less frequently (Aagaard and Kroon, 2007).

Alongshore sandbar variability is associated with the development of threedimensional patterns in the sandbar at length scales ranging between $\mathcal{O}(100 \text{ m})$ and $\mathcal{O}(1 \text{ km})$ (Holman, 2001). Short-scale sandbar variability is typically observed as an alongshore alternation of shoals and rip channels, which can be found along many open ocean coastlines (e.g. Wright and Short, 1984; Holman et al., 2006). At marginal sea coasts with predominantly wind-sea climates, alongshore variability is characterised by subtle crescentic bar crest shapes (Van Enckevort and Ruessink, 2003) or sudden discontinuities in the bar crest (Grunnet and Ruessink, 2005; Ruessink et al., 2012). This kilometre-scale sandbar variability is often attributed to alongshore differences in the phase of the NOM cycle (Walstra et al., 2015; Aleman et al., 2017), as opposed to surfzone flow circulation patterns that govern the generation of short-scale alongshore variability (Reniers et al., 2004; Coco and Murray, 2007). Eventually, differential NOM may lead to rupture of the bar crest. If this occurs in a multiple bar system, bars may reattach to another bar crest at the location of the rupture, referred to as bar switching (Wijnberg and Wolf, 1994; Shand, 2003; Walstra et al., 2015).

Sand nourishments impact nearshore sandbar evolution, depending on the location, size and shape of the nourishment. Nourishments can roughly be subdi-

Traditional beach and dune nourishment

Shoreface nourishment

Localized mega nourishment
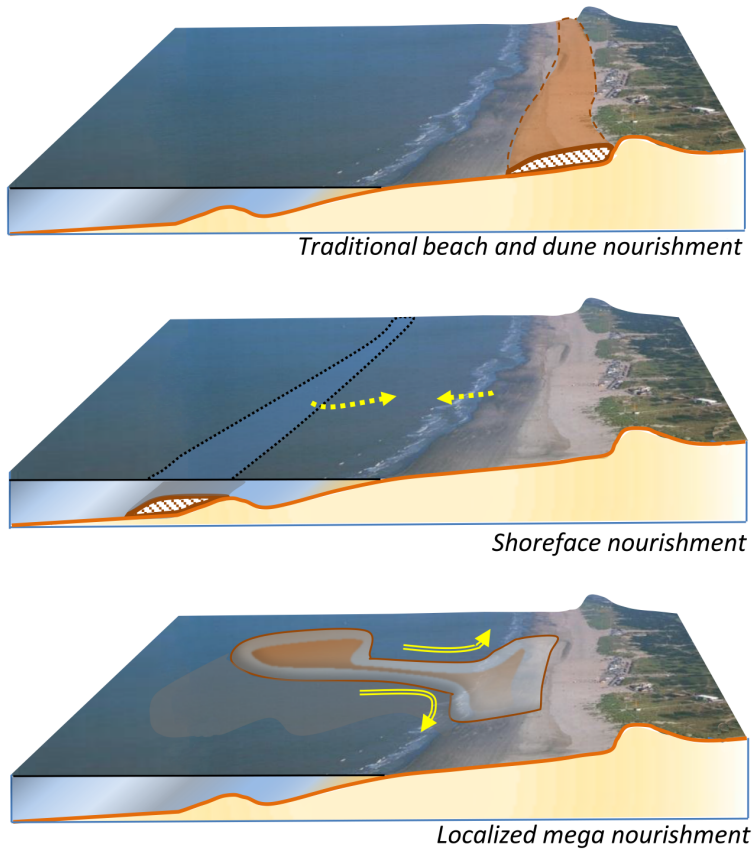
Figure 2.1: Different types of sand nourishments, after Stive et al. (2013).

vided into three different categories (Figure 2.1). In beach and dune nourishment operations (first category) the sand is placed at or adjacent to the dry beach and dune, directly leading to a larger volume and subaerial width of the beach (Dean, 2002). Beach and dune nourishments are often designed with a relatively steep cross-shore beach slope near the waterline. If the nourishment covers pre-existing sub-tidal bars, a barless profile remains. The first high wave energy events following execution of the nourishment will flatten the profile, thereby moving sand from the waterline towards deeper water. This typically results in the creation of a subtidal bar, as observed by Elko and Wang (2007), Yates et al. (2009), Roberts and Wang (2012) and De Schipper et al. (2013) at individual nourishment projects.

Shoreface nourishments (second category) are placed lower in the cross-shore profile, mostly at the seaward face of the subtidal bar (Kroon et al., 1994). The nourished sand may redistribute over the active beach profile, thereby indirectly nourishing the dry beach. Furthermore, the presence of a shoreface nourishment might directly contribute to offshore dissipation of incoming storm wave energy. At the

2

multi-barred Dutch North Sea coast, shoreface nourishments have been applied in coastal maintenance since the 1990's (Hamm et al., 2002). Here, the effect of shore-face nourishments on subtidal sandbars has been studied at the beaches of Noord-wijk, Egmond and Terschelling. The NOM cycles that characterise the natural dynamics at these three sites were disturbed by the presence of the nourishment for a period of several years. Instead of offshore migration, bars were observed to stop migrating (Grunnet and Ruessink, 2005; Ojeda et al., 2008; Ruessink et al., 2012) or even migrate slightly onshore (Kroon et al., 1994; Van Duin et al., 2004; Lodder and Sørensen, 2015) for periods of multiple years following execution of the shoreface nourishment.

While beach and shoreface nourishments primarily strengthen the coastline locally, mega nourishments (third category) are intended to act as a long-term (decades) source of sediment for a larger stretch of coast through naturally occurring alongshore sediment transport. To date, only very few mega nourishments have been executed, one of them being the Sand Motor (Stive et al., 2013) in the focus area of the present study (further discussed in Section 2.2).

The impact of nourishments on alongshore sandbar variability has only been addressed by a few studies. The emergence of large-scale three-dimensional sandbar patterns was reported following a shoreface nourishment at Terschelling (Grunnet and Ruessink, 2005). The presence of the shoreface nourishment along part of the beach induced spatial differences in cross-shore bar migration rate, as offshore bar migration was halted along the nourished section of the beach. This resulted in bar crest ruptures, yielding alongshore variability of the subtidal sandbars. A similar evolution was observed after a shoreface nourishment at Egmond and Noordwijk (Van Duin et al., 2004; Ojeda et al., 2008; Ruessink et al., 2012). At the Sand Motor mega nourishment, highly pronounced sandbar patterns and clear alongshore differences in the response of sandbars were reported (Rutten et al., 2017c), which contrast common sandbar behaviour at the Dutch coast.

Existing studies into the effect of nourishments on sandbar dynamics focussed either on one single nourishment project over the first years after its construction or on a limited alongshore extent. While this yields valuable insights into the joint morphologic development of nourishments and sandbars at relatively short and small scales, it remains unclear how repeated nourishments and implementation of different nourishment types affect the natural, unnourished behaviour of the system. The present study focuses on spatio-temporal scales beyond a single nourishment project and aims to determine the long-term behaviour of subtidal sandbars along an entire coastal cell, taking into account both the unnourished and nourished regime, and covering various types of nourishments.

The analysis makes use of a 52-year bathymetric dataset of the 17-km long Delfland coast, a coastal cell at the Dutch North Sea coastline that has received a wide range of sand nourishments over the last decades. Having a low-lying hinterland that represents a large economic value, the Delfland coast plays an important role in the coastal flood protection system of The Netherlands. The construction of the Sand Motor mega nourishment in 2011 has drawn large scientific attention to the Delfland coast, adding to the importance of an adequate understanding of its long-

term sandbar dynamics. Firstly, the field site and methodology are introduced (Sections 2.2 and 2.3). Subsequently, fifty years of observations of sandbar dynamics at the Delfland coast are presented in Section 2.4. Finally, these observations are analysed and discussed (Section 2.5).

2.2. Field site

Sandbar dynamics are analysed here for the Delfland coast, a 17 km long sandy beach at the Dutch North Sea coastline. It is constrained by the long harbour breakwater (3.5 km) of Rotterdam in the southwest and the relatively short harbour breakwaters (0.5 km) of The Hague in the northeast (Figure 2.2). The cross-shore profile slope of the Delfland coast typically is around 1:80 in the upper part of the profile (between 0 and 7 m depth with respect to Mean Sea Level (MSL)) and 1:400 in the lower part of the profile (below -11 m MSL). The average shore-normal orientation of the coast is 310 degrees North, which deviates locally around the harbour breakwaters in Rotterdam and The Hague. The wave climate at the south-eastern North Sea is bimodal, with energetic waves arriving from the South-West or from the North. The annual mean significant wave height is 1.3 m, with typical wave periods around 5 to 6 s (Wijnberg, 2002). Sediment at the Delfland coast consists of medium-sized sand in the surf and swash zone, with the median sediment diameter ranging between approximately 200 and 400 μm (Huisman et al., 2016). The tidal range varies between 1.4 m and 1.8 m over a spring-neap cycle (Wijnberg, 2002) and drives an alongshore directed tidal current with peak flow velocities in the order of 0.7 m/s depth-averaged at a water depth of 9 m (Radermacher et al., 2017a).

Similar to other parts of the Dutch coastline, the Delfland coast has been subject to structural erosion for the last 2000 years (Beets and Van der Spek, 2000) in response to Holocene sea level rise and changing sediment supply. In order to protect coastal towns and their low-lying hinterland, humans have made attempts to stop coastal erosion or mitigate its adverse effects. First, this was done by the creation of artificial dykes. Later, wooden and stone groynes were built perpendicular to the beach in order to obstruct the alongshore sediment transport, which are still in place nowadays. At the Dutch coast, beach and dune nourishments have been a standard coastal maintenance practice since the 1970's. The Dutch national government has actively increased sand volumes at the Delfland coast (Hillen and Roelse, 1995) by the execution of over 20 different sand nourishments in the area (Figure 2.3). While early sand nourishments were placed directly onto the beach and the dunes (beach and dune nourishment), from the late 1990's onwards it became more common to place the nourished sand in the subtidal part of the beach profile (shoreface nourishment). A large-scale human intervention took place in 2011, when an experimental mega-scale nourishment (the Sand Motor, Stive et al., 2013) of 17 Mm^3 (9000 m^3/m alongshore) was implemented at the Delfland coast. The Sand Motor, which originally formed a hook-shaped sandy peninsula, does not only strengthen the beach and dune system locally (Hoonhout and De Vries, 2017; Nolet et al., 2018), but also feeds sand to adjacent beaches along the Delfland coast (De Schipper et al., 2016; Luijendijk et al., 2017; Arriaga et al., 2017).

Most of these nourishments were placed at the southern and central parts of

2
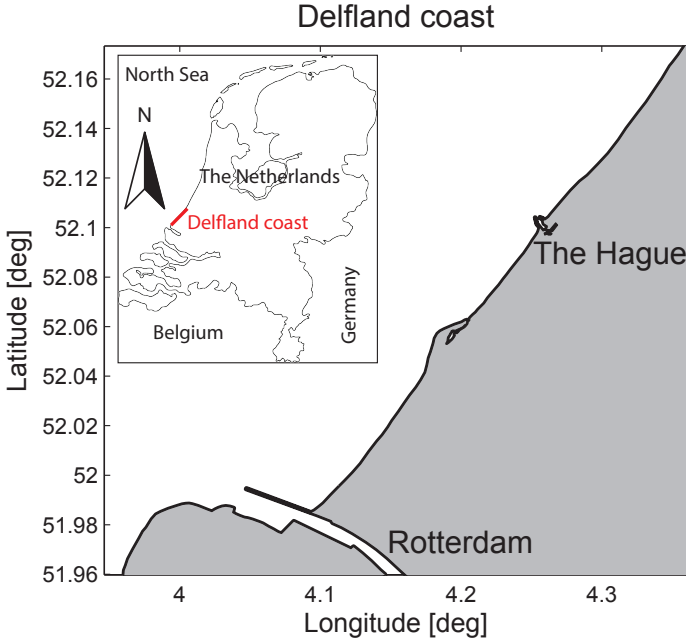
Figure 2.2: Setting of the Delfland coast. The Sand Motor is visible as a seaward perturbation in the middle of the coastal cell.

the coastal cell, while the northern part (alongshore coordinate > 2000 m, Figure 2.3) only received its first nourishments after 2010. Several small, localised nourishments near the southern end of the coastal cell are related to sediments dredged from the Rotterdam harbour entrance channel for navigability purposes. Their repetitive character, very limited spatial extent and proximity to the Rotterdam harbour mole obscure the morphodynamic development of the individual nourishments. These nourishments are therefore omitted from further analysis.

2.3. Methodology

Bathymetric data of the Delfland coast were obtained from the JARKUS dataset. Since 1965, the Dutch Ministry of Infrastructure and Water Management (Rijkswaterstaat) has collected annual cross-shore beach elevation profiles over the full length of the Dutch coastline at fixed intervals of approximately 250 m in alongshore direction (Southgate, 2011). The annual surveys are always collected in spring in order to create a consistent dataset and avoid the influence of seasonal fluctuations. An overview of sandbar evolution was created by detecting the crest level and location of subtidal sandbars in the cross-shore profiles. Downward zero crossings of the smoothed first derivative of cross-shore beach elevation were identified as bar crests (Figure 2.4, smoothing length scale of 50 m). Only bar crests situated at a water depth between -1.5 m and -7 m with respect to mean sea level (MSL) were
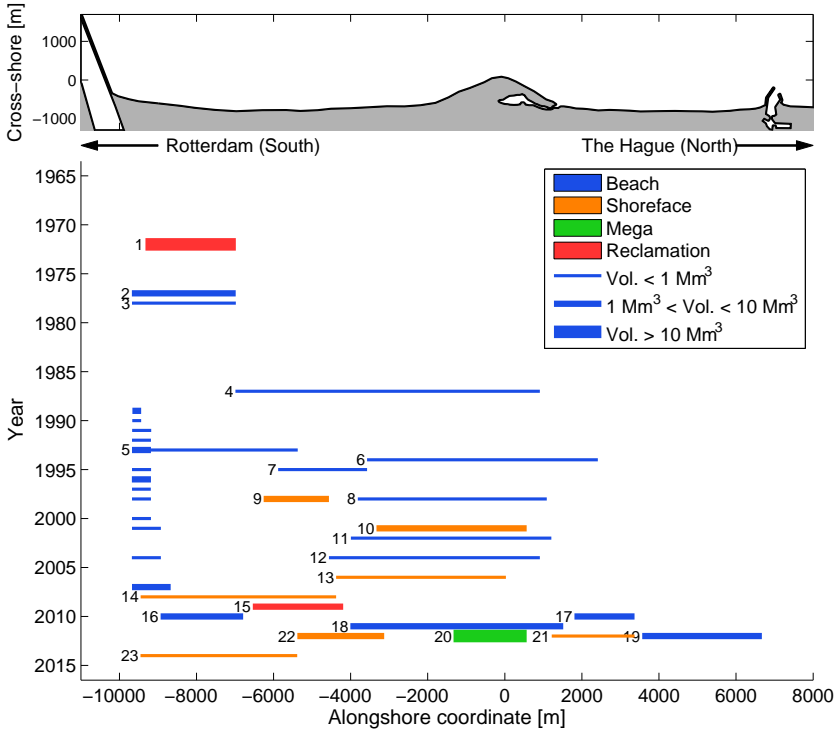
Figure 2.3: Overview of all sand nourishments executed at the Delfland coast until 2016 based on nourishment type and nourished volume per alongshore metre of beach. Unnumbered nourishments are considered insignificant and are omitted from further analysis. Nourishment data were obtained from the Dutch Ministry of Infrastructure and Water Management (Rijkswaterstaat).
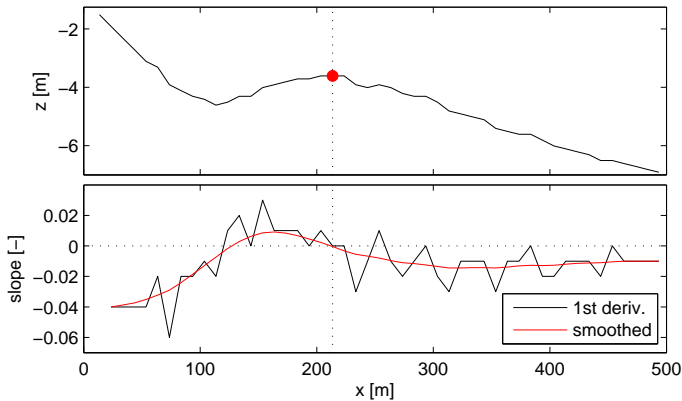
Figure 2.4: Demonstration of the bar crest detection method, based on downward zero crossings of the smoothed cross-shore beach slope.
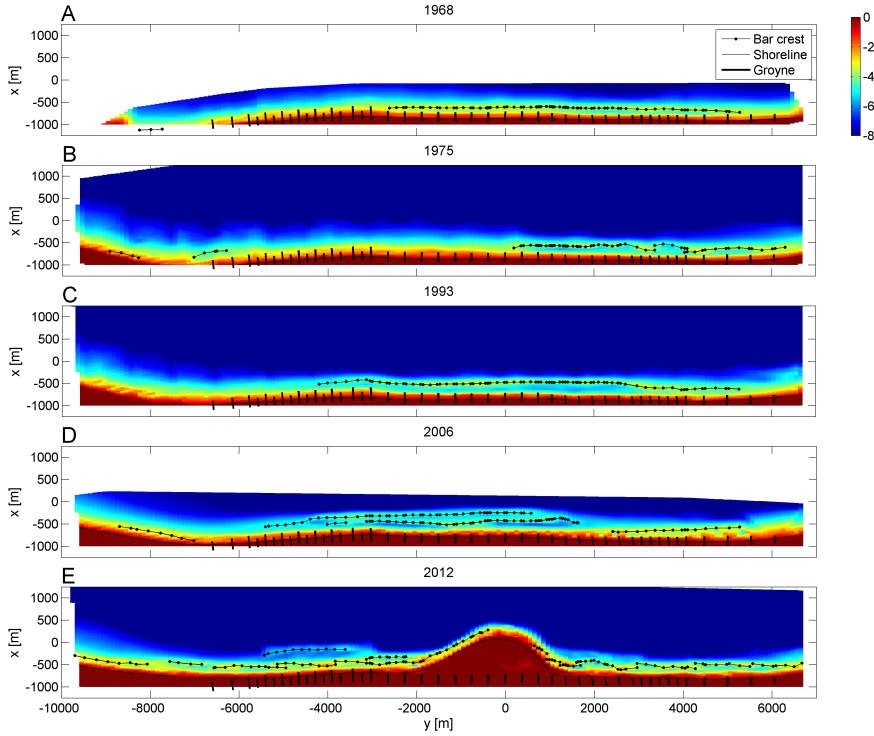
Figure 2.5: Five JARKUS surveys including detected sandbars. The shading indicates bed level in m with respect to the local datum (≈ mean sea level). Detected bar crests, the shoreline and the locations of rubble-mound groynes are indicated with markers and lines (see legend). The local coordinate system is aligned with the average coastline orientation and has its origin at the tip of the Sand Motor.

accepted for analysis. Subsequently, bar crests identified in individual profiles were linked to nearby bar crests in adjacent profiles to define coherent sandbars with a certain alongshore coverage. Every bar crest was linked to a neighbouring bar crest in alongshore direction, provided that both were less than 150 m apart and the line connecting the two bar crests made an angle of less than 40 degrees with the average coastline orientation. Sandbars with limited alongshore size (i.e. covering less than 3 adjacent profiles) were omitted. As an example, the results for five different years are shown in Figure 2.5. The bar detection algorithm is able to detect natural sandbars as well as shoreface nourishments appearing in the profile as an artificial sandbar (e.g. the double bar crests in 2006 and 2012, see Figure 2.5 panels D and E).

Additionally, alongshore sandbar variability and cross-shore migration rates were determined. Alongshore sandbar variability σ is computed as the root-mean-squared cross-shore bar position within an alongshore window of 1500 m, reading

$$\sigma(y) = \sqrt{\frac{\sum_w x_{b,u}^2}{n_w}} \qquad (2.1)$$

where x_b denotes the cross-shore bar crest position (subscript u indicates linear trend removal), w is a sliding 1500 m window in y and n_w is the number of bar crests within w. If a double sandbar is present, which occasionally occurs due to the placement of a shoreface nourishment, values are shown for the inner bar only (the outer bar being the nourishment). Finally, year-to-year bar migration rates were calculated as the difference between the subsequent (in time) cross-shore bar crest positions, a positive migration rate indicating offshore migration. Earlier work in this coastal cell based on monthly surveys showed that sandbar characteristics change relatively slowly (De Schipper et al., 2013), such that surveys of subsequent years can safely be used to follow individual bar development without the risk of aliasing.

2.4. OBSERVATIONS OF SANDBAR EVOLUTION

2.4.1. CROSS-SHORE EVOLUTION

An overview of bar crests detected in the full JARKUS dataset reveals large variations in the presence of sandbars in space and time along the Delfland coast (Figure 2.6). The unnourished evolution, which can be observed until 1986, was characterised by the absence of subtidal sandbars along a large part of the coastal cell. At the start of the study period, a subtidal sandbar was only present along the northern half of the coast ($y > -2000$ m). Between 1968 and 1987, the alongshore length of the sandbar gradually decreased from 6 km to 3 km, while the crest level lowered approximately from -3 m to -4 m and the bar moved further offshore (Figures 2.7 and 2.8). The average offshore migration rate of the bar section between $y = 2000$ m and $y = 3000$ m over this period was 5.0 m/year. Although the observed offshore migration did not describe a full cycle including the generation of a new bar near the shoreline, it indicates that the unnourished bar behaviour along the northern part of the Delfland coast was characterised by net offshore migration. This is in line with observations further north along the Dutch coastline at Noordwijk and Egmond (Ruessink et al., 2003; Walstra et al., 2016).

The nourished evolution of subtidal sandbars can be observed from 1987 onwards. Following execution of the first nourishment at the central part of the Delfland coast (nourishment number 4 in Figure 2.3), an 8 km long sandbar was established. This bar expanded 3 km along the coast towards $y = -6000$ m until 1997, coinciding with subsequent beach nourishments in the same area (nourishments 6 and 7). Meanwhile, the sandbar migrated steadily offshore at a rate of approximately 15 m/year. A series of shoreface nourishments between 1998 and 2008 (nourishments 9, 10 and 13) locally and temporarily created double bar systems, one of the bars being the (remnant of the) nourishment. All shoreface nourishments rapidly migrated shoreward at rates ranging between 20 and 60 m/year, thereby forcing the inner sandbar to weld to the beach in the nourished area (an example is presented in Figure 2.9). Both ends of the nourishment connected to the adjacent sandbar, effectively taking over the position of the pre-existing bar.

After 2000, a shallow bar with a crest level around -2.5 m formed in the northernmost part of the coastal cell ($y > 2000$ m). The cross-shore position of this bar was very stable and its crest level persisted around -2.5 m. The first nourishment

2
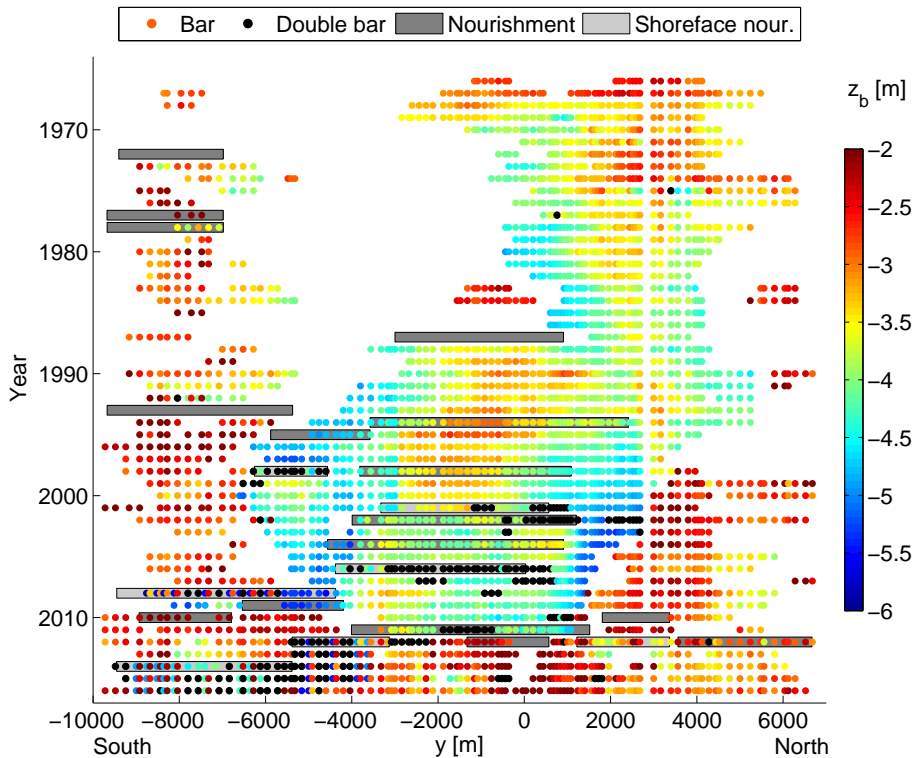
Figure 2.6: Occurrence of subtidal sandbars along the 17 km long Delfland coast between 1965 and 2016. Shading of the markers indicates bar crest level with respect to the local datum, while black markers indicate the presence of a double sandbar. Execution of nourishments is indicated for reference in grey shading. Irregular alongshore spacing is related to non-constant transect intervals.

in the northern part of the domain was only executed in 2010, but the evolution of this sandbar might have been influenced by potential alongshore spreading of nourished sand from the central part of the domain. Therefore its evolution cannot be regarded as strictly unnourished behaviour.

The southern end of the domain was characterised by shallow, dynamic, sandbars with a lifetime of several years, that typically formed after the execution of beach nourishments in the area. Shoreface nourishments (numbers 14 and 23) temporarily created double bar systems for a period of 1-2 years. Similar to the evolution of shoreface nourishments 9, 10 and 13, nourishment 23 rapidly moved onshore.

Between 2009 and 2012, a very large amount of sediment (37.5 Mm^3) was added to the Delfland coast. First, a relatively small land reclamation project was executed between $-7000 < y < -4000$ (nourishment 15), which effectively straightened the local coastline (De Schipper et al., 2013). Shoreface nourishment number 14 was covered by the reclamation project and ceased to exist as a separate sandbar. Subsequently, three large beach (and dune) nourishments were placed, covering a large
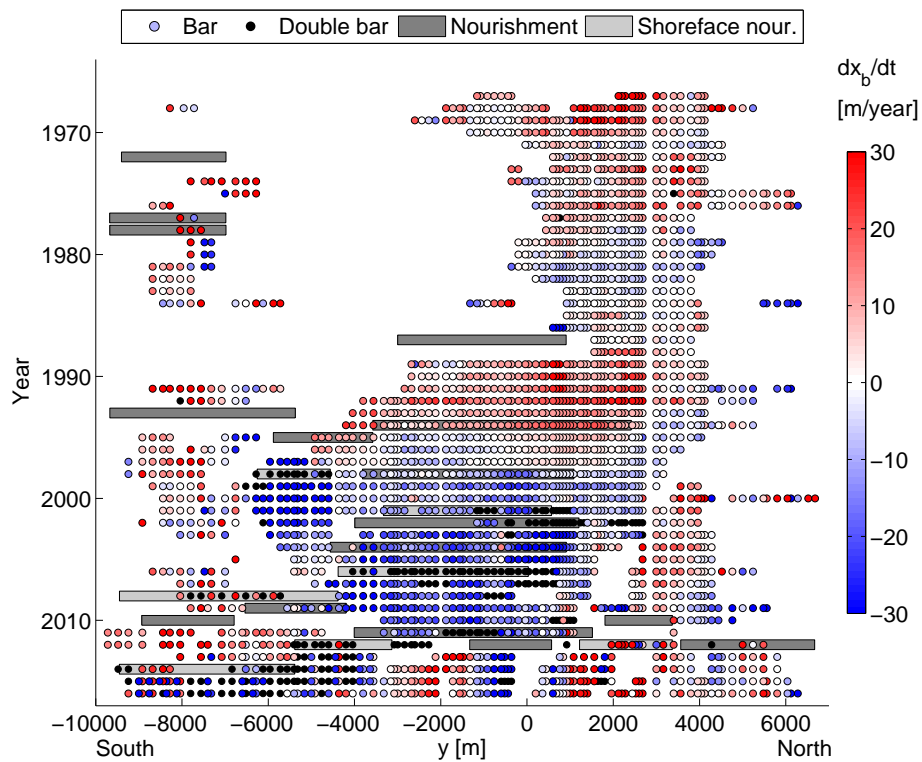
Figure 2.7: Five-year averaged cross-shore migration of subtidal sandbars at the Delfland coast, represented by the coloured markers in m/year. Positive migration is offshore directed.
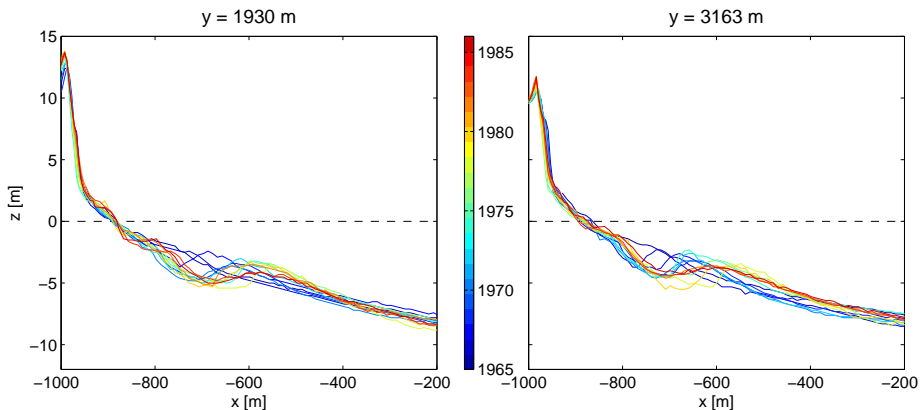
Figure 2.8: Gradual offshore migration of the sandbar in the northern half of the domain in two arbitrary profiles, before any nourishments have been carried out along this section of the Delfland coast.
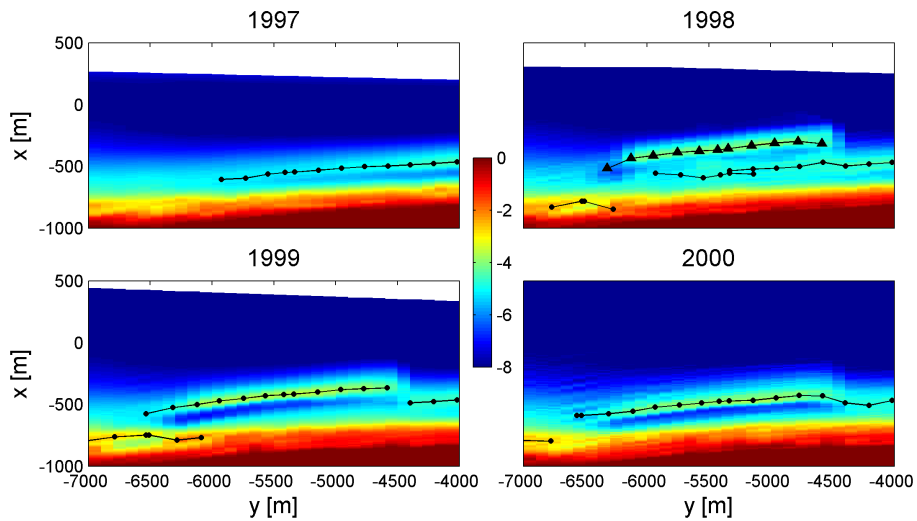
Figure 2.9: Morphological development of the 1998 shoreface nourishment (indicated with triangles in 1998), exhibiting rapid onshore migration of the nourishment. Onshore migration of the pre-existing bar is even faster and occurs during less than one year (1998-1999).

part of the coastal cell (nourishments 16 through 19). In 2011 the Sand Motor was constructed (nourishment 20, showing in 2012 as construction finished in the second half of 2011), along with two adjacent shoreface nourishments (nourishments 21 and 22). The relatively deep sandbar that had existed in the central part of the domain since the 1987 beach nourishment and the shallower bars at the southern and northern end of the domain were almost entirely covered by the nourished sand. A new, shallow sandbar formed along almost the entire Delfland coast. The cross-shore migration rate of this bar was highly variable in space and time. Shoreface nourishment number 22 migrated landward, albeit at a slower rate (around 20 m/year) than observed previously in that area. The other shoreface nourishment (number 21) was covered soon after its construction by massive sand deposition due to the presence of the Sand Motor. This situation, with a shallow sandbar along the full Delfland coast and onshore migration of shoreface nourishments 22 and 23, persisted until the end of the dataset in 2016.

2.4.2. ALONGSHORE VARIABILITY OF SANDBARS

Although most of the subtidal sandbars that were present at the Delfland coast between 1965 and 2016 were relatively straight, alongshore perturbations can be observed at several instances in the dataset (Figure 2.10, notably the last years). In the mid-1970s, prior to the implementation of nourishments at the central part of the Delfland coast, three-dimensional bar patterns developed at 2000 m < y < 4000 m ($\sigma \sim 50$ m). The initially straight sandbar attained a cresentic shape in 1974, subsequently broke up in two obliquely oriented sections in 1975 (Figure 2.5, panel B) and finally straightened again. Until 2009, alongshore sandbar variability remained
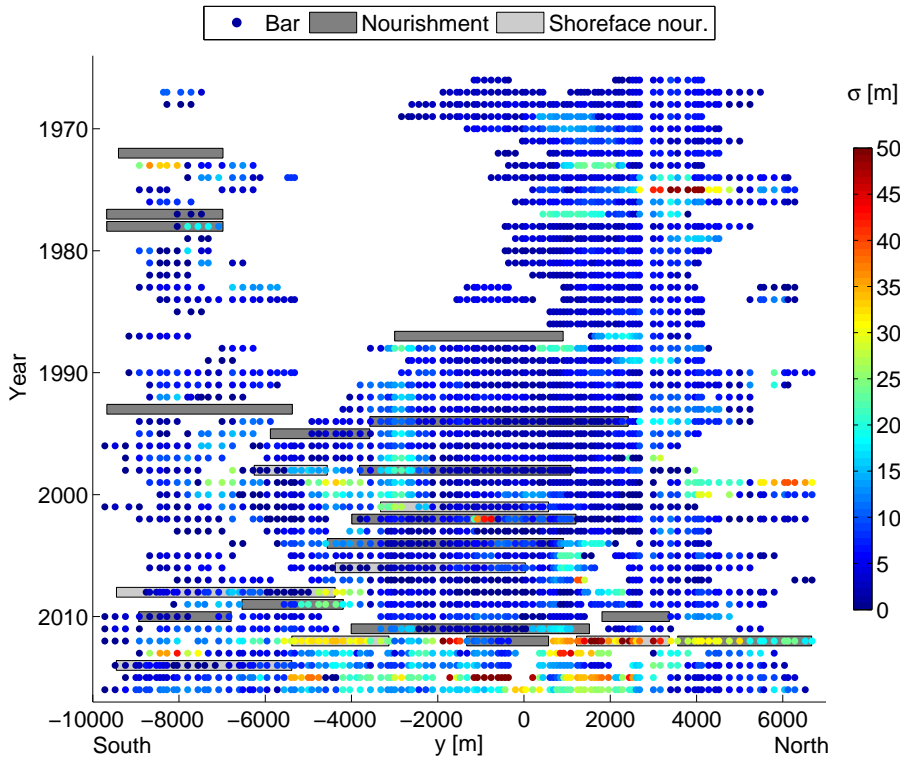
Figure 2.10: Alongshore variability of subtidal sandbars at the Delfland coast, represented by the coloured markers.

fairly limited. Only near the alongshore ends of sandbars and during the onshore merging sequence of shoreface nourishments, moderate variability was observed over a period of several years (e.g. 2004-2006, $y = 1000$ m).

Following the extensive nourishment operations between 2009 and 2012, the system changed drastically. As mentioned before, a shallow nearshore bar was formed along the full Delfland coast, fronted by shoreface nourishments at several locations. This shallow sandbar exhibited a degree of alongshore variability in bar crest position (σ between 20 and 50 m along large parts of the Delfland coast) that was significantly higher than elsewhere in the dataset analysed here (disregarding the mid-1970s event described above, which had a very limited spatial extent). In 2012, several sections of the newly formed sandbar attained an oblique orientation (see Figure 2.5, panel E), attaching to the shoreline on one end while creating a gap in the bar crest on the other end at intervals in the order of 1 km. This pattern slightly resembles the discontinuous sandbar observed in 1975, although extending along a much larger part of the coast. Around the connections of the Sand Motor to the adjacent coastline ($y = -1500$ m and $y = 1500$ m), discontinuities were found between the newly formed sandbars at the mega nourishment and the pre-

existing shallow sandbar that borders it. Finally, in 2015, the subtidal bar attained a highly pronounced crescentic shape ($25 < \sigma < 60$ m) at $-4000 < y < -500$. Based on data obtained from coastal imagery, Rutten et al. (2017b,c) showed that this pattern formed during several weeks of weakly-oblique incidence of energetic waves in the 2014/2015 winter. From high-resolution bathymetric surveys of the Sand Motor (De Schipper et al., 2016), it was confirmed that the dominant scale of these patterns was around 400-500 m. The presence of such repetitive, pronounced crescentic bar patterns at the Delfland coast did not occur elsewhere in the 50-year analysis period.

2.5. DISCUSSION

2.5.1. UNNOURISHED SANDBAR BEHAVIOUR

The unnourished sandbar behaviour at the Delfland coast was inferred from the observations between 1965 and 1986. A sandbar was only present along a limited section of the coastal cell over this period (Figure 2.6). These data suggest that the central part of the Delfland coast has a different equilibrium profile shape (unbarred) than the northern part (barred) over this period. While it remains difficult to determine the actual cause of this difference, one potential mechanism can be identified. The harbour of Rotterdam, which protrudes more than 4 km into the sea, partly blocks south-westerly waves (Figure 2.2). This sheltering effect is strongest at the southern end of the Delfland coast and progressively weakens towards the North. The amount of incoming wave energy and the wave obliqueness influence the delicate balance of cross-shore forcing terms that governs sandbar growth and cross-shore migration (Walstra et al., 2012). Therefore, alongshore differences in local wave climate caused by the harbour of Rotterdam may induce alongshore differences in equilibrium profile shape. Similar alongshore differences in sandbar behaviour have been observed at beaches with strong alongshore variations in wave climate due to sheltering by headlands (Wright and Short, 1984; Thornton et al., 2007; Blossier et al., 2016).

The unnourished bar in the northern half of the Delfland coast was observed to migrate offshore at a very slow rate (Figure 2.8). Within the 20-year observation window of unnourished sandbar development, less than one full offshore migration cycle is completed. The offshore migration rate at this part of the coastline is low compared to locations further north along the Dutch coastline. Faster offshore migration has been observed at Noordwijk (period of $\sim$ 4 years) and Egmond ($\sim$ 15 years) by Ruessink et al. (2003). According to Walstra et al. (2016), the offshore bar migration cycle period is primarily governed by the cross-shore beach slope. A steep profile is characterised by fast initial migration, which slows down drastically as the bar migrates offshore, eventually resulting in a relatively long migration cycle period. The slope of the upper shoreface around $y = 3000$ m is slightly steeper ($1 : 80$) than the slope at Egmond ($1 : 110$), which may explain the longer migration cycle period.

Beach nourishment *(cross-section)*

Pre-nourishment   *Post-nourishment 1*   *Post-nourishment 2*

2

Shoreface nourishment *(cross-section)*

Pre-nourishment   *Post-nourishment 1*   *Post-nourishment 2*

Mega nourishment *(top view)*

Pre-nourishment   *Post-nourishment 1*   *Post-nourishment 2*

.... = Sandbar

Water
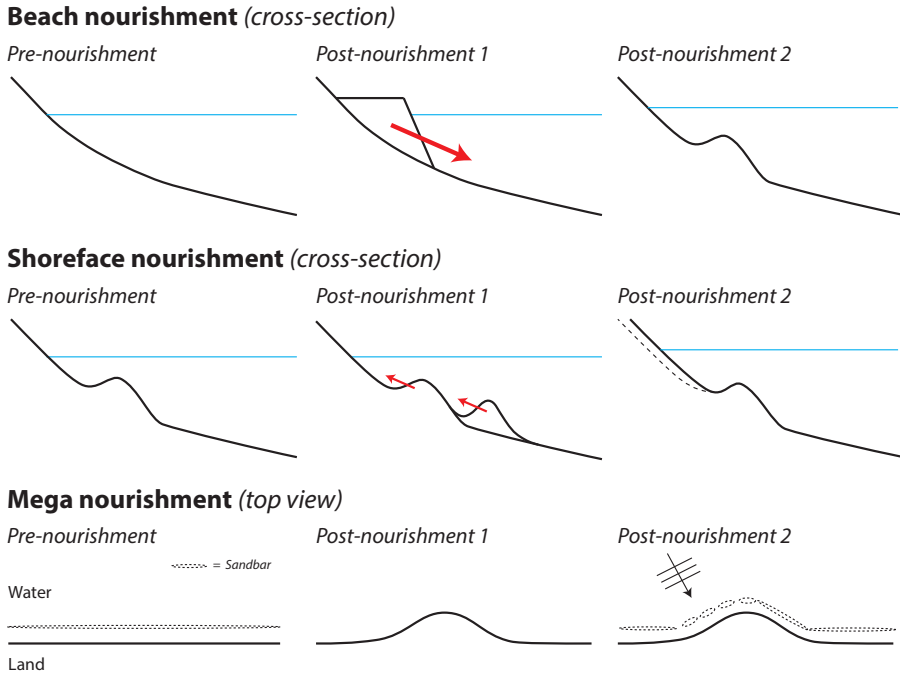
Land

Figure 2.11: Schematic overview of the observed impact of different types of nourishments on subtidal sandbar dynamics at the Delfland coast.

2.5.2. INFLUENCE OF BEACH NOURISHMENTS ON SANDBAR BEHAVIOUR

Over the full period analysed in the present study, 13 beach nourishments were executed. Beach nourishments were found to stimulate the formation of subtidal sandbars (Figure 2.11, top row), which is reflected in statistics of sandbar presence in the years surrounding execution of a beach nourishment. When an unbarred profile was nourished, a new bar developed within 3 years in 84% of all cases (Figure 2.12, middle panel). If profiles are included that already had a subtidal sandbar before the nourishment, the share of profiles with a sandbar 3 years after the nourishment even rises to 93% (left panel). The formation of a sandbar following execution of a beach nourishment is in line with earlier observations (Benedet et al., 2004; Elko and Wang, 2007; Yates et al., 2009; Roberts and Wang, 2012). In general, beach nourishments are placed around the waterline and typically have a steeper cross-shore slope than the pre-nourishment profile. After execution of the nourishment the beach slope is restored towards the equilibrium situation. The surplus of (nourished) sediment in the upper part of the profile is redistributed in cross-shore direction, leading to sandbar formation.

The crest depth of newly formed bars was variable. The bar in the central part of the domain that formed after nourishment 4 was situated at relatively deep water (bar crest around $z = -4$ m; Figure 2.6). The large-scale nourishment scheme carried out between 2009 and 2012 burried the groyne field and the pre-existing sub-

Figure 2.12: Percentage of cross-shore profiles with a sandbar in the years before and after a beach nourishment was carried out (nourishment in year 0). The left panel represents statistics over all profiles, the middle panel only includes profiles that were unbarred before execution of the nourishment (year -1, 100% equals 50 profiles), while the right panel only includes profiles that did have a pre-existing bar (100% equals 137 profiles).

tidal bar, followed by the formation of a relatively shallow sandbar along the entire coastal cell from 2012 onwards (bar crest around $z = -2.5$ m; Figure 2.6).

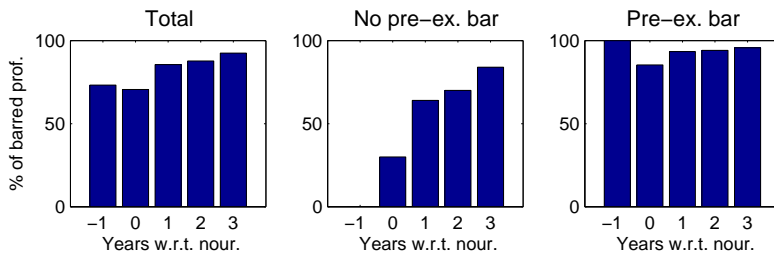The Sand Motor mega nourishment (nourishment number 20 in Figure 2.3) behaved as a regular beach nourishment in terms of its profile development. A sandbar formed along the entire contour within one year after completion of construction and remained in place until the end of the analysis period.

2.5.3. INFLUENCE OF SHOREFACE NOURISHMENT ON SANDBAR BEHAVIOUR

In total, 7 shoreface nourishments were placed at the Delfland coast within the study period. The first shoreface nourishments (number 9, 10 and 13), as well as the last two (number 22 and 23) migrated onshore (Table 2.1), thereby forcing the pre-existing sandbar to move shoreward and weld to the beach in most cases (Figure 2.11, middle row). The onshore migration rates of nourishments 9, 13 and 23 were very high (-62, -39 and -47 m/year respectively in the first year after execution), while the migration rates of nourishments 10 and 22 were lower (-16 and -24 m/year respectively in the first year after execution). Based on these observations alone the cause of this difference cannot be identified, although such spatial differences in cross-shore migration rate and direction of shoreface nourishments have been observed before (Wilmink et al., 2017).

The observed rapid onshore migration of shoreface nourishments contrasts with reported shoreface nourishment evolution at Noordwijk, Egmond and Terschelling. At these locations, the nourishment and the natural sandbar(s) were found to keep their position or slightly migrate shoreward (Kroon et al., 1994; Van Duin et al., 2004; Grunnet and Ruessink, 2005; Ojeda et al., 2008). Rapid onshore migration of the nourishment was only reported at Bloemendaal in The Netherlands (Lodder and Sørensen, 2015), while onshore welding of the pre-existing bar after implementation of a shoreface nourishment has not been reported before in scientific literature.

The evolution of the other two shoreface nourishments (numbers 14 and 21) was strongly influenced by subsequent large-scale nourishments. The trough landward of nourishment 14 was filled up by the 2009 land reclamation, effectively covering the shoreface nourishment and thereby halting its evolution. Nourishment 21 was

Table 2.1: Cross-shore migration rates (m/year, positive offshore) of shoreface nourishments over the first years after their implementation; *n/a* values indicate that sandbar evolution was disturbed by subsequent nourishments or extended beyond the end of the dataset.

Nourishment	Year 1	Year 2	Year 3	Year 4
#9	-62	-58	-28	-32
#10	-16	-12	-20	n/a
#13	-39	-29	-7	-21
#14	n/a	n/a	n/a	n/a
#21	n/a	n/a	n/a	n/a
#22	-24	-17	-25	n/a
#23	-47	-44	n/a	n/a

placed close to the pre-existing bar at a section of the coastline that was rapidly covered by deposits from the nearby Sand Motor.

2.5.4. INFLUENCE OF NOURISHMENTS ON ALONGSHORE SANDBAR VARI-ABILITY

The alongshore variability of natural, human-influenced and man-made sandbars at the Delfland coast was derived in the previous section (Figure 2.10). The unnourished and nourished bar systems between 1965 and 2011 were both largely characterised by straight bars ($\sigma \approx 5 - 10$ m). Local increases were only observed around the edges of shoreface nourishments, where discontinuities developed between the nourishment and the adjacent sandbar (Wijnberg and Wolf, 1994; Ojeda et al., 2008). This is in line with earlier observations of subtidal sandbars at the Dutch North Sea coastline, which all indicate that bar crest variability is relatively low compared to the distinct, rhythmic, three-dimensional bar patterns that are found at open ocean beaches (Short and Aagaard, 1993; Van Enckevort and Ruessink, 2003; Ojeda et al., 2008; Ruessink et al., 2012; De Schipper et al., 2013; Walstra et al., 2015). After the implementation of extensive beach and shoreface nourishments along almost the entire coastal cell between 2009 and 2012, a degree of alongshore variability arose that was unprecedented in the 50-year study period (Radermacher et al., 2017b).

These results are reflected in a direct comparison of bar crest depth and alongshore variability (Figure 2.13). Sandbars were more variable in general from 2011 onwards (stars in Figure 2.13), while before that year alongshore variability mainly occurred near the end points of shoreface nourishments (triangles in Figure 2.13). If data points obtained near the end points of shoreface nourishments are ignored, it appears that variable sandbars on average had a relatively shallow bar crest depth, while deeper bar crests had low alongshore variability (reflected by the red lines in Figure 2.13). A possible cause for the emergence of shallow, variable sandbars after 2011 is the burial of groynes by the 2009-2012 beach nourishment operation. Groynes impact hydrodynamics (Scott et al., 2016) and morphodynamics (Short, 1992) in the inner surfzone. Their presence may prevent the formation and evolution of nearshore sandbars, which could lead to the observed differences in sandbar dynamics before and after 2011. The alongshore variable, obliquely oriented

2
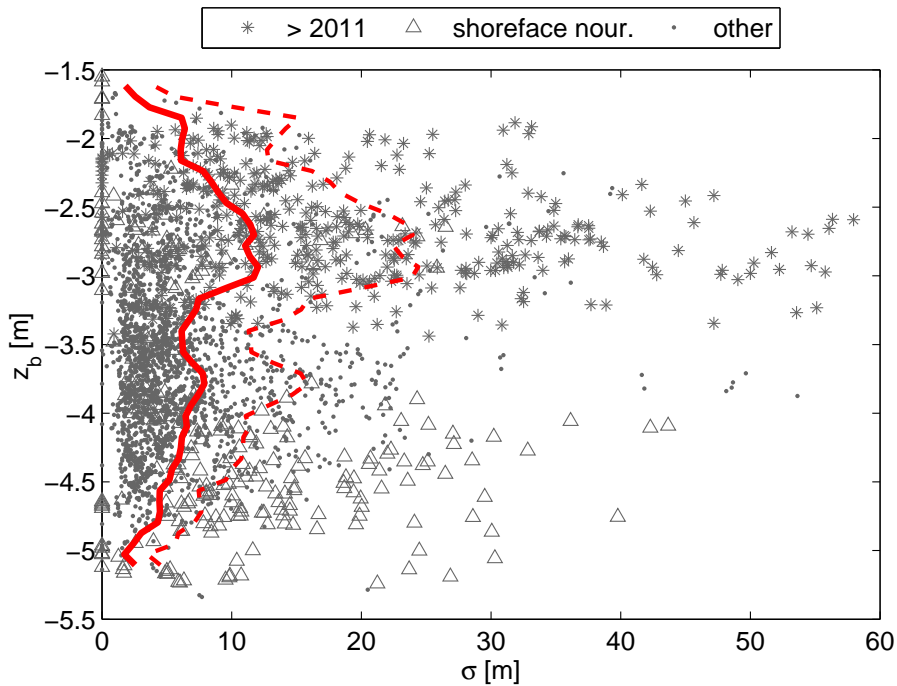
Figure 2.13: Comparison of sand bar variability (horizontal axis) and bar crest depth (vertical axis). Data points obtained around the end points of shoreface nourishments have been marked with triangles, while data points obtained after 2011 have been marked with stars. The solid red line represents a window-averaged variability in a sliding depth window of 0.25 m (excluding shoreface nourishment data points). The windowed average plus one windowed standard deviation is indicated with a dashed red line.

bar crests that arose after 2011 resemble observations along the French Mediterranean coast (Aleman et al., 2017). There, this particular bar pattern was linked to alongshore variations in the phase of net offshore sandbar migration. Whether such variations in NOM phase also caused the observed variability at the Delfland coast remains difficult to determine due to the short observation period of these recent bar patterns.

Finally, the formation of highly pronounced crescentic sandbars at the southern side of the Sand Motor in early 2015 is remarkable. The observed patterns are unique for the Dutch North Sea coastline in terms of their rhythmicity and amplitude. This is confirmed by the fact that these patterns are associated with the highest σ in the entire dataset analysed here (Figure 2.10). Rutten et al. (2017b) and Rutten et al. (2017c) found that the Sand Motor mega nourishment plays an important role in the formation of these patterns. Very large nourishments are associated with changes in the local coastline angle, changing the orientation of the coast with respect to the local wave climate. The wave climate at the Dutch North Sea coast is dominated by southwesterly and northerly waves, both of which correspond with highly oblique

wave incidence given the overall orientation of the Delfland coast. In contrast, the curved coastline at the Sand Motor received more normally-incident wave energy, associated with a higher probability of three-dimensional bar pattern generation (Calvete et al., 2005; Price and Ruessink, 2011; Thiébot et al., 2012). As such, very large nourishments may give rise to unprecedented sandbar morphodynamics by locally changing the coastline orientation (Figure 2.11, bottom row).

2.6. CONCLUSIONS

The behaviour of sandbars at the Delfland coast has been studied at spatio-temporal scales beyond a single nourishment project, revealing the long-term behaviour of subtidal sandbars along an entire coastal cell, taking into account both the unnourished and nourished regime, and covering various types of nourishments. The results presented in this study imply that individual nourishments can influence the formation and cross-shore migration of individual sandbars, while continued nourishments can fundamentally change long-term presence, cross-shore migration and alongshore variability of sandbars over an entire coastal cell.

It was found that in the unnourished system (first 20 years of the study period), a subtidal sandbar was present in only a part of the coastal cell. This sandbar exhibited net offshore migration at a low average rate. The initial migration rate was high, but slowed down several years after formation of the sandbar. Alongshore variability of unnourished sandbars along the Delfland coast was very low. The unnourished sandbar behaviour at the Delfland coast is consistent with earlier observations further north along the Dutch coastline.

Clearly different sandbar behaviour was observed in the nourished system. Placing nourished sediment at the subaerial beach, as done with regular beach nourishments and mega nourishments, resulted in the formation of subtidal sandbars. Shoreface nourishments on the other hand, which are typically placed on the seaward face of the pre-existing sandbar, quickly migrated onshore at rates up to 60 m/year, thereby pushing the pre-existing bar onto the intertidal beach. This behaviour is different from most observations of shoreface nourishment development along other parts of the Dutch North Sea coastline, where onshore migration of the nourishment is typically slow or absent.

The alongshore variability of sandbars at the Delfland coast in part depended on the bar crest depth. Sandbars in shallow water were more likely to exhibit three-dimensionality than sandbars in deep water. At the only mega nourishment in the dataset considered here, subtidal sandbars were found to exhibit high alongshore variability and clear alongshore differences in behaviour. Due to its large size, the mega nourishment changed the local coastline orientation with respect to the wave climate, leading to different sandbar dynamics compared to the adjacent parts of the Delfland coast.

3

TIDAL FLOW SEPARATION AT PROTRUDING BEACH NOURISHMENTS

In recent years, the application of large-scale beach nourishments has been discussed, with the Sand Motor in the Netherlands as the first real-world example. Such protruding beach nourishments have an impact on tidal currents, potentially leading to tidal flow separation and the generation of tidal eddies of length scales larger than the nourishment itself. The present study examines the characteristics of the tidal flow field around protruding beach nourishments under varying nourishment geometry and tidal conditions, based on extensive field observations and numerical flow simulations.

Observations of the flow field around the Sand Motor, obtained with a ship-mounted current profiler and a set of fixed current profilers, show that a tidal eddy develops along the northern edge of the mega-nourishment every flood period. The eddy is generated around peak tidal flow and gradually gains size and strength, growing much larger than the cross-shore dimension of the coastline perturbation. Based on a three-week measurement period, it is shown that the intensity of the eddy modulates with the spring-neap tidal cycle.

Depth-averaged tidal currents around coastline perturbations are simulated and compared to the field observations. The occurrence and behavior of tidal eddies is derived for a large set of simulations with varying nourishment size and shape. Results show that several different types of behavior exist, characterized by different combinations of the nourishment aspect ratio, the size of the nourishment relative to the tidal excursion length and the influence of bed friction.

Figure 3.1: The Sand Motor mega-nourishment in the Netherlands (left) just after construction in 2011, with turbidity patterns at the sea surface revealing signs of a separating tidal flow field, and (right) in 2014, after approximately 3 years of morphological development. Images by Joop van Houdt / Rijkswaterstaat.

3.1. INTRODUCTION

Beach nourishments have been applied world-wide as an effective method of mitigating coastal erosion problems for several decades already (Hamm et al., 2002). In recent years, large-scale multi-functional beach nourishments have been advocated based on morphological, ecological, recreational and economic arguments (Stive et al., 2013; De Vriend et al., 2015). Large beach nourishments protrude from the coastline and therefore cause strong interactions between the nourishment and the surrounding coastal hydrodynamics. Notably, the character of the tidal flow field around such large nourishments might change drastically, see Figure 3.1. Separation of shore-parallel periodic tidal flow at a perturbation and the associated formation of tidal eddies can have consequences for the morphological development of the coast (Pingree, 1978; Ferentinos and Collins, 1980) and the nourishment. Furthermore, if the nourishment represents a significant recreational value, concerns regarding the impact of tidal flow separation on swimmer safety might arise (Van den Hoek et al., 2014a). Finally, enhanced tidal mixing and spatially varying bed shear stresses can affect the mixing of nutrients (Signell and Geyer, 1990) and the quality of the benthic habitat (Nowell and Jumars, 1984). Adequate field observations and numerical parameter sensitivity studies of tidal flow perturbation by beach nourishments are currently lacking, which hampers prediction of the tidal flow field and related morphological, ecological and recreational impacts around nourishment sites.

    This study is aimed at examining the characteristics of the tidal flow field around protruding beach nourishments under varying nourishment geometry and tidal conditions. First, the behavior of the tidal flow field is assessed in a real-world situation based on a set of field observations, which were obtained near a particularly large beach nourishment in the Nertherlands (section 3.2 and 3.3). Multiple measurement techniques are combined to support interpretation of the spatio-temporally varying tidal flow field. Then, a numerical model is presented and compared to the field data (section 3.4). Subsequently, this model is employed to perform a parameter sensitivity study, examining the behavior of the tidal flow field (occurrence of flow separation and eddy formation) as a function of tidal flow characteristics and

the geometry of the perturbation (section 3.5).

Studies of the impact of beach nourishments on tidal flow are rare. This is mainly due to the fact that traditional beach nourishments generally have a cross-shore extent in the order of 100 meters, and therefore do not significantly obstruct alongshore tidal currents. The best analogy of tidal flow around a very large nourishment is found in studies of tidal flow around headlands. Pingree (1978) obtained field observations of tidal flow around a headland in the English Channel, showing that large eddies exist off the headland as a result of flow separation. Similar findings were reported based on observations with fixed current meters around headlands in the Bristol Channel (Ferentinos and Collins, 1980).

Geyer and Signell (1990) mapped tidal currents around Gay Head (MA, USA) and found large-scale eddies, which were formed as a result of tidal flow separation. These eddies are not shed from the coastline, as can be observed in flow past an obstruction in stationary flow, but remain in the near vicinity of the headland. Just after their formation around peak tidal flow the eddies are small, but they gradually grow in size to reach their maximum around slack tide. Subsequently, the eddy rapidly disappears as the tidal flow reverses. Spiraling secondary flow perpendicular to the main flow direction was found off the headland tip, forced by strong centrifugal accelerations (Geyer, 1993). An elaborate parameter sensitivity study was conducted by Signell and Geyer (1991), using a numerical model of the tidal flow around Gay Head. They identified four different flow regimes, depending on a combination of friction, the tidal excursion length and the headland geometry. The situation at Gay Head, with a tidal eddy remaining attached to the shoreline, was found to occur in case of high friction and a relatively large headland compared to the tidal excursion length. From the spreading of artificial, passive tracers in the same numerical model, Signell and Geyer (1990) concluded that flow separation around headlands can significantly enhance the dispersion of floating, suspended or dissolved matter.

Following similar observations around islands by Wolanski et al. (1984), tidal flow separation in island wakes was studied by various researchers. Black and Gay (1987) highlighted the role of the local streamwise pressure gradient in island wakes. Flow separation is the result of an adverse streamwise pressure gradient in wall-bounded flow (e.g. Simpson, 1989). Often the adverse pressure gradient is caused by decelerating flow downstream of an obstacle (e.g. a headland). However, as regions with strong tidal flows typically also experience significant tidal water level gradients, adverse pressure gradients and associated flow separation can also result from the vertical tide. Black and Gay (1987) found that in many cases, tidal eddies near an obstacle are driven by a combination of both mechanisms. They form initially due to decelerating flow downstream of the obstacle and subsequently grow larger under the influence of adverse large-scale tidal water level gradients. This is reflected by the behavior of the growing tidal eddies around Gay Head (Signell and Geyer, 1991). A similar influence of flow instationarity was shown to exist in laminar, oscillatory pipe flow along a wall disturbance (Sobey, 1983; Ralph, 1986), where an initial, separating eddy may interact with vorticity generated around flow reversal. Hench and Luettich Jr (2003) addressed the competition between various forcing mechanisms of tidal flow separation very illustratively by evaluating the terms

of the streamwise and transverse momentum balance around Beaufort Inlet (NC, USA). They underlined the streamwise balance between the pressure gradient and advective acceleration during the early ebb and flood phases and between the pressure gradient and local acceleration during the late ebb and flood phases.

Instationary tidal flow around these different perturbations can be described based on the dimensionless Keulegan-Carpenter number K_C (Equation 3.1) and the dimensionless disturbance aspect ratio α (Equation 3.2),

$$K_C = \frac{U_p T}{L_a} \tag{3.1}$$

$$\alpha = \frac{L_c}{L_a} \tag{3.2}$$

where U_p represents the off-shore peak tidal flow velocity, T is the tidal period, L_a is the alongshore disturbance length scale (the disturbance being a headland, nourishment, island, etc.) and L_c is the cross-shore disturbance length scale. L_a is measured parallel to the overall coastline orientation between the disturbance tip and the point where it connects to the surrounding coastline. The value of K_C can be regarded as the relative importance of advective acceleration compared to local acceleration, or alternatively as the tidal excursion length over the streamwise disturbance length. A small value of K_C indicates a large disturbance size compared to the tidal excursion. Likewise, if K_C is large, the distubance size is small compared to the tidal excursion. The interpretation of α is straightforward, with a larger value indicating a more pronounced disturbance shape and a smaller value indicating a less pronounced disturbance shape.

Beach nourishments are typically situated along sandy shelf coasts. The water depth in these environments is relatively shallow. Wolanski et al. (1984) and Tomczak (1988) suggested that the importance of bottom friction can be expressed through a shallow water Reynolds number Re_z (Equation 3.3), which was found to correlate well with different types of island wake behavior observed by Wolanski et al. (1984) and Pattiaratchi et al. (1986).

$$Re_z = \frac{U_p H^2}{K_z L_c} \tag{3.3}$$

In Equation 3.3, H denotes the water depth and K_z is the vertical diffusion coefficient, which is calculated here with the formulation suggested by Wolanski et al. (1984). Essentially, Re_z expresses the relative importance of advection compared to bottom friction. This study will expand existing studies by focusing particularly on the role of disturbance size and shape, which may vary strongly between different nourishments. Characteristics of the separating tidal flow field (eddy size, strength and lifetime) will be quantified under a large, realistic range of conditions (expressed by the value ranges of K_C and α), thereby placing earlier qualitative findings in a broader perspective. Large variations in Re_z are not taken into account, because the cross-shore beach profile around beach nourishments is generally mild and the influence of bottom friction is relatively high (values of Re_z considered in

this study are $\mathcal{O}(1)$). Instationarity of the tidal flow is shown to be more important than variable bed friction under these circumstances.

3.2. FIELD SETUP

Field observations for this study were obtained around the Sand Motor (Stive et al., 2013), a mega-scale beach nourishment situated at the Dutch coastline south of The Hague in the Delfland coastal cell. The Sand Motor was constructed in 2011 as a 17.5 Mm^3 hook-shaped peninsula. It is expected to nourish the adjacent coastline throughout the coming decades, relying on natural sediment transport processes to spread the sand.

The Delfland coastal cell is a 20 km stretch of North Sea coastline, located in between the Rotterdam and The Hague harbor breakwaters at the southern and northern end respectively (Figure 3.2). The Sand Motor mega-nourishment was originally constructed between 6 and 8 km south of The Hague, but has meanwhile extended its signature through alongshore sediment transport (Figure 3.1). Its approximate aspect ratio in September 2014 was $\alpha \sim 0.3$. The foreshore is shallow, with the 15 m depth contour located 5 km off-shore. The Delfland coast is a micro-tidal environment, the tidal range varying between 1.8 and 1.4 m over one spring-neap cycle (Wijnberg, 2002). The tide at the southern North Sea is a counter-clockwise rotating Kelvin wave, which drives tidal currents in alongshore direction (flood current directed to the North-East along the Delfland coast). Depth-averaged peak tidal currents are in the order of 0.7 m/s and the phase difference between the surface elevation and tidal currents is close to zero degrees.

Just south of the Rotterdam harbor breakwater, the main outflow of the Rhine river is located (Figure 3.2). This outflow is associated with a considerable freshwater runoff of on average 2200 m^3/s. The resulting, tidally pulsating freshwater plume regularly approaches the shoreline near the Sand Motor and constitutes a region of freshwater influence (ROFI), which stretches northward along the entire Dutch coast (Souza and Simpson, 1997). The presence of freshwater induces temporally varying vertical and horizontal density gradients (De Boer et al., 2006).

In order to determine the characteristics of the tidal flow field around the northern half of the Sand Motor, a set of field measurements was obtained in September and October 2014 during the large, multi-disciplinary Mega-Perturbation Experiment (MegaPEX). Part of the instrument setup is presented in Figure 3.2.

An alongshore array of four upward looking acoustic doppler current profilers (ADCP's) was deployed stretching from the tip (i.e. most seaward point) of the Sand Motor to a location 3.5 km farther north-east. The ADCP profile measurements provided continuous timeseries of flow velocity. Stations A5 and B3 were located at 4 m depth, station E at 6 m and station F at 9 m. Table 3.1 lists the properties of all four current profilers. 15-minute averaged flow velocities were linearly interpolated to mid-depth values, based on the instantaneous water level and local water depth, to obtain a proxy for the depth-averaged flow velocity. Actual depth averaging over the ADCP bins was considered inappropriate, as the shallow ADCP moorings did not always cover a representative part of the water column to justify depth averaging. A comparison was made between mid-depth velocities and depth-averaged veloc-
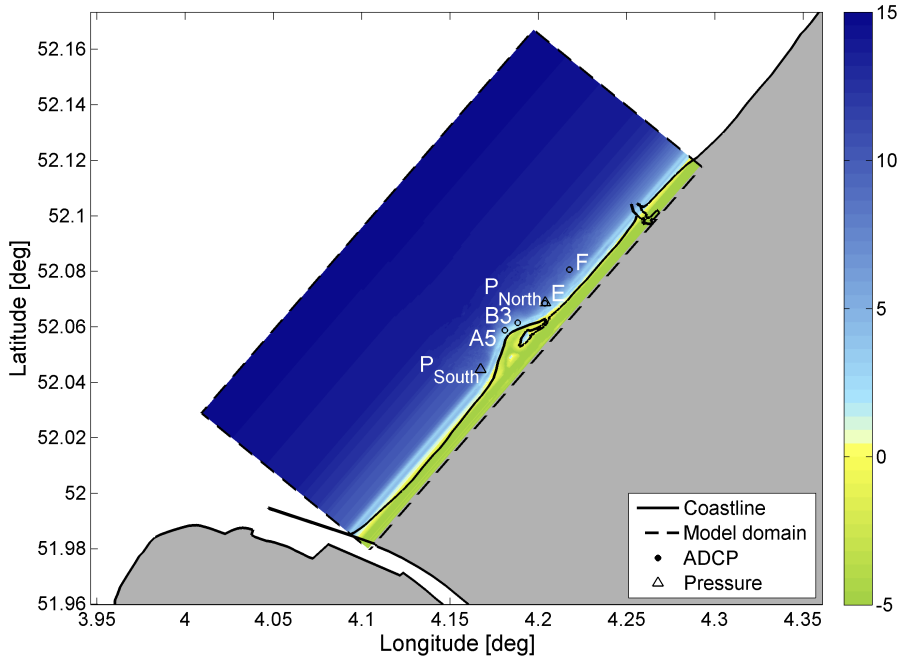
Figure 3.2: Overview of the Delfland coastal cell, the instrument setup and the numerical model domain (dashed lines). Shading inside the model domain marks the model bathymetry. The solid line indicates the real-world position of the coastline as a reference. The harbour moles of Rotterdam and The Hague, which are visible in the real-world coastline, have been omitted in the model.

ities at stations E and F, which had a relatively large coverage of the water column compared to A5 and B3. The correlation coefficient between both parameters for the full deployment period equals 0.99 (significant to the 95% confidence level) at both stations for alongshore velocities with an RMSE of 2 cm/s at E and 3 cm/s at F, while the correlation coefficient for cross-shore velocities is 0.95 at E and 0.68 at F (both significant to the 95% confidence level), with an RMSE of 2 and 3 cm/s respectively. As this study primarily focuses on alongshore velocity components, the use of mid-depth velocities is considered appropriate.

Pressure transducers were located north and south of the Sand Motor (P_{north} and P_{south}) at 6 and 9 m depth respectively, see Figure 3.2. The 15-minute averaged pressure data were used to determine tidal water levels throughout the measurement period.

Next to the fixed instruments, a 13 hour ship-mounted ADCP campaign was conducted on 27 September. Every hour a set of transects was surveyed by the ship. The measurement domain gradually shifted northward as the tidal current turned from ebb to flood. This resulted in (tidal) flow measurements at a high spatial resolution, covering one full tidal cycle. Properties of the downward-facing 600 kHz ADCP are given in Table 3.1. The position and orientation of the ship was measured

Table 3.1: ADCP characteristics

Station	Water depth	Bottom bin center	Bin height	Averaging time
A5	4 m	−3.2 m	0.5 m	1 sec
B3	4 m	−2.6 m	0.5 m	1 sec
E	6 m	−4.1 m	0.5 m	5 min
F	9 m	−6.2 m	0.5 m	5 min
Ship	n/a	n/a	0.25 m	2 sec

with a real-time kinematic differential GPS (RTK-DGPS) and a gyroscope-corrected compass. Observed flow velocities were corrected for the navigation speed of the ship by making use of the ADCP's bottom tracking functionality. Along the ship's navigation tracks, data were interpolated to discrete grid points. The velocity at a grid point was determined from ADCP profiles obtained within 100 m from that point, using interpolation weights based on the reciprocal distance to the grid point. Finally, velocities were averaged over all vertical bins to obtain the depth-averaged velocity.

These in-situ observations were complemented with data from an X-band radar station, which was situated on top of a dune just north of the Sand Motor. Time-averaged backscatter intensity images (e.g. Dankert et al., 2003; Haller et al., 2014) have supported a qualitative understanding of flow patterns around the Sand Motor. A sequence of these images can be found in Radermacher et al. (2015), but further analysis of the radar data is omitted here.

3.3. Field observations

First, the ship-mounted ADCP data are presented. Due to its high spatial resolution, this dataset provides a synoptic overview of the tidal flow pattern. Subsequently the fixed ADCP dataset, which is sparse in space but has a higher temporal resolution and coverage, provides flow characteristics over the course of multiple tidal cycles.

The ship-mounted ADCP data were collected on 27 September 2014. On this day, the tidal range was relatively large (1.6 m, spring tide), wave energy was low (0.5 m significant wave height) and winds were weak (2.5 m/s wind velocity at 10 m above sea level). This implies a dominant role of the tidal forcing of the flow compared to other forcing mechanisms (waves and wind). The data are therefore suitable to study the tidal flow field around the Sand Motor.

Six consecutive flow fields that were measured with the ship-mounted ADCP during the flood phase of the tide are shown in Figure 3.3. Every panel shows measurements obtained within half an hour from the given timestamp. At 16:30 hours, the observed depth-averaged flow vectors show the initiation of tidal flow separation and reversal of the flow direction along the leeward edge of the nourishment. From that moment onward, a tidal eddy starts to develop. The eddy grows in alongshore and cross-shore extent, eventually extending well beyond the most seaward point of the Sand Motor (19:30 hours) and enhancing further contraction of the main flood flow. Towards slack tide, the flow velocity in the eddy decreases, while
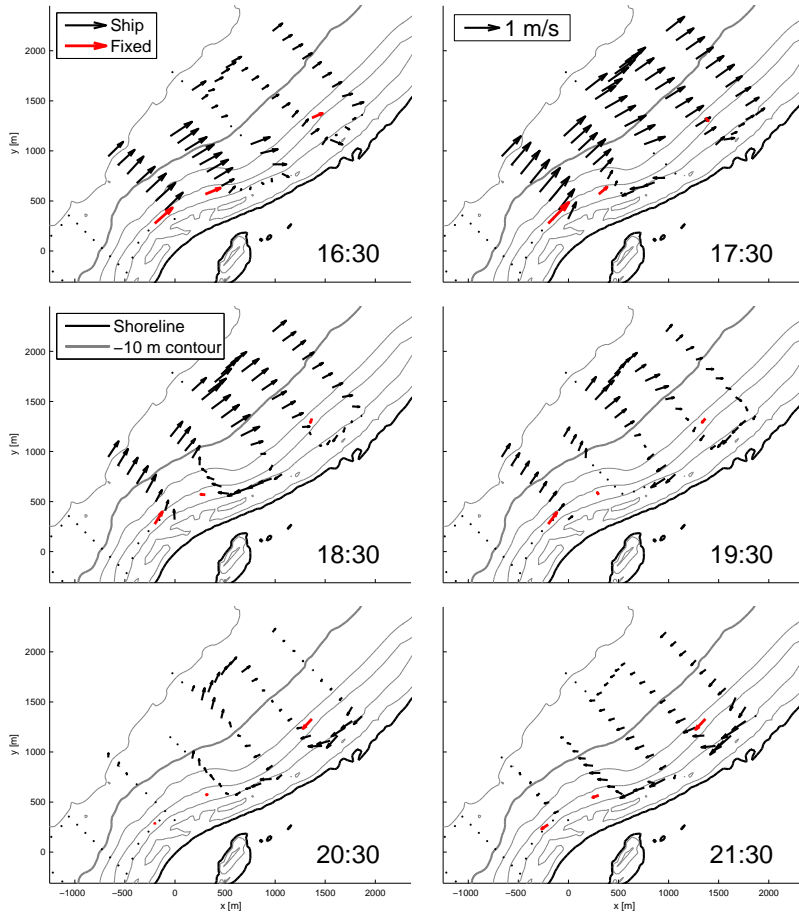
Figure 3.3: ADCP velocity vectors on 27 September 2014. Contours represent the bathymetry.

the eddy still grows in size (20:30 hours) and ceases to exist (21:30 hours). Measurements obtained during the ebb phase do not extend far enough in southern direction to properly cover the flow field downstream of the mega-nourishment and are therefore not shown.

The temporal behavior of the flow is examined in more detail with timeseries of 15-minute averaged surface elevation, alongshore pressure gradient and alongshore flow velocities at mid-depth from all four fixed ADCP stations on 27 September 2014 (Figure 3.4). During early flood, alongshore flow velocities at the four locations rise similarly, until approximately 16:30 hours. The peak flood velocity at station A5 is 0.25 to 0.35 m/s higher than the peak flood velocity at the other three stations. The fall of alongshore flow velocity at stations B3 and E sets in earlier than at the other two stations and turns negative 1.5 (E) to 2.5 (B3) hours before flow reversal at A5 and F. This coincides with flow separation and eddy formation (Figure 3.3), with B3

Figure 3.4: Observed timeseries of surface elevation w.r.t. chart datum (approximately mean sea level) at station B3 (upper panel), alongshore water level gradient $\partial\eta/\partial y$ computed from the pressure sensors (middle panel) and alongshore flow velocity at 4 different stations (lower panel, positive velocities in flood direction). All timeseries represent 15-minute running averages and were observed on 27 September 2014. Six vertical lines indicate the times of the flow fields shown in Figure 3.3.
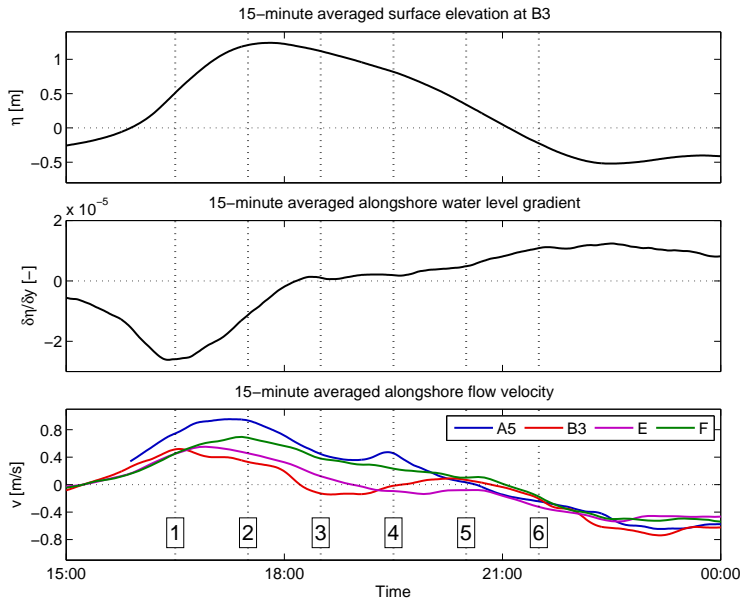
and E being temporarily situated in the return flow of the eddy. It takes about two hours before the eddy has gained enough size (approximate diameter larger than 1 km) to cover stations B3 and E (Figure 3.3). At station F, the peak flood velocity is lower than at station A5. This difference can be attributed to accelerated tidal flow at A5 due to flow contraction. In addition, the tidal flow requires a certain distance downstream of the eddy to recover from flow separation. Within this lee zone, peak flow velocities are relatively low.

The local maximum in the alongshore flow velocity signals around 19:30 hours at stations A5 and B3 cannot be explained by the tidal forcing alone. Most probably, these local peaks are related to the passage of the freshwater plume of the river Rhine. From analysis of time-averaged X-band radar imagery, it was confirmed that the front of the plume reaches the tip of the Sand Motor at that time. Furthermore, similar velocity peaks occur regularly at all four stations, including station F, which is located well outside the region of separating flow. Hence, it is unlikely that the observed alongshore velocity peaks are related to eddy dynamics. The effect of stratification on the tidal currents is outside the scope of this study, which focuses on tidal flow separation.

The clearest indication of flow separation in these timeseries is given by the negative alongshore flow velocities at stations B3 and E during the late flood phase. This
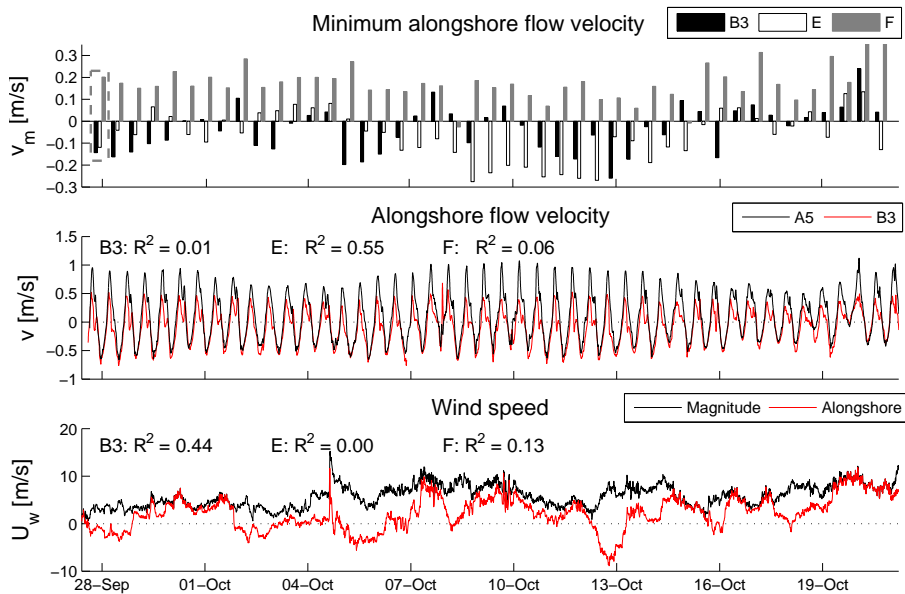
3

Figure 3.5: Long-term analysis of the fixed ADCP timeseries. The minimum alongshore velocity parameter (v_m, upper panel) is shown for stations B3, E and F. The middle panel shows the full timeseries of alongshore flow velocity at stations A5 and B3, including squared correlation coefficients between v_m and the peak tidal flow velocity at A5 during every individual tidal cycle. The lower panel shows wind speed magnitude and alongshore wind speed (positive alongshore winds coming from the South-West), including squared correlation coefficients between v_m and the alongshore wind speed averaged over every individual tidal cycle. The tidal cycle containing the ship-mounted ADCP measurements is boxed in the top panel.

signature indicates whether flow separation occurs at every tidal cycle in the three-week deployment period. The minimum (i.e. most negative) alongshore flow velocity v_m occurring at B3, E and F over the late flood phase is determined for every tidal cycle (Figure 3.5). The late flood phase is defined between 1 hour before the high water peak (HW) and 2 hours after HW. The results presented here showed to be rather insensitive to the exact definition of the late flood phase.

Flow reversal during the late flood phase (i.e. negative values of v_m) rarely occurs at station F, whereas this effect is present during most tidal cycles at B3 and E. At station E, a significant modulation of v_m with the peak alongshore flow velocity at A5 can be observed ($r^2 = 0.55$, significant to the 95% confidence level), showing that the circulation of the eddy intensifies during spring tide. A strong correlation between v_m and the tidal range is absent at the other stations, most probably due to the fact that B3 is positioned at the edge of the tidal eddy while F is positioned outside the eddy. While winds were rather weak during the periods addressed in Figures 3.3 and 3.4, stronger winds occurred later on during the measurement period. A moderate correlation is found between the alongshore wind speed and v_m at station B3 ($r^2 = 0.44$, significant to the 95% confidence level), while this correlation is very weak or

absent at the other stations. Possibly, the presence of alongshore winds leads to slight horizontal shifts in eddy position, locating B3 further inside or outside the eddy. As tidal currents are the focal point of this study, the influence of wind on tidal eddy behavior is not considered here in further detail.

3.4. NUMERICAL MODEL SETUP AND COMPARISON TO FIELD DATA

A numerical model is employed to fill in spatial and temporal details of the field data and to study scenarios involving different nourishment geometries and tidal characteristics. The outline of the model is presented in this section, together with a comparison of computed tidal currents and the field observations.

3.4.1. MODEL SETUP

The depth-averaged (2D-horizontal) model is constructed with the modeling package Delft3D (Lesser et al., 2004), which numerically integrates the shallow water equations. The parameter sensitivity study (section 3.5) is aimed at assessing the tidal flow around various nourishment geometries in different tidal environments at an alongshore uniform coastline. This requires a schematized model setup, without the specific characteristics of the Delfland coast (Figure 3.2). The nourishment geometry was superimposed on an alongshore uniform coastal bathymetry, with a cross-shore depth profile which is representative of the average profile along the Delfland coast. Prescribed water levels along the off-shore boundary were interpolated from timeseries at both off-shore corners, ensuring that a tidal phase difference builds up along the boundary. The lateral boundaries were forced with Neumann conditions, which prescribe the alongshore water level gradient. This gradient was calculated from the difference between the water levels in both corner points divided by the alongshore domain length. Although this method does not exactly reproduce the local gradients along the cross-shore boundaries, the model is found to be rather insensitive to the Neumann boundaries. Water levels at the off-shore corner points were obtained from the Continental Shelf Model and the nested Dutch Coast Model (Sembiring et al., 2015), which were forced with astronomic water levels at the Western European continental shelf break.

For the parameter sensitivity study, artificial timeseries of water levels were imposed at the off-shore corner points. These timeseries were constructed from the M2 constituent only. The M2 phase difference between both off-shore corner points, which drives the alongshore tidal currents in the model domain, was derived from the Dutch Coast Model.

Friction is specified using the White-Colebrook formulation with wall roughness height parameter $k = 0.025$ m, which has been calibrated by minimizing the root-mean-squared error between modeled and observed (fixed and ship-mounted ADCP's) currents and water levels. The model calculates spatially and temporally varying turbulent viscosities based on Horizontal Large Eddy Simulation (Uittenbogaard and Van Vossen, 2003) with an averaging duration of 30 minutes and a background viscosity of 0.01 m^2/s. All model simulations were initiated with an 11 day spin-up

period, which allowed the model to reach stable conditions.

The model bathymetry applied to compare the model with field data was based on bi-monthly RTK-DGPS surveys of the Sand Motor. The GPS instrumentation was mounted on a personal watercraft with a single-beam echo sounder for the sub-aqueous parts of the measurement domain and on an all-terrain vehicle for the dry beach (De Schipper et al., 2016). These data were interpolated to the rectangular model grid, which has a variable spatial resolution depending on the size of the modeled perturbation, such that the cross-shore size of the perturbation spans at least 10 grid cells. A numerical time step of 12 seconds was applied. Further grid refinement and shorter time steps were tested, but the model was found to be insensitive to these changes. For the parameter sensitivity study, artificial nourishment designs were constructed using a cosine-shaped shoreline perturbation with a period (i.e. alongshore length scale) of $2L_a$ and an amplitude (i.e. cross-shore length scale) of $L_c/2$.

3.4.2. COMPARISON TO FIELD DATA

The numerical model was compared to the field observations presented in section 3.3. Comparison to the fixed ADCP velocities primarily indicates if the model is able to reproduce the basic alongshore tidal flows, although especially alongshore velocity timeseries at stations B3 and E also contain a clear signature of tidal flow separation and eddy formation. The ability of the model to reproduce the formation and development of tidal eddies is addressed more extensively by comparing model results to the ship-mounted ADCP dataset.

First, three-day timeseries from two ADCP stations and one pressure sensor are examined (Figure 3.6). South-easterly to south-westerly winds ranged between 3 and 6 m/s over the three-day period shown in the figure. During the same period, the off-shore wave height increased from 0.3 to 0.9 m. Modeled surface elevations largely show the same behavior as the observed surface elevations (top panel of Figure 3.6). Computed alongshore flow velocities at both stations shown in the figure compare well with the observed values in terms of amplitude, phase and tidal asymmetry (middle panel). The weak winds and low waves present during the three-day analysis period have very limited impact on the observed alongshore flow, implying that the flow field is dominated by the astronomic tide.

Cross-shore velocities computed by the model show slightly larger deviations with respect to the observed flow velocities (lower panel of Figure 3.6). Off-shore velocity peaks during the ebb phase are underestimated by the model. Secondary forcing mechanisms like stratification and curvature-induced circulation, which are omitted in the schematized model, may impact the relatively weak cross-shore flows during this phase of the tide. In the timeseries of alongshore flow velocity the influence of these forcing mechanisms is not visible, except for the positive peak during the late flood phase. As noted before, comparison with X-band radar imagery (Radermacher et al., 2015) suggest that these peaks coincide with the arrival of the freshwater front.

Error metrics over the full measurement period (Table 3.2) show that at all four fixed ADCP stations, alongshore flow velocities are predicted with a root-mean-
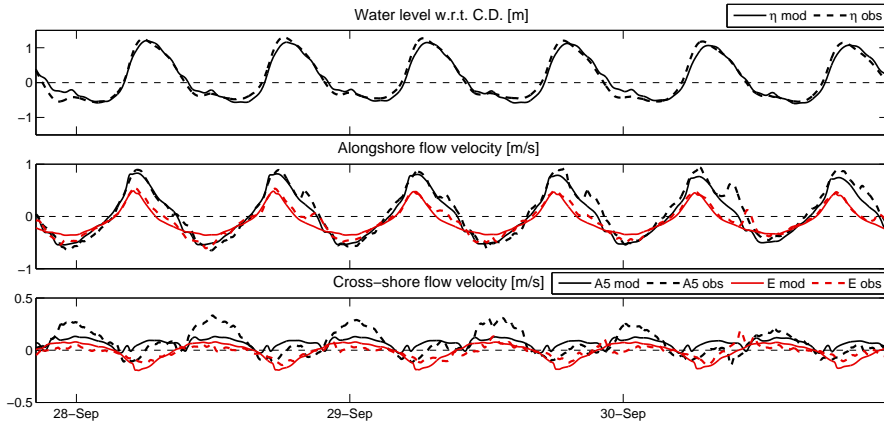
Figure 3.6: Comparison of model results (solid lines) to pressure sensor and ADCP field observations (dashed lines). Computed parameters are compared to surface elevations from pressure sensor P_{south} (upper panel) as well as alongshore (middle panel) and cross-shore (lower panel) depth-averaged flow velocities from ADCP A5 and E. Positive velocities indicate flow in flood and off-shore direction respectively.

Table 3.2: Timeseries error statistics

Station	RMSE	Alongshore RMSE	Cross-shore RMSE	Record length
A5		0.079 m/s	0.150 m/s	23.36 days
B3		0.080 m/s	0.131 m/s	23.40 days
E		0.057 m/s	0.121 m/s	34.42 days
F		0.046 m/s	0.107 m/s	34.52 days
P_{north}	0.218 m			33.19 days
P_{south}	0.218 m			33.21 days

squared error between 0.05 and 0.08 m/s, giving confidence in model skill regarding alongshore tidal flow. The relative error in modeled cross-shore currents, which are one order of magnitude smaller than alongshore currents, is clearly larger. The difference between modeled and observed cross-shore currents is thought to be largely related to stratification and secondary circulations, as commonly observed in river bends and around headlands (Geyer, 1993). These vertical circulations cannot be captured by the 2D-horizontal numerical model.

The quality of the spatial flow fields calculated by the model is assessed by comparing model outcomes to the ship-mounted ADCP observations. Computed flow velocities were collected at the same spatial grid points as shown in Figure 3.3, taking into account the time lag between subsequent velocity profile samples along the ship's navigation tracks (Figure 3.7). Generally, the model is able to predict the separating tidal flow field, in terms of spatial structure as well as timing. Modeled swirling strength fields, computed as the complex part of the eigenvalues of the velocity gradient tensor (e.g. Henriquez et al., 2014) support interpretation of eddy development. The visual comparison of velocity vectors is quantified by direct

3
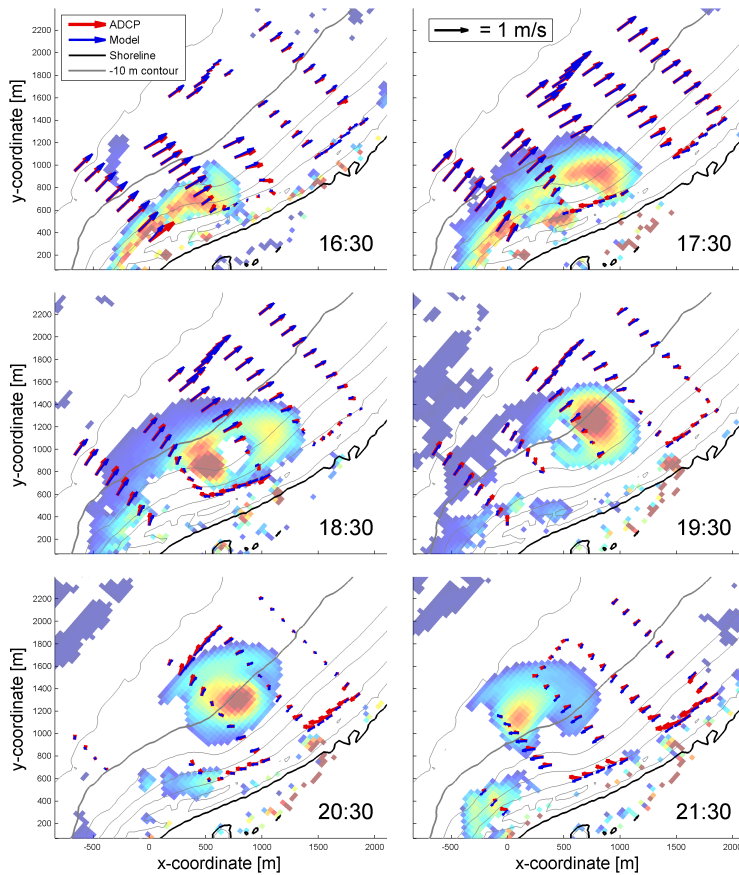
Figure 3.7: Comparison of model results to depth-averaged ship-mounted ADCP observations at six different moments during the flood phase. Projected local coordinates are provided along the axes. The shading represents swirling strength derived from the numerical model results to help interpretation of the flow fields. The maximum swirling strength λ_{ci}, indicated in yellow, amounts 1.0^{-3} s^{-1}.

comparisons of computed and observed velocity magnitude and direction (Figure 3.8), which are composed of all gridded velocity data points throughout the 13-hour measurement period. Root-mean-squared errors of flow velocity magnitude are 0.05 and 0.06 m/s during the ebb and flood phase respectively. Around slack tide, the error is slightly higher (0.10 m/s). Flow velocity directions show larger deviations (left panel of Figure 3.8), although the bulk of the data points still shows good agreement between the model and the observations. Altogether, the 2DH model forced with astronomic tidal boundary conditions accurately predicts spatial and temporal evolution of the tidal flow field around the Sand Motor, including the occurrence of flow separation and eddy formation.

Figure 3.8: Direct comparison of flow velocity magnitude and direction from model results against ship-mounted ADCP observations. The different data point markers indicate different phases of the tidal flow. Root-mean-squared errors are indicated in the figure. Data points with a velocity magnitude below 0.1 m/s have been omitted from the right panel.
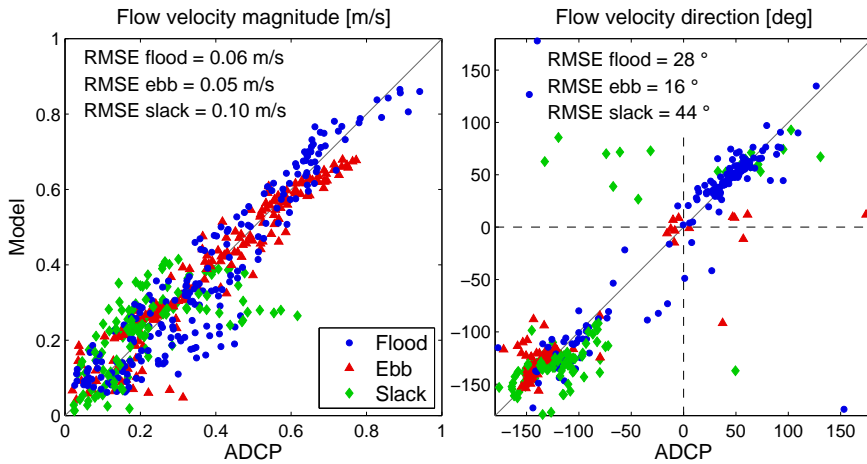
3.5. SIMULATED TIDAL FLOWS AROUND COASTLINE PERTURBATIONS

A general understanding of the impact of protruding beach nourishments on the tidal flow is created based on numerical model simulations. First, a set of parameters is defined to characterize the degree of disturbance of the tidal flow field by the nourishment by quantifying the size, strength and longevity of generated tidal eddies.

Several methods for definition and detection of eddies in an instationary flow field were considered. Often, eddy dynamics are studied from parameters that are based directly on the velocity gradient tensor (e.g. vorticity, Long and Özkan-Haller (2009); swirling strength, Henriquez et al. (2014); vector potentials, Talstra (2011)). Reliable, automated quantification of eddy size and longevity from such parameter fields proved to be difficult. The most consistent agreement with visual eddy identification was obtained using cross-shore profiles of alongshore flow velocity v (Figure 3.9). The full analysis procedure makes use of 10 equally spaced transects on either side of the nourishment between the tip and the connection with the surrounding shoreline. The presence of a return flow in the shoreward part of the profile is taken as an indication of the presence of a tidal eddy. The size of the eddy L_e is defined by integrating these profiles in cross-shore direction until a zero net discharge is found. The maximum value found over 10 cross-shore profiles is assigned to L_e, which is made dimensionless through dividing by the cross-shore nourishment size L_c, resulting in dimensionless eddy scale ℓ_e. Furthermore, the strength of the eddy is characterized by the maximum swirling strength λ_{ci} found in the region delineated by the first and last cross-shore velocity profile (Figure 3.9) and the -1.5 m
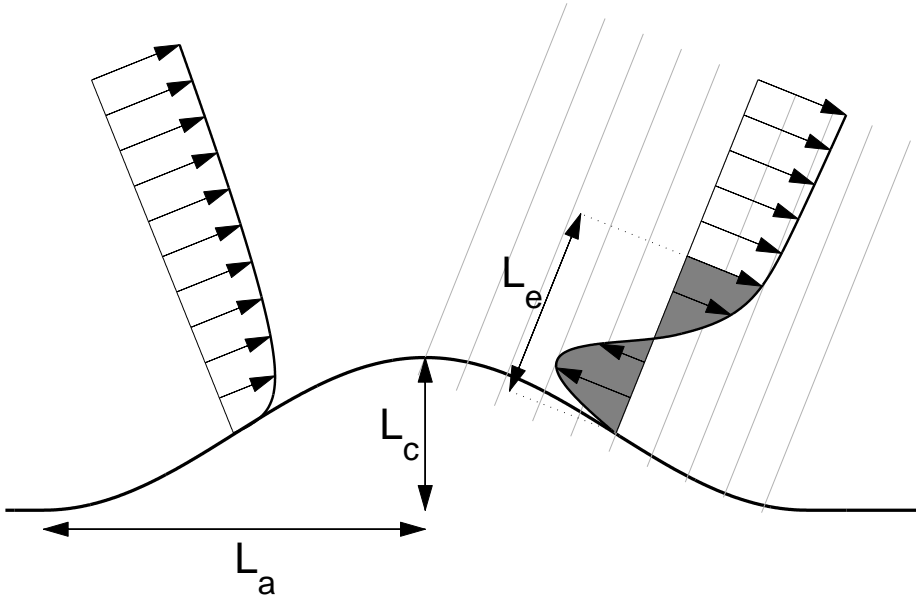
3

Figure 3.9: Definition of parameters characterizing eddy size, based on ten downstream cross-shore transects of tidal flow velocity at the pressure switch. Velocity profiles in one upstream and one downstream transect are shown as an example.

and -12 m water depth contours. It has been confirmed from visual inspection that this definition leads to the maximum λ_{ci} near the eddy core if the flow separates. Swirling strength can be interpreted as the inverse rotation timescale of a vortex, which is then scaled with an inverse timescale relating to the perturbation U_p/L_c to obtain dimensionless eddy intensity Λ. As for the calculation of K_C and Re_z, U_p is defined here in an off-shore grid cell, far away from the perturbation.

The evolution of ℓ_e and Λ over one tidal half-cycle in a baseline simulation (Tidal amplitude of 0.5 m, deep water tidal flow velocity amplitude of 0.35 m/s, $L_a = 1000$ m, $L_c = 300$ m) is now treated as an example (Figure 3.10). The tidal eddy on the downstream side of the nourishment is initiated around the peak of the main tidal flow at 0.5 hours, well before the large-scale pressure gradient changes sign and turns adverse. Hence, in this simulation, tidal eddies are generated by a local adverse pressure gradient in the lee of the nourishment as a result of lateral flow expansion. ℓ_e grows at a constant rate until the large-scale pressure gradient changes sign at 3.2 hours (this moment is henceforth referred to as the *pressure switch*). From the pressure switch onwards, ℓ_e grows exponentially, supported by the large-scale adverse pressure gradient. Eddy intensity Λ is relatively low at the moment of eddy formation, but grows rapidly to reach its maximum value at the pressure switch. After the pressure switch, the main flow is not forced anymore and the eddy intensity is reduced, while the return flow keeps expanding and smoothly evolves into the next phase of the tidal flow.
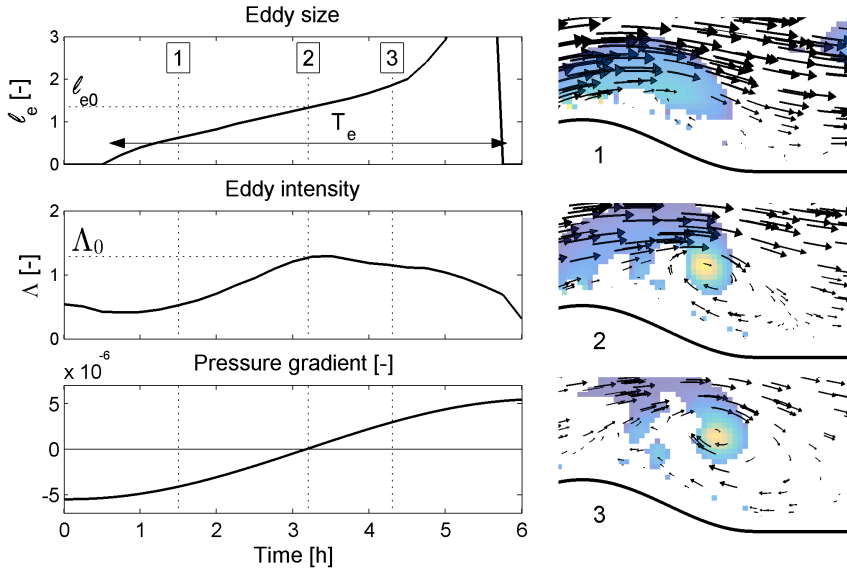
Figure 3.10: Timeseries of ℓ_e (upper left panel), Λ (middle left panel) and domain-averaged alongshore pressure gradient (lower left panel). Vertical dotted lines indicate the times of three flow fields shown in the right panels. Line number 2 is situated at the pressure switch. A positive pressure gradient supports ebb flow (right to left), a negative pressure gradient supports flood flow (left to right). Shading in the right panels represents computed swirling strength.

Three parameters are now extracted from these timeseries of ℓ_e and Λ, such that one parameter value is obtained for every tidal half-cycle (one during flood flow and one during ebb flow). ℓ_{e0} is the downstream value of ℓ_e at the pressure switch. A non-zero value of ℓ_{e0} indicates that the initiation of the tidal eddy is caused by a locally adverse pressure gradient due to lateral flow expansion rather than a large-scale adverse pressure gradient due to the tide. The larger ℓ_{e0}, the larger the tidal flow disturbance caused by the nourishment. Analogous considerations hold for Λ_0, the value of Λ at the pressure switch: a larger value means stronger disturbance. The third parameter is the total lifetime duration of the eddy, indicated in the upper panel of Figure 3.10. It is expressed by T_e, and made dimensionless with the tidal period T, resulting in dimensionless eddy lifetime τ_e.

These three parameters, which describe the process of tidal flow separation for every tidal half-cycle, are now used to create a generic picture of tidal flow separation around a beach nourishment of arbitrary size and shape in an arbitrary tidal environment. A set of 29 numerical model runs with varying K_C (i.e. varying nourishment size relative to the tidal excursion, Equation 3.1) and varying α (i.e. varying nourishment shape, Equation 3.2) is evaluated (Figure 3.11). K_C is varied by changing L_a, while α is varied by changing L_c. Well-developed eddies, with a lifetime $\tau_e > 0.35$, are found for pronounced perturbations ($\alpha > 0.15$). Relative eddy size ℓ_{e0} is largest for small nourishments compared to the tidal excursion length. For $K_C > 33$ and $\alpha > 0.2$, eddy size at the pressure switch is more than twice as large
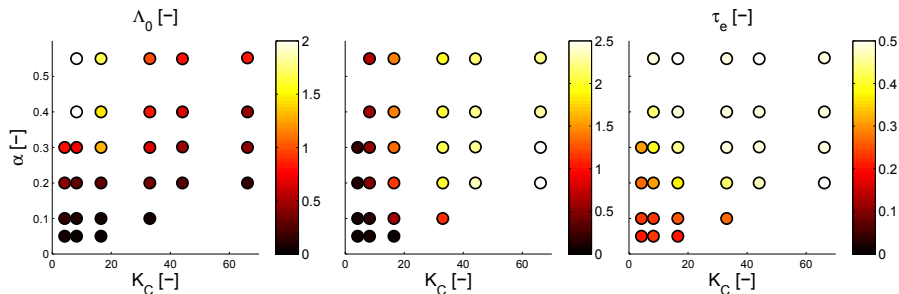
Figure 3.11: Various eddy characteristics as a function of K_C and α. The left panel shows Λ_0, the middle panel shows ℓ_{e0} and the right panel shows τ_e. Shaded markers show actual data points obtained from numerical simulation, a lighter color indicating stronger disturbance. These parameter values were derived from the flood half-cycle.

as the cross-shore nourishment dimension. For very mild perturbations ($\alpha < 0.15$), no significant eddy formation takes place before the pressure switch. Eddy intensity Λ_0 is close to zero and eddy lifetime is short. Local adverse pressure gradients downstream of the nourishment tip are absent or too weak to induce flow reversal. Similarly, for very large perturbations ($K_C < 5$), no significant eddy development is found given the small eddy size and lifetime. The alongshore perturbation dimension is very large compared to the tidal excursion length. As a result, the flow field is not given enough time to spin up during a tidal half-cycle. Local accelerations dominate advection and the flow experiences the nourishment as a smooth coastline modulation. Maximum eddy intensity is found in the upper left corner of the K_C-α plane. This implicitly shows that eddy intensity increases with increasing L_c (given that the flow separates), as the largest cross-shore perturbation dimensions and eddy intensities are found for small K_C and large α. These perturbations with large L_c extend into deeper waters, which decreases the influence of friction and therefore allows for more intense eddies.

Visualized flow fields at the pressure switch aid interpretation of these results (Figure 3.12). Pronounced perturbations (large α) are found to generate circular eddies, while the eddy shape is elliptic in case of mild perturbations (small α). For relatively large perturbations (small K_C), the eddy remains close to the perturbation tip. In contrast, if the perturbation is relatively small (large K_C), the eddy core drifts farther downstream and expands into the lee zone behind the perturbation. This expansion explains the large eddy size found for large K_C.

3.6. DISCUSSION

The model results presented in the previous section can be schematized into several different characterizations of the tidal flow field, depending on the values of K_C and α (Figure 3.13). For sufficiently large or mild nourishments (low K_C or α), the coastline perturbation is not pronounced enough to induce tidal flow separation before the pressure switch. The transitional value for α is found between 0.1
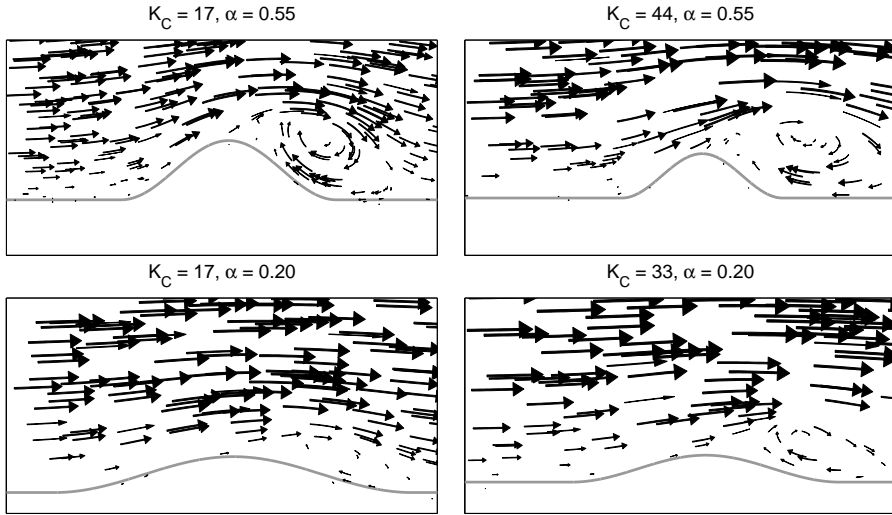
Figure 3.12: Comparison of the tidal flow field at the pressure switch for four runs with different K_C and α. The vector arrows are aligned with the local streamlines and provide an indication of the flow field. Arrow length and thickness increase with increasing flow velocity.

and 0.2, which is similar to the empirical limit of 1/6 to 1/8 for separation of stationary flows (e.g. Chandavari and Palekar, 2014). These results suggest that the instationary character of the flow does not affect this limit aspect ratio for flow separation. Within the parameter range where flow separation occurs before the pressure switch, several different types of eddy dynamics can be discerned. For relatively large perturbations (regions 1 and 3 in the figure), the eddy stays close to the nourishment tip and remains limited in size compared to the nourishment dimensions. For smaller perturbations (regions 2 and 4), the eddy expands towards the adjacent coastline downstream of the nourishment, allowing for a large eddy size compared to the nourishment. If the nourishment size is decreased further (region 5), the flow becomes semi-stationary and tidal eddies are shed off the perturbation. This regime mainly occurs outside the parameter space of the sensitivity study presented in the previous section, but is added for the sake of completeness. If the nourishment is very pronounced (regions 1 and 2), the eddy has a circular shape. For milder nourishments (regions 3 and 4), the eddy becomes more elliptic, with its cross-shore dimension significantly shorter than its alongshore dimension.

The analysis of separating tidal flow fields under varying perturbation shape and for a wide range of K_C values elaborates upon the conceptual picture presented by Signell and Geyer (1991) for a pronounced headland ($\alpha = 4$). Their case with high friction and low K_C corresponds to region 1 in Figure 3.13. The other regions in the figure are a transitional case of their framework (region 2) or describe less pronounced aspect ratios (region 3 and 4). Vortex shedding, as predicted by Signell and Geyer (1991) in model simulations with low friction, did not occur in most model
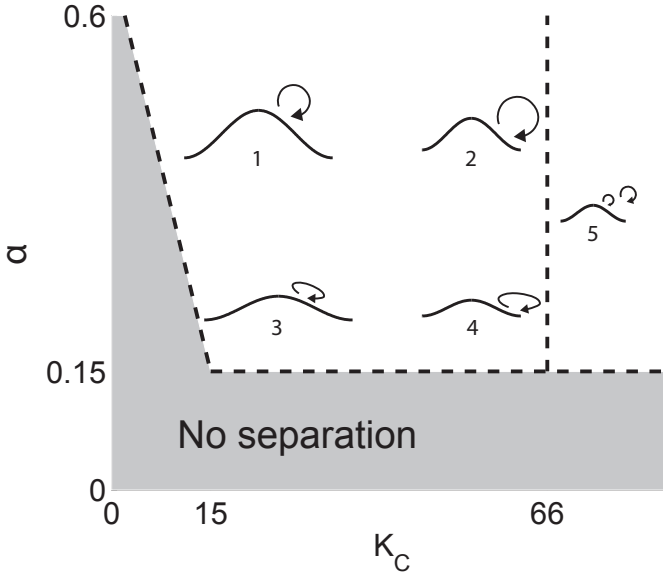
Figure 3.13: Generalized overview of the tidal flow disturbance by beach nourishments as a function of K_C and α. Approximate transitional values are given along the axes. Gradual transition zones exist between the regions indicated in the diagram. The vertical line at $K_C = 66$ indicates the extent of the modeled parameter space.

simulations of the present study. Only at $K_C = 66$ the tidal eddies started to exhibit instabilities, which has been identified as a transitional case to vortex shedding at intermediate values of the shallow water Reynolds number Re_z by Wolanski et al. (1984). The low-friction regime is considered less relevant for the present study, as large-scale beach nourishments are only a viable option along relatively shallow, sandy shelf coasts. The cross-shore coastal profile applied in this study, which was based on the average profile of the Delfland coast, is considered to be a typical setting for these nourishments. If the cross-shore profile is twice as steep, the nourished volume of sand (which is considered to be the governing design parameter) is confined to a smaller cross-shore extent, which limits the influence of a steeper profile on the characteristic water depth. Nevertheless, it should be noted that in case of a steeper profile, Re_z increases to $\mathcal{O}(10)$ and eddy instability and vortex shedding occur at somewhat lower K_C values already, which was also found from additional model simulations for these conditions (not presented here). If the tidal flow can be considered as semi-stationary (at high K_C), the degree of eddy instability and vortex shedding is expected to vary with Re_z as found by Wolanski et al. (1984) and Tomczak (1988).

Flow forcing due to Earth's rotation was not included in the model simulations. If the nourishment dimensions are very large, the Coriolis term has a small but noticeable influence on the flow field. An additional model simulation at $K_C = 8$ and $\alpha = 0.55$ with a Coriolis parameter representing conditions at 50° North causes up

to 8% deviations in eddy characteristics compared to the values presented in Figure 3.11. If cross-shore and vertical currents are concerned, the influence of Coriolis is expected to be more important.

The field data obtained around the Sand Motor in September 2014 can now be assessed in the light of the framework in Figure 3.13. During the flood phase at the Sand Motor, K_C is approximately 14. The September 2014 shoreline geometry of the mega-nourishment can be approximated by a cosine function with $\alpha \sim 0.3$. According to the framework, this is a transitional case between regions 1 and 3, which matches the observations from the ship-mounted ADCP (Figure 3.3). A slightly elliptical eddy develops along the northern edge of the Sand Motor, quite close to the nourishment tip. At the pressure switch (around 19h00 on 27 September 2014, Figure 3.4), the values of ℓ_{e0} and τ_e can be visually estimated from the ship-mounted ADCP data ($\ell_{e0} \sim 1.25$ and $\tau_e \sim 0.36$). The estimated eddy size and longevity match the values predicted from Figure 3.11 ($\ell_{e0} = 1.2$, middle panel and $\tau_e = 0.4$, right panel). Altogether, the framework presented in this section can be used to predict or explain the tidal flow field around coastline perturbations in shallow waters. As beach nourishments tend to diffuse along the coast over time, the change of the tidal flow field with morphological evolution can be predicted.

It is expected that the presence of tidal flow separation and eddy generation significantly increases particle dispersion around protruding beach nourishments (Signell and Geyer, 1990). Alongshore directed tidal particle trajectories are deformed when particles enter large-scale eddies. On short timescales (i.e. within one tidal half-cycle) this adds an important cross-shore component to the particle trajectory. On longer timescales, it leads to non-closed tidal excursion loops and therefore to persistent dispersion of particles carried with the tidal flow. This process has implications for several aspects, ranging from morphology and ecology to water quality and recreational safety. Notably, data presented by Huisman et al. (2016) show a strong correlation between the presence of fine sediment in the bed and the locations of tidal eddies at the Sand Motor. Quantification of dispersion by protruding beach nourishments and its implications are an important topic for future work.

3.7. CONCLUSIONS

In this study, the behavior of the tidal flow field around protruding beach nourishments was examined. Based on a diverse field dataset, obtained around the Sand Motor mega-nourishment at the Dutch coast, the separation of tidal flow in a real-world situation was analyzed. Subsequently, a validated numerical model was employed to determine the influence of changing perturbation dimensions on the character of the tidal flow field.

Results show that large-scale tidal eddies develop along the northern edge of the Sand Motor every flood period of the tide. Eddy development is found to be forced by a local adverse pressure gradient during the early tidal flow phase, and by a large-scale adverse tidal pressure gradient during the late flow phase. The intensity of the eddy modulates with the spring-neap cycle, with stronger eddies occurring during spring tide, when the peak tidal flow velocity is larger.

A validated numerical model shows the temporal development of predicted eddy size, strength and lifetime, which were quantified by extracting eddy size and intensity from cross-shore flow velocity transects along the downstream side of the perturbation. These parameters enabled characterization of the tidal flow field around nourishments of varying relative nourishment size and shape. The dimensionless Keulegan-Carpenter number K_C quantified the size of the perturbation relative to the tidal excursion length, while the aspect ratio α quantified the perturbation shape. Numerical results show that tidal flow separation does not take place for relatively smooth or very large perturbations, as under these conditions the nourishment is not pronounced enough (low α) or too large compared to the tidal excursion (low K_C). For sufficiently small and pronounced perturbations (high K_C and α), flow separation occurs downstream of the nourishment tip, with generated eddies varying in strength, size, shape and position based on the values of K_C and α. Eddies grow larger compared to the nourishment size if K_C and α increase, while the eddy intensity increases with increasing cross-shore nourishment size. The diameter of the eddies can be more than twice as large as the cross-shore nourishment dimension. For relatively small nourishments, the tidal flow becomes semi-stationary and the generated eddies are shed off the perturbation.

The field observations of eddy size and intensity obtained around the Sand Motor match the predictions made using the framework introduced in this study. These results imply that a man-made coastline perturbation can modify large-scale tidal current patterns, and generate tidal eddies at scales larger than the perturbation itself.

Acknowledgements

4

SENSITIVITY OF RIP CURRENT FORECASTS TO ERRORS IN REMOTELY-SENSED BATHYMETRY

Operational nearshore current forecasts based on numerical model simulations are gaining popularity as a measure to increase the safety of swimmers. Applying remotely-sensed bathymetry in these model simulations is often proposed in order to cope with rapidly changing nearshore bathymetry. Errors in the remotely-sensed bathymetry may negatively affect performance of the hydrodynamic model. Hence, this study aims to determine the sensitivity of modelled nearshore currents (with a strong focus on rip currents) to errors in remotely-sensed bathymetries.

The errors in the remotely-sensed bathymetries (depth inversion algorithm applied to video stream) were quantified with a length scale-aware validation technique, providing useful insights in the contribution of pattern and amplitude errors to the total error throughout the analysis domain and over a range of bathymetric length scales. Subsequently, simulations with a nearshore hydrodynamic model were performed, using both in-situ and remotely-sensed bathymetries as an input. Linking the performance statistics of predicted rip currents on the remotely-sensed bathymetry back to the quantified errors in the remotely-sensed bathymetry finally revealed the relation between errors in flow and bathymetry.

Of all rip currents generated on an in-situ bathymetry, 55% were reproduced on the remotely-sensed bathymetry, showing that models predicting nearshore currents on remotely-sensed bathymetry have predictive value. Positive rip current predictions were promoted by accurate reproduction of the pattern and amplitude of nearshore bars at length scales between 200 and 400 m. In contrast to the length-scale aware validation technique applied here, domain-wide bulk error metrics lack important information about spatial variations in the quality of remotely-sensed bathymetry.

4.1. INTRODUCTION

Operational prediction of nearshore currents by numerical models is an important method for mitigation of risks related to swimmer safety (Alvarez-Ellacuria et al., 2010; Voulgaris et al., 2011; Austin et al., 2012; Kim et al., 2013; Sembiring et al., 2015). The nearshore currents predicted by these models are strongly dependent on bathymetric variability, which is most clearly illustrated by field observations of rip cell circulations related to complex sand bar patterns (MacMahan et al., 2005; Austin et al., 2010; Winter et al., 2014). In turn, these sand bar patterns are affected by nearshore hydrodynamics, as waves and currents reshape the bed continuously. Consequently, sand bar patterns that cause rip cell circulations may change drastically on timescales of days to weeks (e.g. Holman et al., 2006; Price and Ruessink, 2011). In order to reliably predict nearshore hydrodynamics for swimmer safety purposes, operational numerical models should be provided with updated bed levels frequently. This is virtually impossible to achieve with labour-intensive in-situ bed level measurement techniques (e.g. a single-beam echo sounder mounted on a personal watercraft; MacMahan, 2001). Alternatively, nearshore bathymetry can be estimated operationally using remote sensing techniques. The technical feasibility of coupling remotely-sensed bathymetry to nearshore hydrodynamic predictions was presented by Radermacher et al. (2014) and Sembiring et al. (2015), successfully demonstrating the potential of this combination. While they report the accuracy of the resulting simulated flow fields at their respective field sites, they do not adress the coupling between errors in the remotely-sensed bathymetry and the simulated flow fields. The aim of the present research is to determine the sensitivity of simulated rip current occurrence and location to errors in remotely-sensed bathymetries. Only geometrically defined rips related to nearshore sandbar patterns are considered. Other types of rip currents (a.o. headland rips, transient rips) are excluded here.

Over the last decades, a wide range of depth inversion algorithms has been developed, which aim to fit a local water depth to remotely-sensed wave parameters based on physical relations. For instance, these algorithms may employ wave fields observed with video or radar to estimate water depth through the linear dispersion relation (a.o. Bell, 1999; Holman et al., 2013) or model-data assimilation of video-observed wave breaking patterns (a.o. Aarninkhof et al., 2005; Van Dongeren et al., 2008). Although these remote sensing techniques are capable of providing nearshore bathymetry estimates at short time intervals, it is unclear how errors in the resulting bathymetry estimates translate to errors in the resulting flow predictions and whether the bathymetric estimates are sufficiently accurate to be applied in the prediction of nearshore hydrodynamics.

In order to be a significant contribution to recreational safety, an operational hydrodynamic model should adequately predict spatio-temporally varying nearshore current patterns. Primarily, this concerns correct prediction of rip current occurrence and location. Remotely-sensed bathymetries applied in these model simulations should be of sufficient quality to support this aim. Traditionally, the accuracy of remotely-sensed bathymetry with respect to in-situ techniques is assessed from bulk error metrics, such as the root-mean-squared error (RMSE), bias and corre-

lation, or from difference maps (Plant et al., 2007; Senet et al., 2008; Van Dongeren et al., 2008; Holman et al., 2013; Rutten et al., 2017a). Previous attempts to assess the quality of hydrodynamic predictions on remotely-sensed bathymetry by Raderma-cher et al. (2014) and Sembiring et al. (2015) demonstrated the difficulty of linking bathymetric errors to hydrodynamic errors purely based on bulk point-wise error metrics. Nearshore currents do not just depend on the local water depth, but are influenced by bathymetric features that span a range of length scales (Wilson et al., 2013; Plant et al., 2009). Therefore, it is expected that the accuracy of nearshore cur-rent predictions on the remotely-sensed bathymetry is strongly linked to the ability of a depth inversion algorithm to resolve spatial bathymetric patterns.

Here, the performance of a video-based depth inversion algorithm is studied with a pattern-aware validation technique applied to the resulting bed topography maps (Section 4.3.1). Subsequently, wave-driven nearshore currents are simulated with a validated numerical model on the remotely-sensed bathymetries and on tra-ditionally obtained vessel-based bathymetries. A comparison of simulated flow pat-terns on both types of bathymetries, focused on rip currents, yields performance statistics of nearshore current predictions on remotely-sensed bathymetries (Sec-tion 4.3.2). Finally, these current prediction performance statistics are linked to the bathymetric error statistics from Section 4.3.1, which highlight the relation between bathymetric variability and nearshore flows (Section 4.3.3). First, the methodology outlined above will be elaborated upon in Section 4.2, along with a description of the study site.

4.2. METHODOLOGY

4.2.1. FIELD SITE AND INSTRUMENTAL SETUP

In order to assess the accuracy of nearshore currents simulated on a video-derived bathymetry, data were obtained at the Sand Motor, a mega-scale beach nourish-ment in the Netherlands (Stive et al., 2013). The large scientific attention for this coastal engineering pilot project has yielded extensive field datasets (De Zeeuw et al., 2017), which have been employed here for comparison to video-derived bathymetry estimates and hydrodynamic model simulations. The Sand Motor was constructed in 2011 as a 17.5 Mm^3 sandy peninsula and is intended to nourish the adjacent coastline throughout the coming decades by natural alongshore sediment trans-port. It is situated within the Delfland coastal cell, a 17 km stretch of coastline be-tween the harbor breakwaters of Rotterdam and The Hague. At approximately two-monthly intervals, the bathymetry was surveyed (see Figure 4.1, panel A) with high accuracy using a single-beam echo sounder and RTK-DGPS mounted on a personal watercraft for the sub-aqueous part of the measurement domain and on an all-terrain vehicle for the sub-aerial part (details provided in De Schipper et al., 2016). The original bed elevation data were subsampled to a 25 x 25 m resolution (Plant et al., 2002) and subsequently linearly interpolated to a 20 m x 10 m grid (alongshore x cross-shore resolution). As a result, only bathymetric features at scales larger than 25 m are considered in this study. This matches conditions at the Dutch North Sea coast, where subtidal sandbar variability typically occurs at scales larger than 50 m
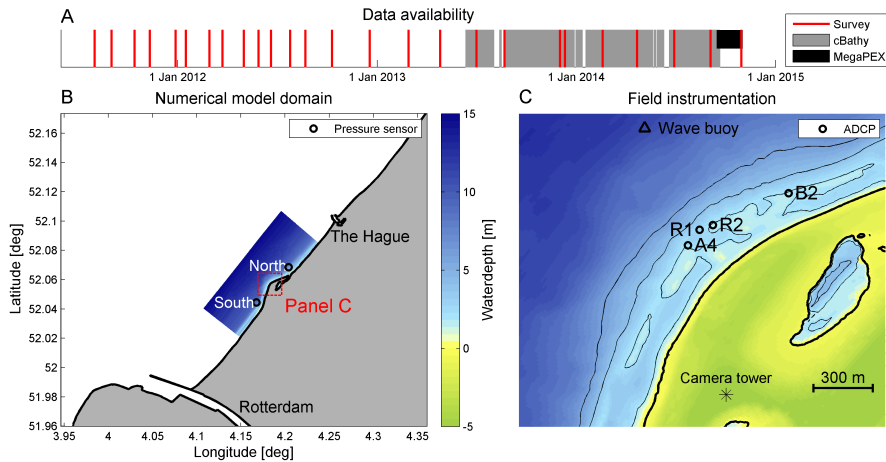
Figure 4.1: Overview of available field data and extent of numerical model domain: timeline of available in-situ bathymetry surveys, periods with cBathy coverage and MegaPEX experiment (panel A), position of the Sand Motor and the model domain (area covered by bathymetric data) along the Delfland coast with colours representing water depth and grey shading representing the dry land (panel B) and nearshore field setup with ADCP stations, depth contours and Argus camera tower (panel C).

(e.g. De Schipper et al., 2013; Winter et al., 2014; Sembiring et al., 2014). All surveys used in this study are presented in Figure 4.2.

An extensive set of field observations was collected in fall 2014 during the Mega Perturbation Experiment (abbreviated to MegaPEX), comprising a.o. nearshore pressure and velocity measurements with four acoustic doppler current profilers (AD-CPs) over a four-week period (Figure 4.1, panel C). This type of instrument has been successfully applied before for observations of nearshore current dynamics, a.o. by Brown et al. (2015). The ADCPs were deployed on the nearshore bars and at the seaward end of an oblique rip channel. They sampled the vertical current profile in bins of 0.5 m as well as the pressure. Depth-averaged flow velocities were calculated by averaging over all sub-aqueous bins (i.e. bins that are submerged more than 99% of the time within a temporal window of 10 minutes). If no sub-aqueous bins were found at a particular point in time, no depth averaged flow velocity was computed for that time. In order to remove short-term fluctuations from the timeseries, the velocity timeseries were low-pass filtered with a cut-off period of 10 minutes. Further details of the ADCPs are provided in Table 4.1, where h denotes the average water depth, z_{bbc} is the vertical level of the bottom bin center and t_{av} is the internal averaging duration of the instrument. Additionally, pressure sensors were deployed at 6 m water depth just north and south of the Sand Motor.

4.2.2. REMOTELY-SENSED BATHYMETRY
A tower is located at the most elevated point of the Sand Motor, with 8 cameras covering an approximately 230 degree horizontal view angle (part of the Argus network; Holman and Stanley, 2007). The depth inversion algorithm applied to the 2 Hz video
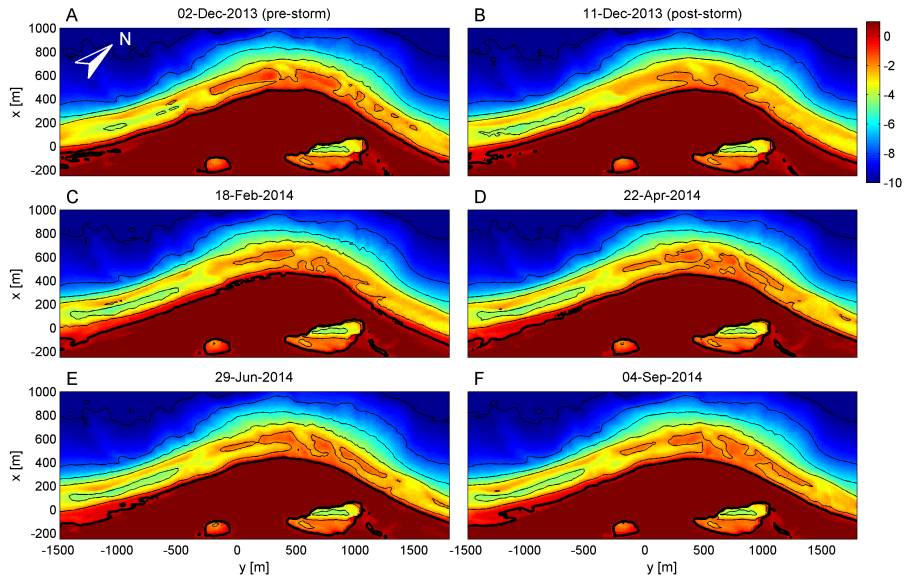
Figure 4.2: Overview of the six in-situ surveyed bathymetries that are used in this study. The first two surveys were captured just before and after a severe storm (peak $H_s \sim 5$ m). The locations of bars and rip channels remain fairly stable, while the exact shape and orientation of bathymetric features varies throughout the analysis period. All bed levels in this study are presented relative to the Dutch vertical datum NAP (approximate mean sea level).

Table 4.1: ADCP properties.

Station	Type	h [m]	z_{bbc} [m]	t_{av} [s]
A4	Nortek Aquadopp profiler 1 MHz	2.16	-1.18	1
R1	Nortek Aquadopp profiler 2 MHz	2.59	-1.27	15
R2	Nortek Aquadopp profiler 1 MHz	1.80	-1.15	1
B2	Nortek Aquadopp profiler 2 MHz	1.79	-1.26	20

stream is named *cBathy* (detailed description can be found in Holman et al., 2013). cBathy applies cross-spectral analysis to the video intensity timeseries in order to determine dominant pairs of frequency and wave number within a sliding spatial analysis window (Plant et al., 2008) and subsequently inverts the linear dispersion relation to make an estimate of the water depth. Timeseries of water depth estimates on a 20 x 10 m analysis grid (alongshore x cross-shore spacing) are then fed into a Kalman filter (Kalman, 1960) in order to reduce noise and make the depth estimates more robust. Applications of the cBathy algorithm to Argus imagery at various field sites and under a range of environmental conditions have demonstrated its capability to resolve nearshore bathymetry with a bulk root-mean-squared error of approximately 50 cm (Holman et al., 2013; Wengrove et al., 2013; Radermacher et al., 2014; Sembiring et al., 2015; Bergsma et al., 2016; Rutten et al., 2017a). Depth estimates were obtained every four hours during daytime since installation of the camera tower in 2013, with the exception of several periods of down-time (Figure 4.1, panel A). For this study, cBathy's Kalman filter was initiated on 13 June 2013 and fed with 4-hourly bathymetry estimates. In addition to the algorithm presented by Holman et al. (2013), an outlier removal routine was added here to prevent several site-specific error sources (mainly ships sailing through the camera view) from fouling the remotely-sensed bathymetry. Depth estimates falling outside a 1.5 m envelope around the nearest groundtruth survey or the previous filtered bathymetry estimate were rejected. The *process error* calibration parameter was set to a value of 10^{-4} day^{-1}. This was found to yield the most accurate bathymetry estimates when compared to in-situ surveyed bed levels. It was verified that this parameter choice can cope with natural site morphodynamics by comparing cBathy results to a pre and post-storm groundtruth survey.

The present study emphasises the importance of local bathymetric patterns when studying nearshore currents. Advanced, pattern-aware comparison and verification methods for spatial parameter fields have been proposed by many authors, mostly within the field of meteorology. An extensive overview is presented by Gilleland et al. (2009). Not all methods perform equally well if the spatial parameter field consists of nearshore bed levels along a curved coastline. Scale separation methods, which assess bandpass-filtered parameter fields to perform a scale-selective comparison (e.g. Briggs and Levine, 1997), have the theoretical advantage of quantifying length scales of bathymetric patterns, but fail to separate variability due to nearshore bar patterns from variability related to the cross-shore beach profile. This is considered impractical here, as variability due to the cross-shore beach profile is irrelevant for this study of nearshore circulation patterns. The same holds for feature-based methods, which detect and compare physically relevant features by setting parameter value thresholds (e.g. Ebert and McBride, 2000).

Here, a neighborhood method is employed, which is comparable to the method presented by Bosboom and Reniers (2014). The quality of the remotely-sensed bathymetry with respect to the in-situ bathymetry is determined by computing several error metrics within a circular sliding window of diameter *L*. This approach acknowledges both the spatially coherent structure of the bathymetry (by calculating bulk metrics over all points within a distance *L* of each other) and the spatial

variability in bathymetric features encountered along a beach (by applying a sliding window over the 20 x 10 m cBathy grid). Before the error metrics are computed, the average beach slope is removed by fitting a least squares plane to the windowed in-situ bathymetry and subtracting that from both bathymetries. The error metrics were then computed as follows: let z_i be the in-situ bathymetry and z_r the remotely-sensed bathymetry within the same spatial window of n data points and z_i' and z_r' their respective counterparts after subtracting the average slope. The error metrics computed in the sliding window are (Figure 4.3 and Equations 4.1a through 4.1d): (1) the correlation ρ, (2) the bias b, (3) the ratio of standard deviations $\hat{\sigma}$ and (4) the root-mean-squared error ϵ.

$$\rho = \frac{\frac{1}{n}\sum_{k=1}^{n}(z_{i,k}' - \bar{z}_i')(z_{r,k}' - \bar{z}_r')}{\sigma_i \sigma_r} \tag{4.1a}$$

$$b = \bar{z}_r - \bar{z}_i \tag{4.1b}$$

$$\hat{\sigma} = \frac{\sigma_r}{\sigma_i} \tag{4.1c}$$

$$\epsilon = \sqrt{\frac{1}{n}\sum_{k=1}^{n}(z_{r,k} - z_{i,k})^2} \tag{4.1d}$$

Here, n is the number of data points inside the circular sliding window, subscripts i and r indicate in-situ or remotely-sensed quantities respectively, the overbar denotes window-averaged quantities and σ denotes the standard deviation of bed levels z' within the window.

The example shown in Figure 4.3 treats a spatial window with a relatively good performance of the depth inversion algorithm. The patterns are matching fairly well ($\rho = 0.93$), while the remotely-sensed bathymetry slightly underestimates the amplitude of bathymetric variability ($\hat{\sigma} = 0.96$). The bias is close to 0 and the RMSE is 0.27 cm.

4.2.3. NUMERICAL MODEL

The present study relates bed level deviations in the remotely-sensed bathymetry to their impact on the nearshore flow field. To this end, nearshore currents were simulated on remotely-sensed as well as in-situ surveyed bathymetries with the Delft3D modeling suite, which has been used sucessfully for nearshore current simulation in previous studies (Elias et al., 2000; Reniers et al., 2007, 2009, 2010). Setup and validation of the model are discussed in more detail in Appendix B. The root-mean-squared error of modelled versus observed flow velocities is in the order of 10 cm/s. As the model is validated by comparing modelled flow velocities and water levels to quantities measured in the field, the model described in the appendix is intended to closely match conditions occurring at the Delfland coast. For the simulations discussed in Section 4.3.2, a more synthetic version of this model is applied by removing the tidal water level modulations and associated currents, as this study aims to isolate the relation between nearshore bathymetry and wave-driven currents. The
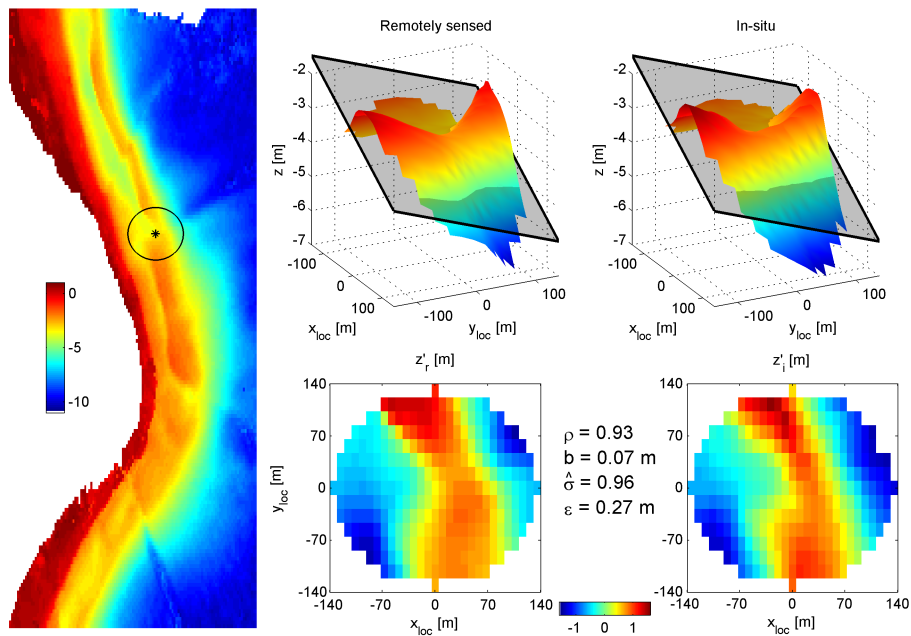
Figure 4.3: Demonstration of the pattern-aware bathymetry validation method. The location and size of the analysis window are indicated in the leftmost panel, along with the remotely-sensed bathymetry. The top panels show the remotely-sensed and in-situ measured bathymetries within the analysis window, including the least-squares fitted plane of the in-situ measured bathymetry. The bottom panels show the residual bathymetries z'_r and z'_i. Values of the four error metrics are stated between the bottom panels.

Figure 4.4: Example of rip current detection on computed flow field. Shading represents off-shore velocity in m/s. Four detected rip current patches have been marked in blue. The thick black line marks the 0 m bed level contour.

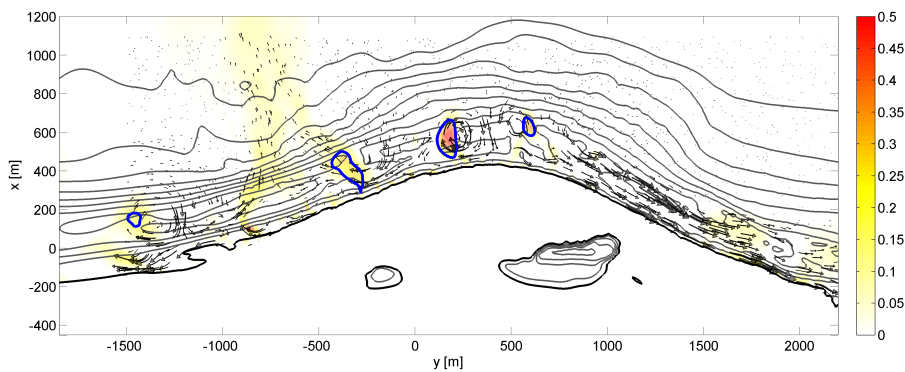wave conditions at the offshore boundary were held constant at $H_{m0} = 1.5$ m, $T_p = 6$ s and a directional spreading of 25° throughout all simulations, while the off-shore wave angle varied between simulations. The significant wave height of 1.5 m was chosen to make sure that sufficient wave energy dissipates on the subtidal bar, accounting for the generation of rip currents. The chosen wave height represents an upper limit of the wave energy that can be expected on a bright summer day at the Dutch coastline.

As studying the response of nearshore currents to nearshore bathymetry in a swimmer safety context is naturally focused on the generation of rip currents, simulated nearshore flow fields were subjected to a rip current detection algorithm. Concentrated patches of strong off-shore velocities (> 0.2 m/s) were identified as rip currents (see Figure 4.4 for an example). Rip current detection was performed on fields of the Generalised Lagrangian Mean flow velocity (Groeneweg and Klopman, 1998), which is resolved directly from the shallow water equations in Delft3D (Reniers et al., 2009). Following automated detection using the velocity threshold value stated above, manual quality control was performed to alleviate the discrete behavior of the rip current detection method around the velocity threshold value. The similarity of flow patterns in both simulations of a simulation pair was checked around every detected rip current. In some cases, a particular rip current was only detected in one of the two simulations, although the two simulations had visually similar flow patterns and similar off-shore velocity magnitudes. This is a result of the offshore directed flow velocity being just above and below the threshold value in the two simulations respectively. The resulting discrete behavior is considered undesirable. Therefore, automatic rip current detection in these cases was overruled by classifying both flow patterns as a rip current. Attempts to automate this correction through quantification of flow field similarity were not successful.

Subsequently, the rip current detection algorithm was applied to model simulations on six pairs of remotely-sensed and in-situ surveyed bathymetries. Each bathymetry was subjected to waves under five different off-shore angles of incidence, ranging from -30 to +30 degrees with respect to shore-normal at 15 degree intervals, constituting a total of 30 pairs of model simulations. Detected rip currents were compared between the two simulations of every pair, resulting in statistics regarding positive, false negative and false positive rip current predictions on the remotely-sensed bathymetry. For a pair of rip currents to be classified as a positive prediction, the centroids of the detected patches had to be closer than 0.75 times the sum of the alongshore patch dimensions. This criterion was found to match best with visual inspections of the similarity of simulated flow fields. The sensitivity of the results to this criterion is very small, as only 3% of all detected rip current pairs in this study are situated around the threshold value (i.e., only 3% of rip current pairs have a relative separation distance of the rip current patches between 0.5 and 1.25). A rip current predicted on the in-situ bathymetry, but not on the remotely-sensed bathymetry was counted as a false negative, while the opposite case was counted as a false positive.
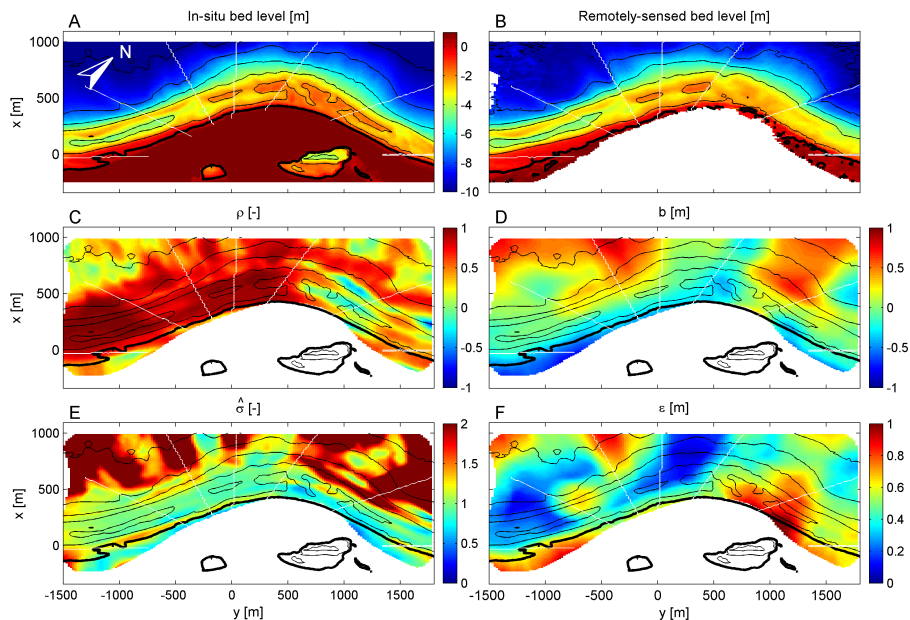
Figure 4.5: Bathymetric validation at 4 September 2014 with a window size *L* of 320 m. Panels A and B show the in-situ and remotely-sensed bathymetries, while panels C through F show the four error metrics defined in Equation 4.1. Bed level contours at 2m intervals were added to aid interpretation of the error metrics. Camera view boundaries are indicated as white lines.

4.3. RESULTS

4.3.1. PATTERN-AWARE VALIDATION OF REMOTELY-SENSED BATHYMETRY

Six pairs of in-situ surveyed and remotely-sensed bathymetries were subjected to the pattern-aware validation technique introduced in section 4.2.2. Results are treated here for the 4 September 2014 bathymetry pair as an example (see Figure 4.5).

At the scale of the entire Sand Motor, the error metrics reveal a strong divide between the southern and northern (left and right respectively in the figure) half of the nourishment on the one hand and between the nearshore and the off-shore part of the domain on the other hand. These large-scale trends are complemented with local, small-scale variations. The correlation ρ (panel C) is close to 1 along the southern edge of the Sand Motor, while it tends to 0 or even becomes negative along the northern edge and in the off-shore corners of the domain. This mismatch of bathymetric patterns on the northern side can be confirmed by comparing panels A and B of Figure 4.5. In the off-shore corners, the bed is almost featureless, which allows residual noise in the remotely-sensed bathymetry to dominate the correlation.

The spatial variation in the bias b (panel D) largely confirms that the cBathy algorithm tends to underestimate the water depth at deeper waters, while it overestimates the water depth near the shoreline (also found by Holman et al., 2013;
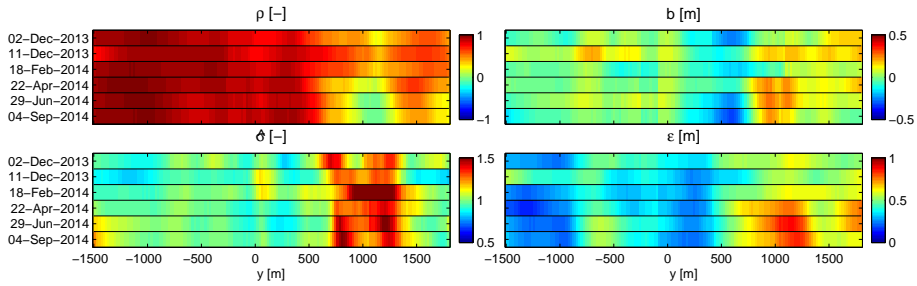
Figure 4.6: Nearshore-averaged error metrics for all six bathymetry pairs as a function of alongshore distance.

Bergsma et al., 2016; Rutten et al., 2017a), although the windowed calculation reveals important local differences. Especially the sharply delineated patches of high bias in the off-shore part show that the bias at deep water differs between individual camera views. This suggests that the deep water bias can partly be explained by inadequate or outdated geo-referencing of several cameras at the Sand Motor Argus station, a problem commonly encountered at operational camera stations.

Standard deviation ratio $\hat{\sigma}$ (panel E) tends to be large in the off-shore part of the domain, while it is close to 1 in the nearshore. In the off-shore areas, as was mentioned before, residual noise in the remotely-sensed bathymetry leads to a relatively high standard deviation compared to the featureless in-situ bathymetry. The fact that $\hat{\sigma}$ is close to 1 in the nearshore areas indicates that cBathy is generally well-capable of reproducing bathymetric variability there.

Finally, the root-mean squared error (RMSE) ϵ (panel F) contains strong spatial variations. This goes to show that the bulk, domain-wide RMSE, which is often reported in depth inversion validation studies (0.58 m in this case), is not a very representative indicator of the performance of a depth inversion algorithm for the entire field site. Performance may differ strongly between particular zones in the field of view of a camera station. The windowed calculation of ϵ already gives more insight and can be regarded as an aggregated error metric that reflects the combined effect of the three other parameters (Murphy and Epstein, 1989).

A synoptic overview of these four error metrics throughout all six bathymetry pairs can be constructed by cross-shore averaging of the error metrics over the nearshore part of the profile (between the -1 m and -5 m bed level contours, see Figure 4.6). Pattern-aware validation of all bathymetry pairs yields similar results regarding the large-scale contradictions in performance between the southern and northern side. At smaller scales, temporal evolution of the bathymetric quality can be observed. Especially the deterioration of ρ, b and ϵ around $y = 1000$ m from the April 2014 survey onwards is remarkable. This is related to the development from a rather featureless or cluttered bathymetry before that date to a bathymetry with well-defined bar patterns in that area. As the remotely-sensed bathymetry fails to reproduce clear bar patterns along the northern edge of the nourishment, its skill to reproduce the in-situ bathymetric patterns there (reflected by ρ) decreases sharply

Table 4.2: Rip current prediction performance over 30 simulation pairs.

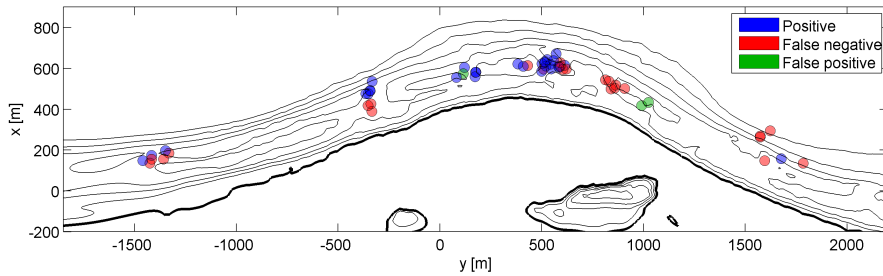| Prediction	Occurrences
Positive	29
False negative	24
False positive	3

Figure 4.7: Overview of all detected rip currents throughout all pairs of simulations. Depth contours of the 22 April 2014 bathymetry are shown as a reference. Markers are slightly transparent to show overlapping rip currents.

in April 2014.

4.3.2. NEARSHORE CURRENT SIMULATIONS

Thirty nearshore hydrodynamic model pairs with varying bathymetries and off-shore wave angles were simulated. The resulting flow fields were subjected to the rip current detection algorithm (Section 4.2.3). Rip currents detected in pairs of model simulations were classified as positives, false negatives and false positives. The statistics over all model simulations are presented in Table 4.2. Out of 53 rip currents predicted on the in-situ bathymetry, 55% were positively predicted on the remotely-sensed bathymetry, while 45% of the rip currents generated on an in-situ bathymetry were missed in simulations with remotely-sensed bathymetry. Out of 32 rip currents predicted on the remotely-sensed bathymetry, 9% were found to be false positive predictions that did not occur on the associated in-situ bathymetry.

It is remarkable that the number of false positives is far lower than the number of false negatives. This difference may be related to errors in the remotely-sensed bathymetry and is addressed in more detail in section 4.4. The map with the locations of all 56 detected rip currents throughout all simulation pairs (Figure 4.7) indicates that rip current formation is constrained to several rip-bar configurations in the underlying bathymetries. Most false negatives are situated along the northern edge of the nourishment, while most positives can be found around the most seaward point of the Sand Motor.

4.3.3. Relating bathymetric errors to flow errors

In the previous section, performance statistics of simulated rip currents on remotely-sensed bathymetry were presented. The source of the input bathymetry (in-situ or cBathy) was varied between the two simulations in a simulation pair. Therefore, it is expected that observed differences between simulated flow fields and detected rip currents can (partly) be explained based on the pattern-aware bathymetry error metrics that were presented in section 4.3.1. For every detected rip current, the associated bathymetry errors at the center point of the rip current patch were extracted (in case of a positive rip current prediction, the mean location of the two patch centroids from both simulations was used). The bathymetric analysis length scale L was varied between 80 m and 400 m in steps of 40 m. The resulting parameters (ρ, b, $\hat{\sigma}$ and ϵ) were transformed in order to make their relation to bathymetric performance monotonous, i.e. a low parameter value means good performance and a high parameter value means bad performance, or vice versa. Parameters ρ and ϵ naturally possess this property. The absolute value was taken of b, while $\hat{\sigma}$ was transformed to $|\hat{\sigma} - 1|$. Subsequently, parameters were normalised to have zero mean and a standard deviation of 1. Normalised equivalents of the bathymetric error metrics are indicated with subscript n. Good performance is indicated by high ρ_n, low b_n, low $\hat{\sigma}_n$ and low ϵ_n.

Normalised bathymetric error metrics can now be compared for positive and false negative rip current predictions (Figure 4.8). False positives are omitted here due to the low number of observations (3). Bootstrapped mean parameter values and associated 95% confidence intervals per class (positive or false negative) were obtained from 10^4 realisations. The relative distance Δ between the two class averages was computed through dividing the absolute distance by half the sum of the confidence intervals of the two classes. The case $0 < \Delta < 1$ corresponds with overlapping confidence intervals of the two classes and therefore insignificant discriminative power of the associated bathymetric error metric. The case $\Delta > 1$ corresponds with non-overlapping confidence intervals and significant discriminative power.

The value of Δ has been computed for every error metric over a range of bathymetric length scales L (Figure 4.9). The bathymetric correlation ρ significantly differentiates between positives and false negatives for L between 200 and 400 m, the maximum value occuring at $L = 320$ m. Within this range of length scales, positive rip current predicitons are associated with significantly better correlated remotely-sensed bathymetry than false negatives. The ratio of standard deviations $\hat{\sigma}$ has significant discriminative power between $L = 240$ m and $L = 360$ m, the maximum value again occurring at $L = 320$ m. For positive rip current predictions, $\hat{\sigma}$ is significantly closer to unity (i.e. equal standard deviations and therefore equal levels of bathymetric variability) than for false negatives. The bathymetric root-mean-squared error ϵ significantly differentiates between classes for $320 < L < 400$ m, but has less discriminative strength than ρ and $\hat{\sigma}$. The bias b of the remotely-sensed bathymetry does not have a significant influence on rip current prediction performance, as Δ_b remains below unity for all tested length scales. The sharp decline of Δ for $\hat{\sigma}$ above $L = 320$ m is remarkable, since the discriminative power of ρ and ϵ still remains significant. As L increases towards 400 m, the positive rip current predic-
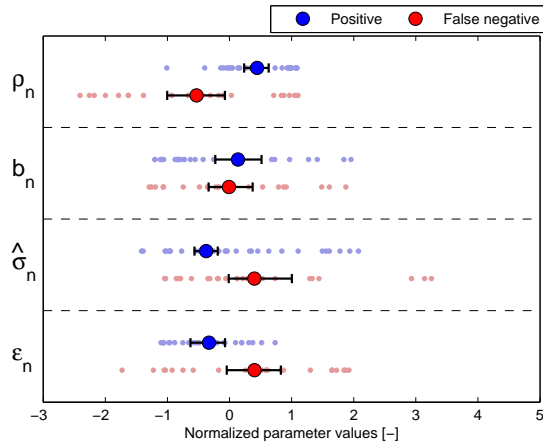
Figure 4.8: Normalised bathymetric error metrics for positive and false negative rip current predictions with $L = 320$ m. Bootstrapped mean values and 95% confidence intervals are presented for every parameter. Non-overlapping confidence intervals indicate discriminative power of the associated error metric, which holds for ρ_n, $\hat{\sigma}_n$ and ϵ_n.

Figure 4.9: Relative distance Δ as a function of analysis length scale L for all bathymetric error metrics, indicating their discriminative strength.

tions around the most seaward point of the nourishment start being associated with low bathymetric skill along the northern edge. Analogously, negative predictions along the northern edge start being associated with high bathymetric skill around the most seaward point. This ef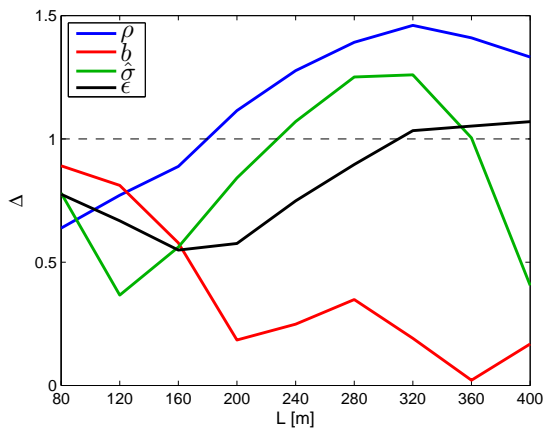fect, which clutters the relations between flow performance and bathymetric skill, appears to start at smaller L for $\hat{\sigma}$ than for ρ and ϵ due to differences in the spatio-temporal evolution of these parameters.

Additionally, three flow-related parameters are examined for their discriminative strength. These parameters, being the maximum cross-shore flow velocity found in a rip current patch U, the off-shore wave angle with respect to the local shoreline orientation α and the mean alongshore flow velocity in a rip current patch V, are derived directly from the hydrodynamic simulations and therefore do not depend on L. Neither of the three selected parameters significantly differentiates between positives and false negatives, as Δ remains below unity in each case.

4.4. Discussion

The results presented in section 4.3 show that an operational rip current prediction system with updated remotely-sensed bathymetry performs best if the remotely-sensed bathymetry correlates well with the groundtruth bathymetry and if the amount of variability in both bathymetries is comparable. These relations are significant at bathymetric length scales approximately between 200 and 400 m. It implies that adequate reproduction of the pattern (related to ρ) and amplitude (related to $\hat{\sigma}$) of large nearshore sand bars by the depth inversion algorithm is most important for skilful rip current prediction. The relevant range of length scales derived here is of the same order as the scales reported by Plant et al. (2007) and Wilson et al. (2013) as the most important scales regarding cross-shore current generation. Relating length scale dependence of nearshore currents to a shallow water Reynolds number, as presented by Wilson et al. (2013), is only viable in a weakly alongshore varying regime. The presence of pronounced bathymetric variability and associated rip currents in this study hampers that approach.

False positive rip current predictions were only found in three cases, whereas false negatives occur more regularly in the dataset. Because three data points are not enough to infer statistically significant relations, determining the factors promoting false positive rip current predictions based on the model simulations is difficult. However, this result may be expected based on the facts that (1) cBathy tends to overestimate nearshore water depth (e.g. Rutten et al., 2017a) and (2) cBathy typically smoothens real-world bar patterns but hardly ever exaggerates bar patterns or generates non-existent bars. A positive bias of water depth in the nearshore and removal of breaker bars will promote the probability of underestimating wave breaking on the sub-tidal bar and thereby reduces bathymetric rip current forcing, leading to false negatives rather than false positives.

The numerical model simulations in the framework of this study were performed with a constant off-shore significant wave height of 1.5 m and a constant water level equal to mean sea level. This combination of parameters was observed to induce differential wave breaking all along the sub-tidal bar (i.e. wave breaking at the bar crest, but no wave breaking in the rip channel), thereby promoting rip current gen-

eration in areas with sufficient alongshore bathymetric variability. This choice is justified by the fact that the added value of updated remotely-sensed bathymetry is primarily created by the ability to detect spatio-temporal variability in nearshore bar patterns. Whether or not rip currents are generated over a certain bathymetric pattern is mostly governed by spatial gradients in wave energy dissipation and therefore by the ratio of the wave height at the bar crest over the local water depth, H_b/h_b. As the bar crest height varies along the coastline, progressively decreasing the off-shore wave height or increasing the (tidal) surface elevation in the numerical model simulations would lead to less and less alongshore sections with wave breaking at the sub-tidal bar. Ignoring potential dependencies between bar crest height and alongshore bathymetric variability, there is no reason to believe that a lower wave height would alter the relative performance statistics presented in Table 4.2. However, regarding the relations between bathymetric quality and rip current prediction identified in Figure 4.9, it is expected that the importance of bathymetric bias would strongly increase if the off-shore wave height is lowered. The breaker parameter for a biased bathymetry is actually $H_b/(h_b + b)$, which becomes very sensitive to the exact value of b if the breaker parameter at the bar crest is in the critical range between wave breaking and no wave breaking.

Generally, operational nearshore current prediction with video-derived bathymetry is thought to be a valuable tool for beach safety management. The present study showed that the tool has predictive value (55% positive predictions at the Sand Motor), although the exact percentage of positive predictions cannot be directly translated to other field sites. Errors in the remotely-sensed bathymetry were found to vary strongly throughout the camera domain, possibly depending on camera graze angles, geo-referencing and wave incidence angles. The Sand Motor camera station has a rather complex geometry, with a strongly curved coastline and a large area of interest. Hence, rip current prediction performance is likely to be higher along a straight coastline. Nevertheless, in day-to-day beach safety management, numerically generated rip current predictions should always be regarded as one out of multiple information sources for lifeguards (their own experience and visual observations being other very important sources).

An important aspect of determining the merits of remotely-sensed bathymetry for rip current prediction is the trade-off between using outdated, but more accurate in-situ surveyed bathymetries or up-to-date but error-prone remotely-sensed bathymetries. The mobility of nearshore sand bar patterns plays a central role in this respect, as it determines the rate at which an outdated in-situ survey loses its power to predict the actual bathymetry. The trade-off between these two sources of bathymetry has not been addressed here, as it is outside of the scope of the present study. Recognising that an optimal prediction of up-to-date nearshore bathymetry would rely on assimilation of outdated in-situ data and up-to-date remotely-sensed data, insight in the relative accuracy of both data sources under increasing age of the in-situ data would help to determine the optimal assimilation scheme.

4.5. CONCLUSIONS

The present study has assessed the sensitivity of operational rip current forecasts to video-derived bathymetry estimates. It was found that rip currents predicted on remotely sensed bathymetry have predictive value. Of all rip currents generated on an in-situ bathymetry, 55% were reproduced on the remotely-sensed bathymetry. The system is prone to false negative predictions, meaning that 45% of rip currents generated on the groundtruth bathymetry are not reproduced on the remotely sensed bathymetry. In contrast, false positive predictions are rare, meaning that only 9% of rip currents predicted on the remotely sensed bathymetry do not occur on the in-situ bathymetry. This fact can be applied when using operational rip current forecasts in daily beach management, as rip currents predicted on remotely sensed bathymetry will have a very high probability of occurring in reality.

Errors in the remotely sensed bathymetry were found to exhibit strong spatial variability due to dependence of depth inversion performance on the water depth and on camera-specific error sources (quality of the camera geo-referencing, camera resolution in real-world coordinates and alongshore differences in coastline orientation and wave incidence). Generally, depth estimates in the offshore part of the camera domain are characterised by a negative bias and a relatively high noise level, while nearshore depth estimates have a positive bias but contain realistic bar patterns (in the absense of afore-mentioned camera-specific errors sources).

The performance of rip current prediction on remotely sensed bathymetry was found to depend on the ability of the depth inversion algorithm to reproduce patterns and amplitudes of nearshore bars. Positive rip current predictions were promoted significantly by accurate reproduction of the pattern and amplitude of nearshore bars at length scales between 200 and 400 m. The angle of wave incidence, cross-shore rip current intensity and strength of the alongshore flow velocity did not significantly influence rip current prediction performance.

The results presented here imply that spatio-temporal maps of the pattern and amplitude errors of remotely-sensed bathymetry can be used to predict the performance of nearshore circulations simulated on that bathymetry. In contrast, domain-wide bulk error metrics lack important information about spatial variations in the quality of remotely-sensed bathymetry.

5

SWIMMER SAFETY AROUND SAND NOURISHMENTS: A SYNTHESIS BASED ON THE SAND MOTOR

A generic framework for coastal swimmer safety is applied to the Sand Motor mega nourishment. Knowledge of hazardous hydrodynamic phenomena around mega nourishments, presented in the preceding chapters of this thesis, is combined with information on the spatio-temporal distribution of beach users at the Sand Motor. This analysis yields insight into the local swimmer safety risks, defined as the coincidence in space and time of hazardous hydrodynamics and beach users.

It is found that tidal currents in the channel that connects the Sand Motor lagoon to the North Sea form the highest swimmer safety risk, as these currents have a high coincidence in space and time with the presence of beach users. In contrast, the risk related to rip current generation over subtidal sandbars is found to be relatively low, due to the low probability of wave breaking over subtidal sandbars on crowded beach days in The Netherlands. The risk related to tidal flow separation at the Sand Motor is relatively low as well. Offshore directed currents may occur as a result of tidal flow separation around the most seaward point of the nourishment, where beach attendance is typically very low. The risk of rip current generation over subtidal sandbars is expected to be significantly larger at open ocean coastlines, which may receive energetic distant swell on a bright summer day with high beach attendance.

5.1. INTRODUCTION

The implementation of coastal engineering works, such as large-scale sand nourishments, potentially generates hazardous hydrodynamic phenomena. This was illustrated in the the previous chapters of this thesis, which highlighted several mechanisms that could induce hazardous flow patterns around sand nourishments. Safe recreation should be and often is a strict condition for the design and implementation of such engineering works. Furthermore, uncertainties regarding the impact of a coastal intervention or a lack of communication about this aspect might have a negative impact on public support for the project (Van den Hoek et al., 2014b). Being able to understand and predict the influence of coastal engineering works on swimmer safety is crucial, as many coastal interventions are executed at popular recreational beaches.

In the introduction of this thesis, a generic framework for the assessment of coastal swimmer safety was presented, which is comprised of three key components: (1) the timeline of drowning, (2) the notion of swimmer safety risk as the coincidence in space and time of hazardous hydrodynamics and beach users and (3) the notion of predictability of swimmer safety across different spatio-temporal scales. These components are briefly recapitulated here.

First of all, the safety of a particular beach visitor can be influenced at any stage along the timeline of drowning (Figure 1.1). Mitigation measures for recreational risks aim to break the sequence of events between visiting a beach (first stage of the timeline) and actual drowning (last stage) at any point along the timeline. Secondly, coastal swimmer safety inherently is a multi-disciplinary field of science, comprising physical, social and medical aspects. Physical aspects relate to the generation of hazardous hydrodynamic phenomena in the nearshore zone, while social aspects relate to the behaviour of beach visitors. The interplay between physical and social aspects is particularly strong, as these aspects act along the same part of the timeline of drowning. Here, the social aspect of coastal swimmer safety is reduced to the sheer presence of beach users. If the presence of beach users and hazardous hydrodynamics coincide in space and time, an actual recreational risk is constituted. Thirdly, predictability of recreational risks is a key aspect in mitigation of these risks. Predictability may act at different temporal and spatial scales. Predictability at larger and longer scales is typically the domain of coastal managers and engineers, while predictability at smaller and shorter scales occurs at the level of lifeguards and other rescue services.

In this synthesis, the framework for the assessment of coastal swimmer safety is applied to the case of the Sand Motor, a large-scale sand nourishment project at the Dutch North Sea coast that has been introduced in previous chapters. The aim is to demonstrate how application of the framework can assist in creating an integral overview of swimmer safety around a particular coastal intervention.

5.2. CASE STUDY: THE SAND MOTOR

This analysis of swimmer safety around the Sand Motor consists of several steps. First of all, potentially hazardous hydrodynamic phenomena are addressed. These

phenomena have been selected in the introduction of this thesis. Here, the potentially hazardous aspects of every phenomenon are described, along with an assessment of their predictability in space and time. Subsequently, an analysis of beach attendance at the Sand Motor is presented, focusing on its spatio-temporal predictability. Finally, the analyses of physical hazards and beach attendance are combined into a generic overview of swimmer safety at the Sand Motor.

5.2.1. HAZARDOUS HYDRODYNAMICS AT THE SAND MOTOR

Four potentially hazardous flow patterns were identified in the introduction of this thesis:

1. Tidal flow contraction

2. Tidal flow separation

3. Tidal pumping

4. Rip current generation

The first two phenomena are closely related and will therefore be treated together here.

TIDAL FLOW CONTRACTION AND SEPARATION

Tidal flow contraction and separation occur at mega nourishments, provided that the shape of the nourishment is pronounced enough and the tidal excursion is long enough compared to the size of the nourishment (see Chapter 3). Tidal flow separation has three main consequences for swimmer safety compared to the reference situation of a straight coastline: (1) intensified currents and offshore directed currents around the tip of the nourishment can carry swimmers away from the beach, (2) the alongshore direction and magnitude of the tidal current strongly varies in space and time around the nourishment, which reduces the short-term predictability of the tidal flow and (3) the magnitude of the tidal flow along the leeward edge of the nourishment is reduced, which temporarily creates a relatively calm and safe area.

   The predictability of tidal flow contraction and separation can be assessed at different levels. Generally, the predictability of tidal phenomena is relatively high (compared to the predictability of wave-related phenomena) due to the strong periodicity of tidal water level fluctuations and the dependence of tidal flow on stable, large-scale aspects of the coastal geometry rather than highly dynamic small-scale bathymetric features. This makes prediction of tidal currents on a daily basis more straightforward, for example using a numerical model or a tide table.

   At longer timescales, tidal flow characteristics around a beach nourishment (or other coastline perturbation) can be predicted with the help of the framework put forward in Chapter 3 of this thesis. The relation between tidal flow separation and the governing parameters K_C (Keulegan-Carpenter number) and α (nourishment aspect ratio) is shown in Figure 5.1, along with the position of the Sand Motor in this diagram at all stages of its development between 2011 and 2016. Ongoing erosion
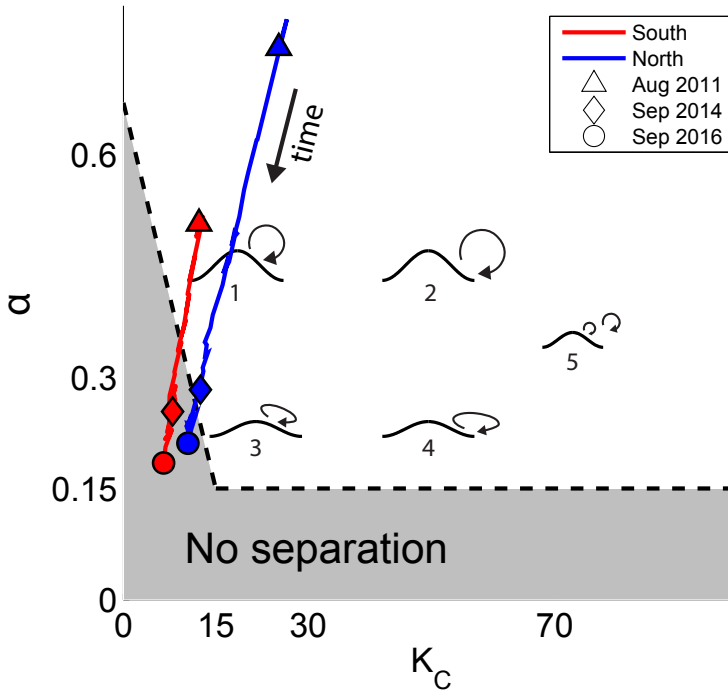
Figure 5.1: Temporal evolution of tidal flow separation at the Sand Motor visualised in the K_C-α plane. The markers indicate the start and end points of the bathymetric dataset, as well as the situation during the MegaPEX field campaign.

and alongshore diffusion of the mega nourishment induces a decrease over time of both K_C and α, which also decreases the likelihood of tidal flow separation at the Sand Motor over time. Additionally, due to the sightly asymmetric outline of the Sand Motor (De Schipper et al., 2016), its southern and northern side have a different aspect ratio. Furthermore, the difference in peak tidal flow velocity (ebb 0.5 m/s, flood 0.7 m/s used here, ignoring spring-neap modulation) leads to different values of K_C on both sides of the nourishment.

Measurements of the tidal flow field around the Sand Motor conducted in September 2014 showed clear signs of tidal flow separation and eddy generation at the northern side of the nourishment (flood flow), which is in agreement with the predictions in Figure 5.1. While the primary focus of the MegaPEX measurements was on the flood phase of the tide, several measurements with GPS-tracked drifters were undertaken during the ebb phase. None of these measurements showed clear signs of flow separation during ebb flow, which is reflected by the location of the red diamond marker in the 'no separation' area.

TIDAL PUMPING

If a tidal basin is present (referred to as *lagoon*) at the coastline, either man-made (Stive et al., 2013) or as a result of spit formation (Achete and Luijendijk, 2012), tidal

flow will develop in the entrance channel of the lagoon. If this tidal flow has considerable strength, it may constitute a hazard to swimmers and bathers. Even though the water depth in the channel might be limited and the flow inside the channel is confined between two sections of beach, the presence of a strong current may already cause distress to humans, as was explained in the introduction of this thesis and by De Zeeuw et al. (2012).

The predictability of this tidal phenomenon on a daily basis is relatively high compared to wave-related phenomena, provided that the geometry of the tidal basin and channel is known. Similar to tidal flow separation, the predictability of currents related to tidal pumping at longer timescales depends on the morphological evolution of the nourishment. The flow velocity U in a sandy tidal inlet is governed by the tidal range R, the surface area of the basin A_b, the cross-sectional area of the channel A_c and the length of the channel l_c.

The basic morphodynamic evolution of a coastal inlet tends towards an equilibrium situation (Escoffier, 1977). However, large and uni-directional alongshore sediment transport at the surrounding coastline can induce spit formation and alongshore migration of the inlet (e.g. Hayes, 1980), leading to a persistent increase of l_c and decrease of A_c. Eventually, the channel will silt up and tidal pumping will stop, unless a new channel forms due to breaching of the spit during storm conditions. The latter constitutes a dynamic equilibrium situation, which is also observed at the Sand Motor (Figure 5.2). An initial modelling study by De Vries et al. (2015) revealed that the mean water level in the lagoon was steadily rising, while the tidal range decreased significantly. This was confirmed in a more extensive modelling study (Figure 5.3, Huizer et al., 2018). Regarding the peak tidal flow velocities in the channel, long-term measurements or simulations showing the evolution over time are not available. Drifter observations and model simulations by Hoekstra et al. (2017) show that the tidal flow reached velocities up to 1 m/s in mid-2013. It is expected that the maximum velocity was even higher in 2012, when the channel had already narrowed but the tidal range inside the lagoon was still much larger.

RIP CURRENT GENERATION

Alongshore variability of sandbar patterns and associated rip currents are observed along many sandy beaches (e.g. Hino, 1974; MacMahan et al., 2005; Austin et al., 2010; Houser et al., 2013; Winter et al., 2014). Their strong, offshore directed currents that form close to the dry beach constitute a major hazard to swimmers and bathers (Brighton et al., 2013; Woodward et al., 2013; Arozarena et al., 2015; Barlas and Beji, 2016). The short-term predictability of rip currents is low compared to the tidal flow phenomena discussed above. Rip currents are primarily driven by differential wave breaking over variable topography, which makes adequate forecasts of the wave height, water level and nearshore bathymetry crucial for numerical model predictions. Although the capabilities of operational, large-scale wave models have improved significantly over the last decades (Booij et al., 1999; Wingeart et al., 2001), their predictive strength remains lower than for tidal models due to their large dependence on input from uncertain numerical wind field predictions. Furthermore, the dynamic character of nearshore bathymetry imposes uncertainties on operational rip current predictions, despite efforts to provide operational models with
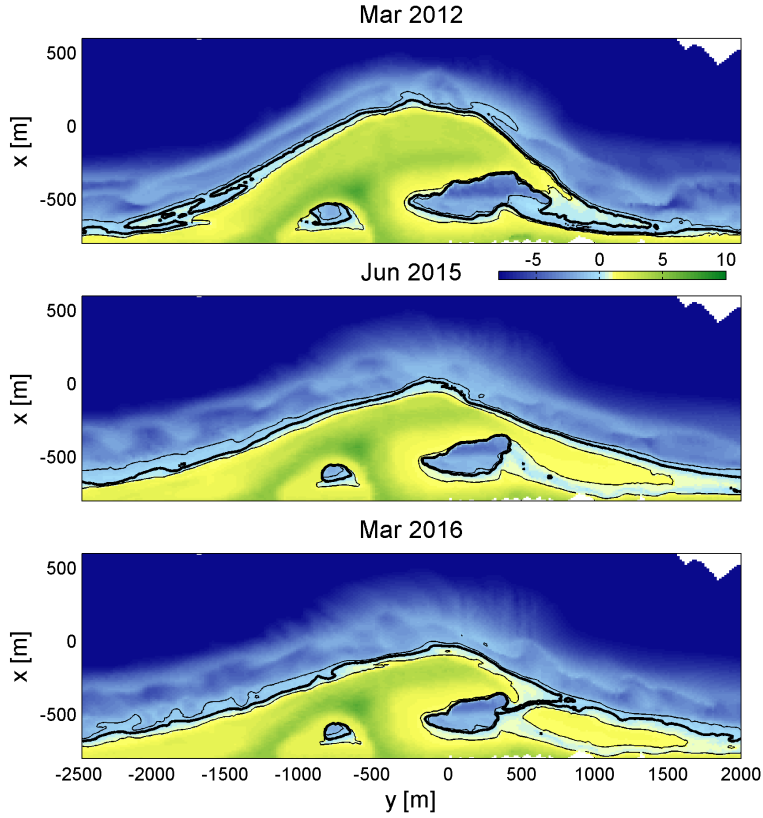
Figure 5.2: Evolution of the Sand Motor lagoon, showing the initial short channel (upper panel), length-ening and siltation of the channel through spit formation (middle panel) and breaching of the spit (lower panel). The background shading represents the bed level with respect to mean sea level. The thick line and bordering fine lines indicate the 0 m, +1 m and -1 m bed level contours respectively and serve as an approximation of the intertidal area.
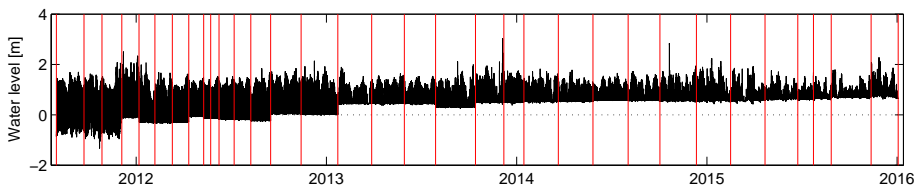

Figure 5.3: Modelled water level in the Sand Motor lagoon over the first 4.5 years after its construction as presented by Huizer et al. (2018). Vertical red lines indicate updates of the model bathymetry based on the Sand Motor survey dataset (De Zeeuw et al., 2017). Breaching occurred in January 2016, just after the end of the timeseries.

up-to-date bathymetry from remote sensing sources (Sembiring et al., 2014, and Chapter 4 of this thesis).

The long-term predictability of rip currents around sand nourishments is closely related to the ways in which a nourishment can influence sandbar variability. Sand nourishments might affect the formation of sandbar patterns and generation of rip currents through three different mechanisms. First of all, the implementation of a beach nourishment modifies the cross-shore beach profile. Often, the pre-existing bar is buried and a relatively steep slope is constructed in the upper part of the profile. Reworking of this man-made profile through natural morphodynamics typically leads to the formation of a new sandbar that may have different characteristics than the pre-existing bar. This was also observed at the Delfland coast after the implementation of an extensive beach nourishment program between 2009 and 2012 (see chapter 2 of this thesis), where the new sandbar was found to become more variable. Secondly, the alongshore transitions of a nourishment to the adjacent, unnourished stretch of beach can be rather abrupt. This may lead to discontinuities in the sandbar crests, as was also observed in the alongshore transition zones of the Sand Motor (Radermacher et al., 2017b). The third mechanism specifically relates to mega nourishments. Due to their large size, they can induce strong changes in the local coastline orientation, which in turn leads to changes in the nearshore wave climate. As the formation of sandbar patterns depends on the incoming wave energy (De Schipper et al., 2013) and direction (Calvete et al., 2005; Garnier et al., 2008; Thiébot et al., 2012), sandbars fronting a mega nourishment may exhibit varying behaviour at different alongshore locations (Rutten et al., 2017c). Particularly, the southern half of the Sand Motor receives more normally-incident wave energy than the adjacent coastline, which may have resulted in the formation of highly pronounced crescentic sandbars in early 2015 (Radermacher et al., 2017b; Rutten et al., 2017c, and Chapter 2 of this thesis).

Quantitative observations of rip currents are typically collected during short-term, labour-intensive field experiments. The rapid evolution of nearshore morphology inhibits long-term deployments of fixed in-situ sensors, because instruments are prone to burial and the focus area of the measurement (the rip channel) migrates over time. Alternative techniques to obtain information on rip current occurrence and/or strength over longer periods and at larger scales include video observations (Bogle et al., 2001; Gallop et al., 2009) and assessments of alongshore variability in the underlying bathymetry (De Schipper et al., 2013; McCarroll et al., 2017; Radermacher et al., 2017b). The latter approach relates to the historical assessment of alongshore subtidal sandbar variability at the Delfland coast in chapter 2 of this thesis. However, an alongshore variable nearshore morphology forms only half of the conditions needed for rip current generation, wave breaking on the sandbar being the other half. Predictability of the latter aspect is treated in Section 5.2.3.

5.2.2. Beach attendance

The presence of beach users forms an indispensable part of the framework for coastal swimmer safety as put forward in the introduction of this thesis. Potentially hazardous hydrodynamic phenomena as addressed in the previous section only form

an actual risk if they coincide in space and time with the presence of beach users. The spatial and temporal aspects are treated separately here.

Temporal distribution of beach attendance

Previous studies into beach attendance have mostly made use of operational coastal camera stations combined with automated beach user detection algorithms (Kammler and Schernewski, 2004; Jiménez et al., 2007; Guillen et al., 2008; Balouin et al., 2014; Trygonis et al., 2015). All of these studies show that beach attendance is strongly linked to the following parameters:

- Weather: temperature, sunshine, cloud cover, wind speed, rainfall (higher beach attendance on warm, sunny, unclouded days with low wind speed and no rainfall)

- Time of day (higher beach attendance in the afternoon)

- Day of the week (higher beach attendance during weekends)

- Holiday season (higher beach attendance during summer vacation)

In relation to swimmer safety, the temporal distribution of beach attendance only holds relevance for wave-related hazardous hydrodynamics. The wave climate on a wind-sea dominated coast is highly correlated with the local weather and is therefore expected to be correlated with beach attendance as well. In contrast, tidal flow phenomena do not exhibit a major correlation with the weather and can occur at any moment throughout the day (without prior knowledge of the tidal phase).

A study into beach attendance at the Delfland coast was performed bij Gulden (2017), based on operational imagery from a camera station at Kijkduin, approximately 4 km north of the Sand Motor, employing an advanced coastal image classification toolbox (Hoonhout et al., 2015). Beach attendance data obtained by Gulden (2017) throughout the summer months of 2013 are used here to verify that the supposed relations between beach attendance and weather-related parameters hold for the Delfland coast. To this end, a beach weather index I_{BW} is calculated in accordance with Table 5.1, taking into account temperature, sunshine, cloud cover, rainfall and wind. For calculation of I_{BW}, meteorological observations were obtained from the Royal Dutch Meteorological Institute (KNMI) for the Valkenburg (cloud cover) and Hoek van Holland (all other parameters) stations.

The beach weather index shows a clear relation with the number of beach users detected at Kijkduin by Gulden (2017) (Figure 5.4). Beach attendance was quantified from webcam images three times per day (late morning, early afternoon, late afternoon). For $I_{BW} < 6$, virtually no beach users are present, while for I_{BW} between 6 and 11 a rising trend is visible. Hence, I_{BW} can be used as an acceptable proxy for beach attendance at the Delfland coast.

Spatial distribution of beach attendance

The spatial distribution of beach users is typically non-uniform (Jiménez et al., 2007) and is influenced by the proximity of beach entrances, parking facilities, holiday

Table 5.1: Calculation of the beach weather index, where T_{max} denotes the daily maximum temperature, t_{sun} is the daily sunshine duration, C_c is the cloud cover on a scale between 0 (clear skies) and 9 (overcast), t_{rain} is the daily rainfall duration and W is the wind force. The value of I_{BW} equals the sum of all parameter scores in the table.

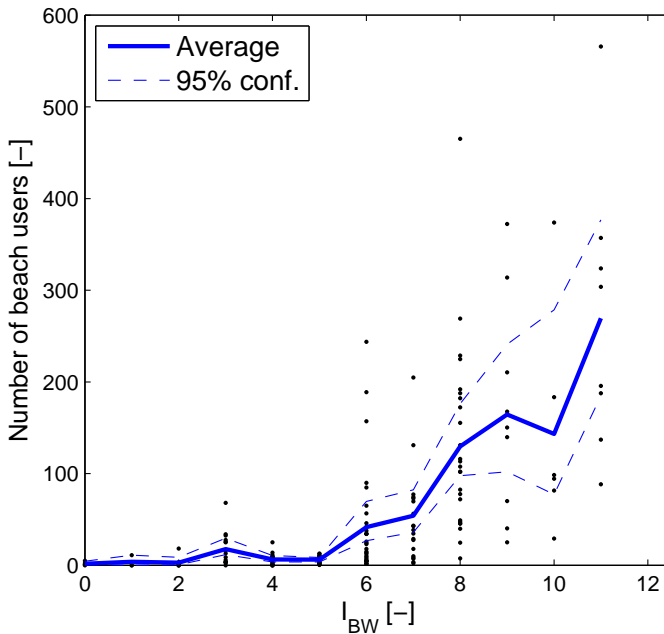| Parameter	Range	Score
T_{max} [°C]	< 20	0
	$20 - 25$	2
	≥ 25	4
t_{sun} [h]	< 5	0
	$5 - 10$	1
	≥ 10	2
C_c [-]	≥ 6	0
	$4 - 6$	1
	< 4	2
t_{rain} [h]	≥ 3	0
	$1 - 3$	1
	< 1	2
W [Bft]	≥ 4	0
	$2 - 3$	1
	< 2	2

Figure 5.4: Comparison of I_{BW} and beach attendance data at the beach of Kijkduin (alongshore length ~ 400 m) for the summer months of 2013 (Gulden, 2017). Solid line represents I_{BW}-averaged beach attendance including bootstrapped 95% confidence intervals around the average.

residences, the waterline and beach facilities. Only once the beach attendance approaches the maximum capacity of the beach (saturation conditions), the spatial distribution becomes near-uniform, as was observed at crowded urban beaches in Barcelona, Spain (Guillen et al., 2008).

At the Sand Motor, several of these influencing factors play a very important role (Figure 5.5). The accessibility of the Sand Motor peninsula is relatively low due to its large distance from holiday residences, car parkings, beach restaurants and coastal towns. Furthermore, even though two beach entrances are located at the pensinsula, the walking distance from these beach entrances to the waterline is much longer (500 - 1000 m) than at the adjacent beaches (150 m). As a result, beach users tend to cluster near the northern and southern ends of the Sand Motor, which is illustrated using images from the Argus camera station at the Sand Motor (Figure 5.6).

5.2.3. Swimmer safety: combining hazardous hydrodynamics and beach attendance

Based on the spatial and temporal distributions of beach users and hazardous hydrodynamic phenomena at the Sand Motor, an integral view of swimmer safety can be created. Again, a distinction is made between temporal and spatial coincidence of hazardous hydrodynamics and beach attendance.

Due to the correlation between weather-related parameters and the local wave climate, it is expected that a correlation exists as well between beach attendance and the wave climate. This relation is explored in more detail here. The beach weather index was shown to be a useful indicator of beach attendance and will therefore be used as a proxy.

The temporal occurrence of rip currents, which are the only wave-driven hydrodynamic phenomenon in this study, typically depends on a range of parameters, the most important ones being the wave height (Lushine, 1991; Dusek and Seim, 2013; Moulton et al., 2017), alongshore variability of the bathymetry (Kennedy et al., 2008; Wilson et al., 2013; Castelle et al., 2014; McCarroll et al., 2017), water level (Austin et al., 2014; Bruneau et al., 2014) and wave obliqueness (Houser et al., 2013; Winter et al., 2014; Moulton et al., 2017). Only wave height is used for analysis here, as its correlation with the weather is much stronger than for the other parameters. Wave conditions at 10 m water depth offshore of the Sand Motor between 2010 and 2017 were obtained with an extensive wave transformation table for the Dutch coast (Tonnon and Briere, 2011). A comparison of the daily maximum value of the significant wave height $H_{s,max}$ against I_{BW} reveals the expected trend (Figure 5.7). High I_{BW} generally corresponds with low $H_{s,max}$, while higher wave heights are only observed for low I_{BW} .The beach attendance statistics in Figure 5.4 indicated that beach attendance incidentally reaches intermediate values at $I_{BW} = 6$ or 7, while days with high beach attendance have $I_{BW} >= 8$.

The interpretation of Figure 5.7 depends on the relation between $H_{s,max}$ and the generation of rip currents. Although other parameters were found to influence rip current generation as well, the influence of the wave height can be assessed through the construction of a breaker parameter $\gamma = H/h$, where H denotes the wave height

Figure 5.5: Recreational map of the Sand Motor. Satellite imagery from Google Earth.
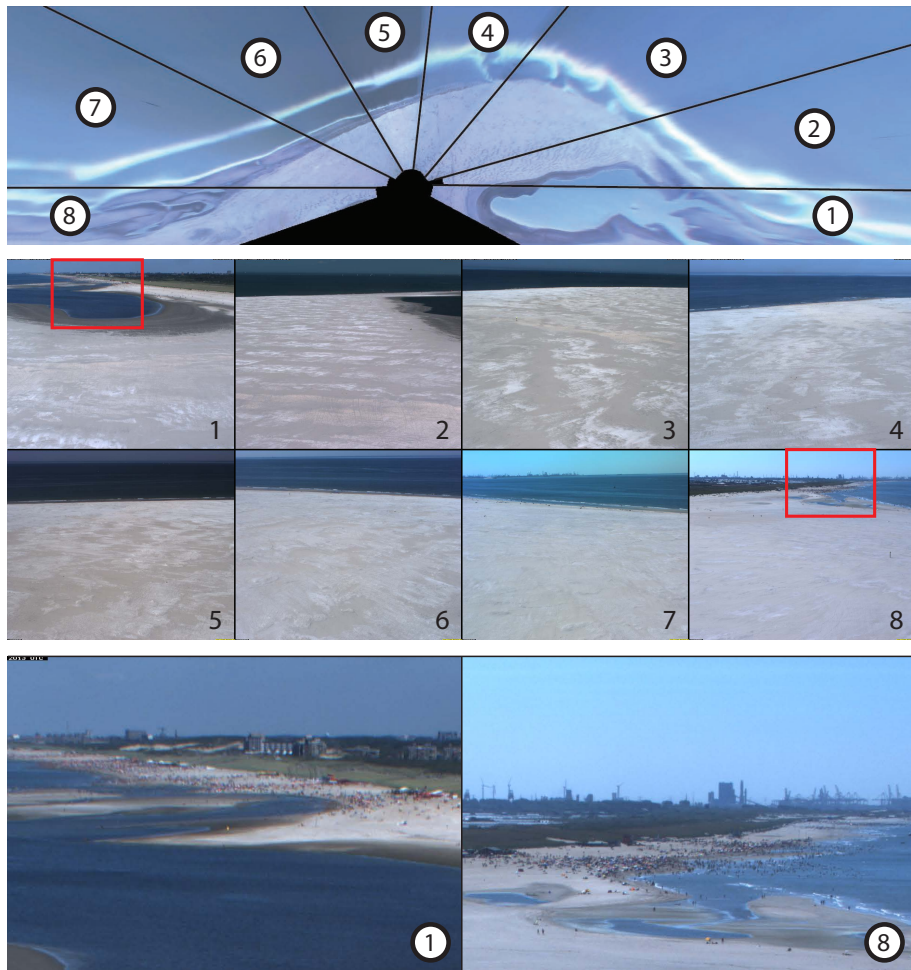

Figure 5.6: Orientation of camera views at the Sand Motor Argus camera station (top panel, after Rutten et al., 2017a). Spatial distribution of beach attendance at the Sand Motor on 1 August 2013, 14h00 local time ($I_{BW} = 11$), as observed from the Argus cameras (middle panel). Magnifications of camera views 1 and 8, revealing the presence of beach users (bottom panel).
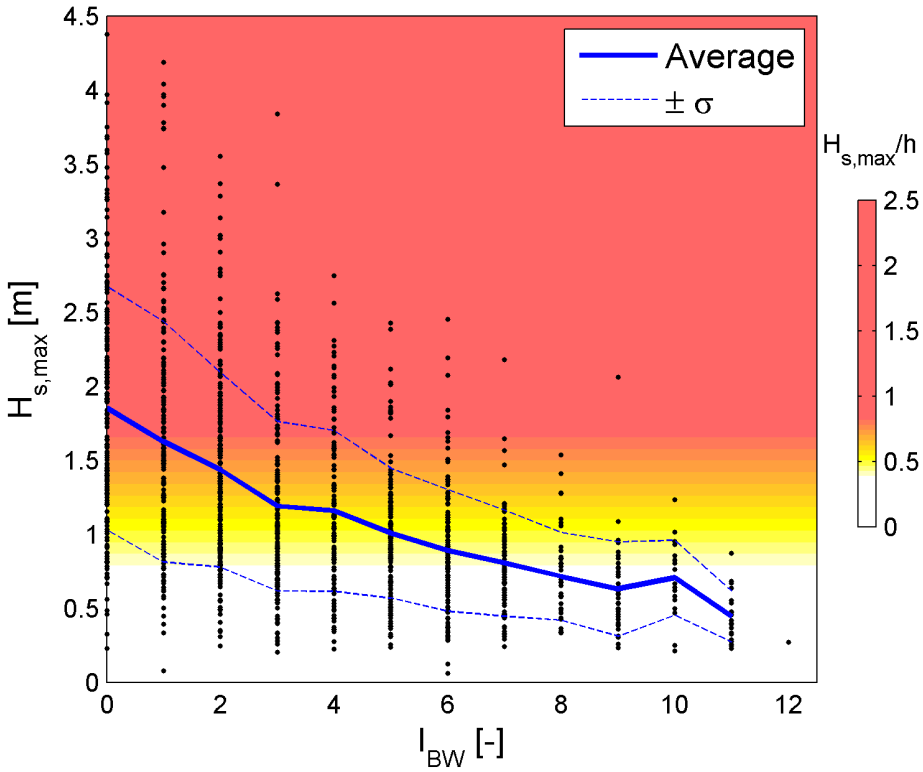
5

Figure 5.7: Daily maximum of significant wave height versus beach weather index between 2010 and 2017.
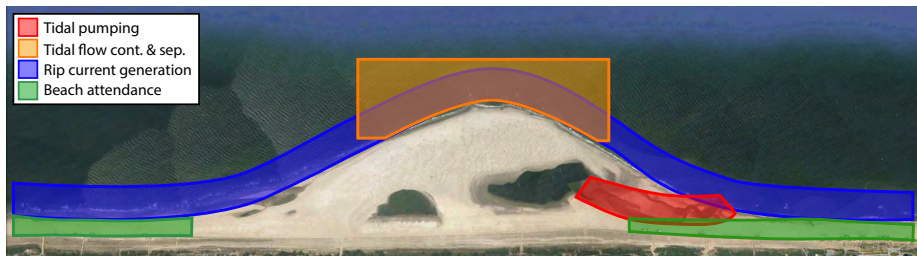

Figure 5.8: Spatial coincidence of hazardous hydrodynamic phenomena and beach attendance. Satellite imagery from Google Earth.

Table 5.2: Overview of coincidence of hazardous hydrodynamics with beach attendance at the Sand Motor.

Hydrodynamics	Temp. coincidence	Spat. coincidence	Risk
Tidal flow contr. and sep.	high	low	low
Tidal pumping	high	high	high
Rip current formation	low	high	low

of an individual wave and h denotes the local water depth. Generally, wave breaking occurs around $\gamma = 0.8$. The highest waves in the field have a wave height of approximately $H_{max} = 2H_s$, implying that wave breaking starts around $H_s/h = 0.4$. Provided that wave breaking occurs on an alongshore variable bar crest, the flow velocity of the generated rip current will increase with increasing H_s/h until waves start breaking in the rip channel as well (Moulton et al., 2017). It was shown in chapter 2 of this thesis that alongshore variable sandbar crests were present at the Delfland coast after construction of the Sand Motor with a bar crest level around $z_b = -2.5$ m. Taking into account a minimum tidal water level of around -0.5 m, the water depth on these bar crests at low water is approximately $h_b = 2$ m. Based on these considerations, the background shading of $H_{s,max}/h$ in Figure 5.7 has been constructed. It shows that on days with $I_{BW} > 8$, wave breaking on the subtidal sandbar is rare and the associated risk of rip current generation is low. For $I_{BW} = 6$, which was found to be a lower limit for days with non-zero beach attendance, the probability of wave breaking on the subtidal sandbar is considerably higher.

The spatial coincidence of beach users and hazardous hydrodynamics is assessed in Figure 5.8. The joint approximate extent of hazardous hydrodynamic phenomena and beach attendance is shown. As explained in the introduction of this thesis, in order to determine spatial coincidence, only the alongshore dimension is considered (Houser et al., 2015), assuming that beach users will enter the water at approximately the alongshore location where they have placed their belongings. Alongshore coincidence of beach users and hazardous hydrodynamics occurs for tidal pumping and rip current generation, but not for tidal flow separation. This pattern implies that the risk associated with tidal flow separation is relatively small, since beach users are largely absent in the area where the tidal flow separates.

An overall view of swimmer safety at the Sand Motor can now be created by combining the findings regarding temporal and spatial coincidence of beach users and hazardous hydrodynamics (Table 5.2 and Figure 5.9). **Tidal pumping has a high spatial and temporal coincidence with beach attendance and therefore constitutes the primary swimmer safety risk at the Sand Motor. Tidal flow separation has a high temporal but low spatial coincidence with beach attendance, limiting its risk. In contrast, rip current formation has a high spatial but low temporal coincidence with beach attendance, which again limits its risk.**
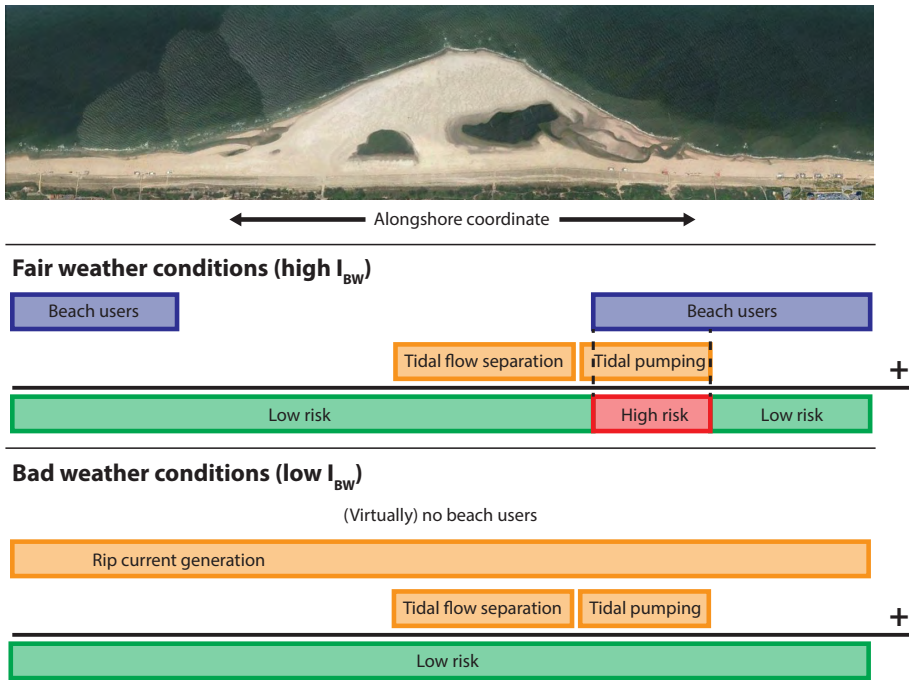
Figure 5.9: Spatial and temporal (through I_{BW}) coincidence of hazardous hydrodynamic phenomena and beach attendance at the Sand Motor, constituting the swimmer safety risk level.

5.3. DISCUSSION

The considerations regarding swimmer safety risk in the previous section constitute a case study for the Sand Motor, but the applied methodology is part of a more generic framework for the assessment of coastal swimmer safety. In this section, two additional swimmer safety risks at the Sand Motor are treated that have not been covered in the preceding analysis. Furthermore, the observed swimmer safety at the Sand Motor since its construction is discussed. Finally, the consequences for the framework and the results when applied to different geographic locations are discussed.

ADDITIONAL RISKS AT THE SAND MOTOR

Two potentially important hazardous hydrodynamic phenomena at the Sand Motor have not been addressed in this thesis, being the risk of tidal trapping and the risk of rip current generation over intertidal bathymetry. The first aspect is related to the vast intertidal beach area at the sand spit along the northern edge of the Sand Motor (see Figure 5.2). Beach users may find themselves isolated on an island by the rising tide, which forces them to take hazardous escape routes through the entrance channel(s) of the lagoon. While these beach users might not have the intention to enter the water (e.g. because they are undertaking a beach hike), they are forced to do so by tidal trapping. Beach hiking has a much weaker correlation with I_{BW}

than other forms of beach recreation, as it is a popular activity during dry weather conditions in all seasons. Therefore, the risk of tidal trapping is not restricted to a handful of warm summer days, but can occur throughout the year. Furthermore, the spatial distribution of beach hikers over the Sand Motor does not adhere to the patterns presented in Figure 5.6 as a result of the willingness of hikers to move over large distances. Enjoyable landscape features such as the sand spit may even attract hikers. Tidal trapping thus has a relatively large spatial and temporal coincidence with beach attendance and forms an important recreational risk at the Sand Motor.

The second additional risk at the Sand Motor relates to rip current generation over intertidal bathymetry. The assessments in the previous section and chapter 2 of this thesis focus on alongshore variability of subtidal bathymetry. It was shown that, although alongshore variability of subtidal bathymetry can be relatively high at the Delfland coast, the temporal coincidence of rip currents generated over subtidal bathymetry and beach users is low. However, that analysis relied on the relatively high water depth above subtidal sandbar crests, which does not hold in the case of intertidal bathymetry. Wave breaking on variable intertidal bars can occur throughout the tidal cycle and over a large range of wave conditions. Although the hydrodynamic forcing of intertidal rip currents is expected to be significantly weaker than for subtidal rip currents (due to lower wave energy and shorter scale bathymetric variability), temporal coincidence of intertidal rip currents and beach users is high. Addressing this risk remains a major, important scientific challenge in the field of coastal swimmer safety. Analysis is complicated due to the small spatial and temporal scales that govern intertidal hydrodynamics and morphodynamics, which hampers collection of adequate field observations of bathymetry and currents.

OBSERVED SWIMMER SAFETY AT THE SAND MOTOR

The considerations on swimmer safety at the Sand Motor put forward in this chapter are purely based on the combination of information regarding physical hazards and beach attendance. Theoretically, this analysis can be verified by comparing the presented outcomes to the actual swimmer safety situation at the Sand Motor since its construction in 2011. This methodology has been applied before to validate predictions of rip current-related risks (Dusek and Seim, 2013; Scott et al., 2014). A similar study for the Sand Motor is complicated due to the lack of structured rescue data collection. Yearly evaluation reports of recreational safety at the Sand Motor (years 2012 through 2016) are the only available source of information (Royal-HaskoningDHV, 2013, 2014, 2015a,b, 2017). In total, 15 relevant incidents were selected from these reports (disregarding incidents related to lost children, violation of law, kitesurfing accidents and suicide attempts, which together form the majority of reported incidents). Tidal trapping plays a role in 7 of the 15 incidents, while the other 8 incidents are related to rescued swimmers and bathers. Clear descriptions of the causes that distressed the swimmers and bathers involved are lacking, making it difficult to attribute incidents to the various physical hazards identified in this thesis.

Furthermore, it is noted that preventive actions by lifeguards, such as warning of swimmers and bathers before they are actually endangered by hazardous hydrodynamics, are typically not documented in the yearly evaluation reports. It is expected

that numerous preventive actions are taken every year by lifeguards, rescue services and bystanders. Therefore, the relatively low number of reported severe incidents at the Sand Motor between 2012 and 2016 does not provide a complete, representative view of the actual swimmer safety situation. The latter could only be obtained through adequate, structured collection of all relevant information regarding the actions of lifeguards and other rescue services, which is not available for the Sand Motor.

CONSEQUENCES OF A DIFFERENT GEOGRAPHIC LOCATION

The analyses of coastal swimmer safety presented in this thesis are all based on the hydrodynamic and recreational boundary conditions of the Sand Motor and the adjacent Delfland coast. The hydrodynamic forcing at the Delfland coast is characterised by relatively strong alongshore tidal currents in the order of 70 cm/s, a tidal range of approximately 1.5 - 2 m and a wave climate that is dominated by locally-generated wind waves with highly oblique wave directions. This situation is typical for marginal sea coasts at mid-latitudes, but can be very different from open ocean beaches. The latter commonly have a small tidal range, weak tidal currents and a wave climate with an energetic swell component. This reduces the physical hazards associated with tidal flow phenomena, such as tidal flow separation, tidal pumping and tidal trapping. In turn, the importance of wave-related phenomena might increase.

The temporal coincidence of rip current generation on subtidal bars and beach attendance was assessed in Figure 5.7 for the Delfland coast. A similar comparison is now made for Virginia Beach at the west coast of the United States, where adequate offshore wave observations (wave buoy CHLV2) and onshore meteorological observations (Norfolk International Airport meteo station) are publicly available from the United States National Oceanic and Athmospheric Administration (NOAA) between 1990 and 1995 (Figure 5.10). Although observations of subtidal barcrest levels at Virginia Beach are not available, an approximate rip current risk classification is made in the figure through shading of the bars based on $H_{s,max}$. The chosen threshold levels are very similar to those chosen by Lushine (1991) for his rip current scale, which was established based on observations from the US east coast. The figure illustrates the difference in wave-related recreational risks between both types of coast: medium to high-energy waves on high I_{BW} days are more common along open ocean (48% of days with $I_{BW} \geq 8$ have $H_{s,max} \geq 0.75$) coasts than along marginal sea coasts (7%). Additionally, in this particular case, the percentage of high I_{BW} days at Virginia Beach is much higher than at the Delfland coast, which is related to their difference in latitude (36° North at Virginia Beach compared to 52° North at the Sand Motor) and the influence of warm ocean currents. A higher absolute number of high I_{BW} days is likely to yield a higher annual beach attendance (disregarding the 'popularity' of the beach) and therefore a larger exposure of beach users to the local hydrodynamic hazards. Altogether, these aspects partly explain the large number of rip current victims at open ocean coasts (Klein et al., 2005; Brighton et al., 2013; Arozarena et al., 2015) compared to the Dutch North Sea coast (De Zeeuw et al., 2012, and Appendix A), although the presence and efficiency of lifeguards and other rescue services has a large impact as well.
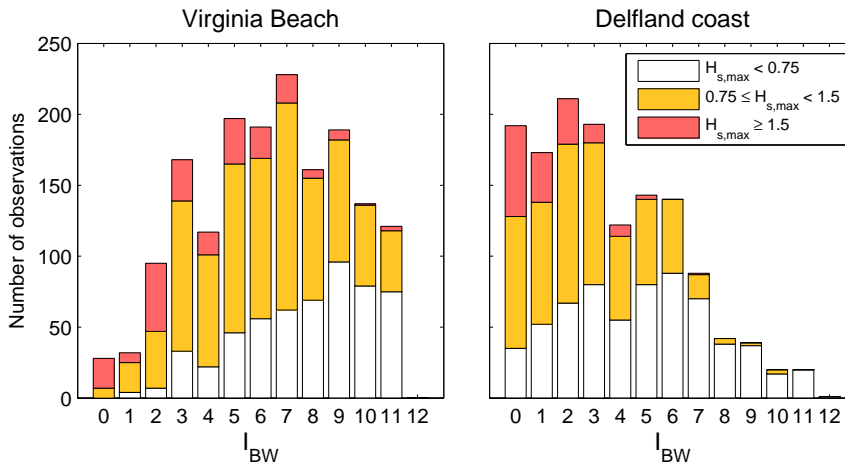
Figure 5.10: Comparison of the relationship between $H_{s,max}$ and I_{BW} for an open ocean beach (Virginia Beach, VA, USA) and a marginal sea coast (Delfland coast).

Finally, the influence of varying geographic location on the spatial distribution of beach users is discussed. At the Sand Motor, beach users were found to cluster in the transition areas between the nourishment and the adjacent coastline. This was mainly attributed to the proximity of the waterline, beach facilities and coastal towns. Even for the Sand Motor case, one might wonder what the effect of an along-shore shift of the Sand Motor would be, placing the peninsula right in front of one of the coastal towns. It is likely that beach attendance around the tip of the nourishment would increase compared to the present situation. Furthermore, if the beach under consideration is not part of a continuous stretch of sandy coast, but an isolated urban beach (such as the beaches analysed by Guillen et al., 2008), beach attendance is more likely to reach saturation conditions. This increases the probability of beach users accepting the long walk towards the tip of the peninsula. The same effect is expected if the walking distance to the shoreline is reduced due to a smaller cross-shore dimension of the nourishment project.

5.4. CONCLUSIONS

An application of a generic framework for swimmer safety to the Sand Motor case was presented in this chapter. The framework adopts the notion of a swimmer safety risk being the coincidence in space and time of hazardous hydrodynamics and beach users. The spatial and temporal coincidence of three potentially hazardous hydrodynamic phenomena and beach users have been assessed here, illustrating the important role of beach attendance in swimmer safety.

Tidal pumping in the entrance channel to the Sand Motor lagoon coincides in space and time with beach users during fair weather conditions, constituting a considerable risk for swimmers and bathers at the Sand Motor. In contrast, tidal flow separation has a large temporal, but small spatial coincidence with beach users

and therefore represents a limited recrational risk at the Sand Motor. Finally, it was shown that although rip currents may occur along the full contour of the nourishment, rip current generation is typically limited to relatively bad weather conditions. As a result, it has a large spatial, but small temporal coincidence with beach users, constituting a limited risk. These findings suggest that rip currents may not have a large impact on swimmer safety along mid-latitude marginal sea coasts.

Finally, the influence of geographic location on coastal swimmer safety was addressed. It was found that at open ocean coastlines, wave-related hydrodynamic hazards are more common than at marginal sea coasts (such as the Delfland coast). In turn, tidal phenomena are expected to play a minor role at open ocean coasts. The spatial distribution of beach users, which has important consequences for swimmer safety at Sand Motor, can be different (primarily more uniform) if the beach or nourishment project under consideration is closer to coastal towns and beach facilities and the available beach area is restricted.

The generic framework for coastal swimmer safety put forward in this thesis proved to be a useful method to create an overview of swimmer safety risks at a particular beach or nourishment project. It allows for a qualitative comparison of the risks associated with various hazardous hydrodynamic phenomena at the Sand Motor. It is expected that the framework is a valuable tool for the design and evaluation of coastal interventions.

6

CONCLUSIONS

The execution of large sand nourishments along recreational beaches may adversely affect swimmer safety. The aim of this thesis as presented in Chapter 1 was:

To determine and understand how a mega-scale sand nourishment influences nearshore hydrodynamics and thereby affects swimmer safety.

One potential impact of sand nourishments on swimmer safety is the formation of alongshore variable subtidal sandbars, which in turn may lead to the generation of rip currents. The Delfland coast, a 17 km long coastal cell at the Dutch North Sea coast, has received more than 20 sand nourishments of various types and sizes over the last three decades, including the Sand Motor mega nourishment in 2011.

1. What is the influence of ongoing sand nourishments on the existence and behaviour of subtidal sandbars at the Delfland coast?

Ongoing sand nourishments at the Delfland coast have largely determined the existence and behaviour of subtidal sandbars at the Delfland coast from 1986 onwards. The exact influence of nourishments on subtidal sandbar dynamics exhibited strong dependence on nourishment type. Beach nourishments promoted the formation of new sandbars within 3 years after execution of the nourishment. Shoreface nourishments induced onshore migration of the nourishment as well as the pre-existing sandbar. Typically, the shoreface nourishment migrated towards the former position of the pre-existing sandbar, forcing the pre-existing sandbar to weld onshore. The Sand Motor, being the only mega nourishment at the Delfland coast, behaved as a regular beach nourishment in terms of cross-shore bar development. Within 1 year after construction of the Sand Motor, a new subtidal sandbar developed along the full nourishment.

The influence of sand nourishments on subtidal sandbar development at the Delfland coast is illustrated by three distinct transition points. The first transition occurred in 1986, when the first (large) beach nourishment was implemented in the unnourished system. The unnourished system was characterised by the absence of

a subtidal sandbar at the central section of the coastal cell. After implementation of the 1986 beach nourishment, a subtidal sandbar started forming in the central section of the Delfland coast as well. The second transition occurred around 1998, when the first shoreface nourishment was implemented at the Delfland coast. Before 1998, sandbar migration at the Delfland coast was generally directed offshore. After 1998, sandbars (including former shoreface nourishments) generally migrated onshore. The third transition took place between 2009 and 2012, when a series of nourishments ($\sim 37.5 \, \text{Mm}^3$ of nourished sand, including the Sand Motor) led to the formation of a new, shallow sandbar along the entire Delfland coast with a high degree of alongshore variability. Alongshore sandbar variability had been low before this transition period, except for the alongshore end points of shoreface nourishments during their onshore merging sequence.

Altogether, these findings imply that individual nourishments can influence the formation and migration of individual sandbars, while continued nourishments can fundamentally change long-term sandbar dynamics along an entire coastal cell.

Addtionally, mega nourishments may perturb the alongshore tidal current. If the tidal flow separates from the shoreline at the nourishment, offshore directed currents can occur, posing a potential threat to swimmers and bathers.

2. What are the characteristics of the tidal flow field around mega-scale beach nourishments under varying nourishment geometry and tidal conditions?

Mega nourishments act as a perturbation to the alongshore tidal flow. Field observations in 2014 confirmed that tidal flow separation and eddy generation occurred during flood flow at the northern side of the Sand Motor at that stage of its morphological development. The intensity of the generated tidal eddies modulated with the spring-neap cycle, with the strongest eddies occurring during spring tide.

Simulations of the tidal flow field around mega nourishments of varying size and shape in a validated numerical model revealed that tidal flow separation and eddy generation occur if the nourishment is pronounced enough and the tidal excursion is long enough compared to the alongshore nourishment size. The size, intensity and longevity of generated tidal eddies depend on the size and shape of the nourishment. Tidal eddies forming due to flow separation at a mega nourishment can reach a diameter that is considerably larger than the cross-shore dimension of the nourishment itself.

Mitigation of swimmer safety risks is closely related to the ability to predict the occurrence of hazardous hydrodynamic phenomena. Nearshore hydrodynamics are strongly influenced by seabed topography, which can change rapidly as a result of surfzone morphodynamics. Therefore, the inclusion of remotely-sensed, up-to-date nearshore bathymetry potentially improves the performance of operational numerical rip current predictions.

3. What is the influence of remotely-sensed bathymetry input on numerical simulations of nearshore hydrodynamics?

Numerical model predictions of rip currents based on remotely-sensed bathyme-

try input have predictive value. Out of all rip currents predicted on an accurate, in-situ measured bathymetry, 55% could be reproduced on the remotely-sensed bathymetry. The system is prone to false negatives (45% of rip currents predicted on the in-situ bathymetry are not reproduced on the remotely-sensed bathymetry) but produces a very low percentage of false positives (only 9% of rip currents predicted on the remotely-sensed bathymetry did not occur on the in-situ bathymetry).

Locally-derived errors in remotely-sensed bathymetry could be used to estimate local performance of the rip current prediction system. Especially the ability of the applied depth inversion algorithm to reproduce nearshore sandbar patterns and amplitudes at horizontal length scales between 200 and 400 m was found to determine the quality of rip current predictions. No clear dependence of the system's performance on hydrodynamic parameters (rip current intensity, alongshore current intensity and incoming wave angle) could be identified. The results imply that locally-derived bathymetric error metrics are to be preferred over domain-wide bulk error metrics when assessing the influence of bathymetric errors on nearshore current predictions.

Applying the knowledge obtained regarding potentially hazardous hydrodynamic phenomena to the Sand Motor case, a generic overview of swimmer safety around this particular mega nourishment can be created.

4. What is the effect of the Sand Motor mega nourishment on swimmer safety?

In this thesis, a generic framework for coastal swimmer safety was put forward, which proved to be a useful method for the assessment of swimmer safety risks at a particular beach or nourishment project. The framework consists of three main components. The first component is the notion that swimmer safety can be affected at any point along the timeline of drowning, which describes the steps leading to coastal drowning. The second component is the notion that the role of engineers in improving swimmer safety lies in increasing the predictability of swimmer safety risks. The third component is the notion of swimmer safety risk as the coincidence in space and time of hazardous hydrodynamics and beach users.

At the Sand Motor, three different potentially hazardous hydrodynamic phenomena were identified: tidal flow contraction and separation, rip current generation and tidal pumping. Tidal pumping was found to be the single largest swimmer safety risk at the Sand Motor during the first years after construction of the nourishment, due to the high spatial and temporal coincidence of tidal pumping with the presence of beach users. Over the course of several years, the flow velocities in the tidal channel diminished as a result of ongoing morphodynamic evolution of the mega nourishment.

Tidal flow separation posed a limited swimmer safety risk, due to its low spatial coincidence with beach attendance. At the Sand Motor, beach users tend to cluster around the connection points between the nourishment and the adjacent coastline as a result of the spatial distribution of recreational facilities. This resulted in low beach attendance at the most seaward point of the nourishment, where hazardous currents due to tidal flow separation may occur. Over time, the impact of the Sand Motor on the alongshore tidal current diminishes due to ongoing alongshore diffu-

sion of the nourishment.

The swimmer safety risk associated with rip current generation over subtidal sandbars was found be low at the Sand Motor, due to its low temporal coincidence with beach attendance. At the Dutch North Sea coast, the wave height is negatively correlated with beach attendance. The probability of wave breaking over subtidal sandbars on days with considerable beach attendance is very limited due to the local wind sea climate. This relation was shown to be very different at open ocean coastlines, where the coincidence of rip current generation and beach attendance is expected to be much higher.

The generic framework for coastal swimmer safety put forward in this thesis proved to be a useful method to create an overview of swimmer safety risks at a particular beach or nourishment project. It allows for a qualitative comparison of the risks associated with various hazardous hydrodynamic phenomena at the Sand Motor. It is expected that the framework is a valuable tool during the design and evaluation stages of coastal interventions.

6

A

COASTAL DROWNING

An important implication of the present study is the ability to include swimmer safety considerations into the design process of coastal interventions. The importance of swimmer safety as a design requirement is illustrated by statistics of coastal drowning and surfzone rescues. Both global and national (Dutch) statistics are presented.

A.1. GLOBAL STATISTICS

Studies into nearshore hydrodynamics are often justified based on a collection of coastal drowning and rescue statistics. Typically, reported figures are confined to a specific country or region. For example, Brighton et al. (2013) report 88 coastal drownings and 13,000 rescues by lifeguards per year in Australia. Attard et al. (2015) estimate that in addition, a similar annual number of rescues is conducted in Australia by surfers. Furthermore, according to Brighton et al. (2013), the annual number of surfzone rescues amounts 58,000 in the United States, 1,500 in the United Kingdom and 1,600 in New Zealand. In Costa Rica, on average 49 coastal drownings occur per year (Arozarena et al., 2015). Barlas and Beji (2016) report 48 coastal drownings per year at the Black Sea beaches of the Istanbul region. The annual number of coastal drownings in Israel amounts 36 (Hartmann, 2006).

Despite the specific character of these statistics, they can be used to interpret global mortality data, which are published by the World Health Organization (WHO). These data contain reported and estimated numbers of fatalities per country, year, sex and death cause. The standard system for death cause classification is *ICD-10* at present, in which coastal drowning is part of the chapter *External causes of morbidity and mortality*, section *Accidental drowning and submersion*, code W69: *Drowning and submersion while in natural water* (which excludes drowning due to falling into natural water). This category also includes accidental drowning in lakes and rivers, which hampers interpretation of the data. The number of reported deaths in category W69 in 2013 was 11,260, while the total reported number of accidental drownings and submersions (categories W65 through W74) was 38,899 (WHO,
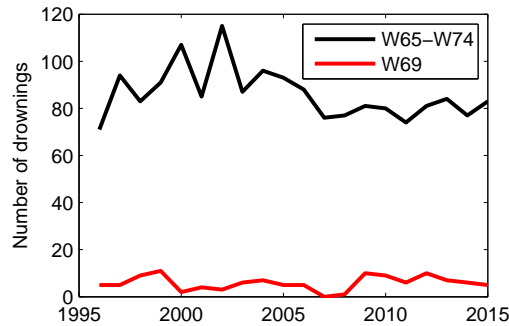
Figure A.1: Total number of reported drownings in The Netherlands between 1996 and 2015 (black line) and contribution of category W69 (drowning and submersion while in natural water, red line).

2017). Since only a limited number of countries reports ICD-10 statistics to WHO, estimates of the global statistics are made as well, albeit on a less specific level. The estimated global number of accidental drownings and submersions in 2015 was 360,000 (WHO, 2016). Assuming that the 29% contribution of category W69 to the total (based on the observations from 2013 presented above) also holds globally, the annual number of accidental drownings and submersions in natural water is 104,400. No data are available to estimate the share of coastal drowning in this number, but it seems safe to state that the annual, global number of coastal drownings is in the order of 10,000.

Many more potential fatalities are prevented by the actions of lifeguards and other rescue services. In Australia, for every case of coastal drowning, 148 people are rescued from the surfzone (Brighton et al., 2013), although the definition of a rescue remains vague. It is assumed that lifeguard activity in Australia is significantly higher than the global average, meaning that the ratio of 148 rescues to 1 fatality will not hold global validity. However, it seems safe to assume a ratio of at least 10, implying a global yearly number of surfzone rescues in the order of 100,000.

A.2. DUTCH STATISTICS

In The Netherlands, ICD-10 mortality data are available from Statistics Netherlands (CBS). The average total number of annual drownings between 1996 and 2015 was 86, with category W69 contributing on average 6 cases to the total (Figure A.1). Again, the share of coastal drowning in category W69 is not documented. Nevertheless, based on an online collection of Dutch drowning-related media messages[1], it is estimated that coastal drowning represents approximately 25% of all drownings in category W69. This leads to an average of 1 to 2 cases of coastal drowning per year in The Netherlands.

For a significant part, this very low number is owed to operations by the Dutch voluntary lifesaving associations, which on average conducted 8625 operations per

---

[1]http://www.verdrinking.nl/, accessed on 7 November 2017

year (304 of which concerned rescue from a life-threatening situation in natural wa-
ter) between 2008 and 2016 (Reddingsbrigade Nederland, 2017).

B

NUMERICAL MODEL

B.1. SETUP OF A COMBINED NUMERICAL WAVE AND CURRENT MODEL

A hydrodynamic model of the Sand Motor was constructed with the modeling suite Delft3D (Lesser et al., 2004), which numerically integrates the shallow water equations. Forcing of the flow by waves was taken into account by solving the wave action balance with the SWAN model (Booij et al., 1999). The main model domain (flow and waves) covers an area of 9.4 x 4.0 km (alongshore x cross-shore) and has a curvi-linear grid that follows the coastline orientation. The spatial extent of the grid is equal to the shaded area in panel B of Figure 4.1. The wave model was nested in a coarse, rectangular model grid with a larger alongshore extent to account for realistic boundary conditions along the lateral boundaries of the detailed model. A grid resolution of 5 m was adopted in the nearshore area in order to accurately represent wave breaking and forcing of wave-driven currents. The time step for numerical integration was 6 seconds.

Tidal currents were forced by varying water levels imposed at the off-shore model boundary. Water level data were obtained from pressure sensors at 6 m water depth, which have been corrected for changes in athmospheric pressure and low-pass filtered with a cut-off period of 15 minutes. A tidal water level gradient was superimposed in alongshore direction, based on gradients predicted by the continental shelf model and nested coastal strip model (Sembiring et al., 2015), which propagate the astronomical tide from the edge of the European continental shelf to the Dutch coast. This approach was shown to yield accurate tidal currents in the shallow coastal waters around the Sand Motor (Radermacher et al., 2017a). Neumann boundary conditions were imposed at the lateral boundaries of the flow model. Friction was specified with the Chézy formulation and a friction coefficient of 50 $m^{1/2}$/s. Horizontal Large Eddy Simulation (HLES, Uittenbogaard and Van Vossen, 2003) was applied for turbulence closure, providing spatially and temporally varying turbulent viscosities with an averaging duration of 30 minutes and a background

viscosity of $0.01 \text{ m}^2/s$.

Parametric boundary conditions for the largest wave grid were obtained from a nearshore waverider buoy at 11 m depth just north of the Sand Motor. Wave conditions were corrected for shoaling and refraction and shifted in time to represent conditions at the off-shore model boundary. Depth-induced wave breaking was accounted for by a combination of the wave energy dissipation formulation by Roelvink (1993) and a roller energy balance (Svendsen, 1984) with breaker parameter $\gamma = 0.8$ and roller slope $\beta = 0.1$.

This model setup is very similar to the approach of Reniers et al. (2007), Reniers et al. (2009) and Reniers et al. (2010), who successfully demonstrated the capability of the Delft3D suite to model nearshore current dynamics.

B.2. COMPARISON TO FIELD OBSERVATIONS

Calculated wave and flow parameters are now compared to quantities observed in the field over a 6-day period in early October 2014 (Figure B.1). Over this period, the wave energy was relatively high and the wave height peaked twice at approximately 1.5 m. This gave rise to distinct wave-driven currents in the nearshore, which makes it a relevant period for model-data comparison in the light of operational forecasts of potentially hazardous currents.

Alongshore currents observed in the field (panel A of Figure B.1) are mostly dominated by the semi-diurnal tidal currents, with positive currents corresponding to flood flow in northeastern direction. Around the second wave energy peak at 7 October, which had more oblique southwesterly waves than the first peak, alongshore wave-driven currents can be seen to dominate the alongshore velocity signal. The numerical model is well-capable of resolving alongshore currents, with very similar performance across all ADCP stations.

Cross-shore currents (panels B-E) exhibit more variability between different stations. During calm conditions, separation of the tidal flow and creation of large-scale tidal eddies causes slight tidal modulations of the cross-shore flow velocity (see Radermacher et al. (2017a) for a more elaborate analysis of tidal currents around the Sand Motor). The two wave energy peaks drive more intense cross-shore currents. The maximum wave height is similar during both peaks, but the first peak is observed to drive less intense cross-shore currents as it coincides with high water. This leads to less intense wave breaking on the subtidal bars and consequently to weaker forcing of nearshore circulations (e.g. Brander, 1999). The modelled cross-shore currents are in reasonable agreement with the field observations, especially in the second half of the comparison period. The overall root-mean-squared error is in the order of 10 cm/s for all stations (Figure B.1). If only periods with high wave energy ($H_{s,obs} > 1$ m) are considered, the RMSE of modeled cross-shore flow velocities is higher (14, 20, 18 and 33 cm/s for stations A4, R1, R2 and B2 respectively). Differences between computed and observed currents are in part attributed to schematisations in the modelling approach, but may also result from slight spatial shifts of modelled flow patterns. The latter is illustrated by a comparison of computed flow fields around ADCP locations A4 and B2 during two events with strong cross-shore currents (Figure B.2).
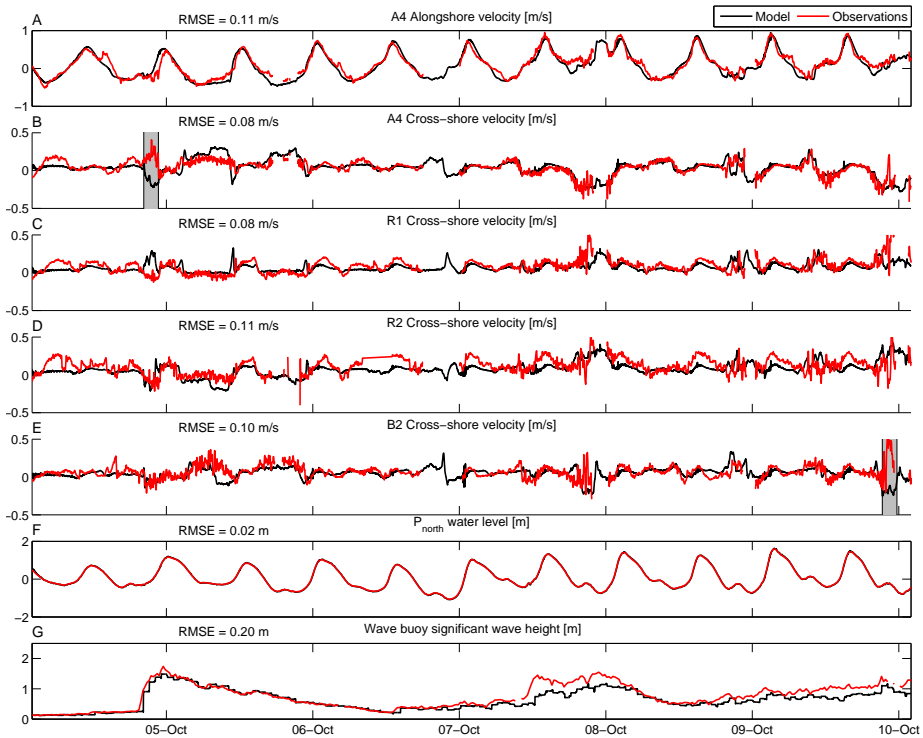
Figure B.1: Comparison of measured (red) and computed (black) flow and wave quantities. The panels show the depth-averaged alongshore velocity component (panel A, positive in flood direction), depth-averaged cross-shore velocity component (panels B-E, positive offshore), water level (panel F) and significant wave height (panel G) at various measurement stations. Shaded periods in panels B and E are analysed in more detail.
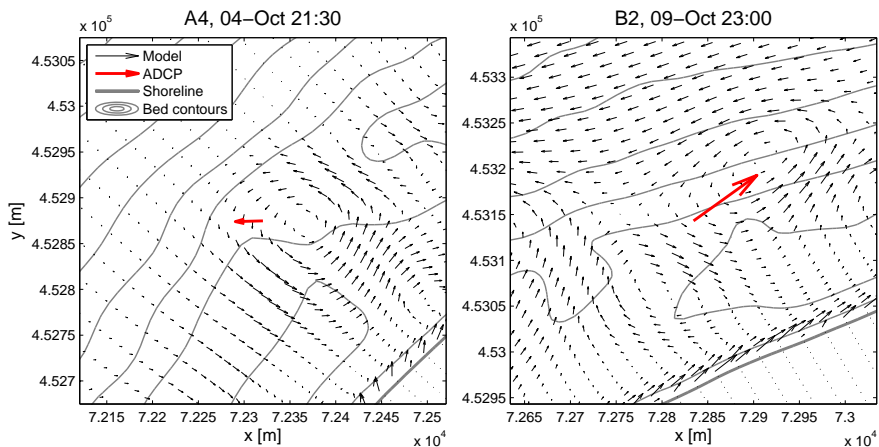

Figure B.2: Computed flow fields and observed local flow velocities at A4 and B2 during two events with strong cross-shore currents. While the model does not match the ADCP observations locally, a spatial shift of the computed flow pattern can explain the differences. Scaling of model and ADCP current vectors is different for optimal visibility. The 0 m MSL bed contour is shown with a thick black line. Thin black lines represent isobaths at 1 m intervals.

REFERENCES

Aagaard, T., Kroon, A., 2007. Mesoscale behaviour of longshore bars - net onshore or net offshore migration, in: Coastal Sediments 07. doi:`10.1061/40926(239)167`.

Aagaard, T., Nielsen, J., Jensen, S.G., Friderichsen, J., 2004. Longshore sediment transport and coastal erosion at Skallingen, Denmark. Danish Journal of Geography 104, 5–14.

Aarninkhof, S.G.J., Ruessink, B.G., Roelvink, J.A., 2005. Nearshore subtidal bathymetry from time-exposure video images. Journal of Geophysical Research 110, C06011. doi:`10.1029/2004JC002791`.

Achete, F., Luijendijk, A., 2012. Applying an analogue for a conceptual model for the development of a mega nourishment, in: Proceedings of ICCE, Santander, Spain.

Aleman, N., Certain, R., Robin, N., Barusseau, J.P., 2017. Morphodynamics of slightly oblique nearshore bars and their relationship with the cycle of net offshore migration. Marine Geology 392, 41 – 52. doi:`https://doi.org/10.1016/j.margeo.2017.08.014`.

Alvarez-Ellacuria, A., Orfila, A., Olabarrieta, M., Medina, R., Vizoso, G., Tintoré, J., 2010. A nearshore wave and current operational forecasting system. Journal of Coastal Research 26, 503–509.

Arozarena, I., Houser, C., Guttiérrez Echeverria, A., Brannstrom, C., 2015. The rip current hazard in Costa Rica. Natural Hazards 77, 753–768.

Arriaga, J., Rutten, J., Ribas, F., Falqués, A., Ruessink, G., 2017. Modeling the long-term diffusion and feeding capability of a mega-nourishment. Coastal Engineering 121, 1 – 13. doi:`https://doi.org/10.1016/j.coastaleng.2016.11.011`.

Attard, A., Brander, R.W., Shaw, W.S., 2015. Rescues conducted by surfers on australian beaches. Accident Analysis & Prevention 82, 70 – 78. doi:`https://doi.org/10.1016/j.aap.2015.05.017`.

Austin, M.J., Masselink, G., Scott, T.M., Russell, P.E., 2014. Water-level controls on macro-tidal rip currents. Continental Shelf Research 75, 28–40.

Austin, M.J., Scott, T.M., Brown, J., MacMahan, J., Masselink, G., Russell, P.E., 2010. Temporal observations of rip current circulation on a macro-tidal beach. Continental Shelf Research 30, 1149–1165.

Austin, M.J., Scott, T.M., Russell, P.E., Masselink, G., 2012. Rip current prediction: development, validation and evaluation of an operational tool. Journal of Coastal Research 29, 283–300.

Balouin, Y., Rey-Valette, H., Picand, P., 2014. Automatic assessment and analysis of beach attendance using video images at the Lido of Sète beach, France. Ocean & Coastal Management 102, 114 – 122. doi:https://doi.org/10.1016/j.ocecoaman.2014.09.006.

Barlas, B., Beji, S., 2016. Rip current fatalities on the Black Sea beaches of Istanbul and effects of cultural aspects in shaping the incidents. Natural Hazards 80, 811–821. doi:10.1007/s11069-015-1998-x.

Beets, D.J., Van der Spek, A.J.F., 2000. The holocene evolution of the barrier and the back-barrier basins of Belgium and The Netherlands as a function of late Weichselian morphology, relative sea-level rise and sediment supply. Netherlands Journal of Geosciences - Geologie en Mijnbouw 79, 3–16. doi:10.1017/S0016774600021533.

Bell, P.S., 1999. Shallow water bathymetry derived from an analysis of X-band marine radar images of waves. Coastal Engineering 37, 513–527.

Benedet, L., Finkl, C.W., Campbell, T., Klein, A., 2004. Predicting the effect of beach nourishment and cross-shore sediment variation on beach morphodynamic assessment. Coastal Engineering 51, 839 – 861. doi:http://dx.doi.org/10.1016/j.coastaleng.2004.07.012.

Bergsma, E.W.J., Conley, D.C., Davidson, M.A., O'Hare, T.J., 2016. Video-based nearshore bathymetry estimation in macro-tidal environments. Marine Geology 374, 31–41.

Black, K.P., Gay, S.L., 1987. Eddy formation in unsteady flows. Journal of Geophysical Research 92, 9514–9522.

Blossier, B., Bryan, K.R., Daly, C.J., Winter, C., 2016. Nearshore sandbar rotation at single-barred embayed beaches. Journal of Geophysical Research: Oceans 121, 2286–2313. doi:10.1002/2015JC011031.

Bogle, J.A., Bryan, K.R., Black, K.P., Hume, T.M., Healy, T.R., 2001. Video observations of rip formation and evolution, in: Proceedings of the International Coastal Symposium 2000, Rotorua, New Zealand.

Bontje, L.E., Slinger, J.H., 2017. A narrative method for learning from innovative coastal projects - Biographies of the Sand Engine. Ocean & Coastal Management 142, 186 – 197. doi:https://doi.org/10.1016/j.ocecoaman.2017.03.008.

Booij, N., Ris, R.C., Holthuijsen, L.H., 1999. A third-generation wave model for coast regions: 1. Model description and validation. Journal of Geophysical Research 104, 7649–7666.

Bosboom, J., Reniers, A.J.H.M., 2014. Scale-selective validation of morphodynamic models, in: Lynett, P.J. (Ed.), Proceedings of 34th Conference on Coastal Engineering, Seoul, South Korea.

Brander, R.W., 1999. Field observations on the morphodynamic evolution of a low-energy rip current system. Marine Geology 157, 199–217.

Brannstrom, C., Trimble, S., Santos, A., Brown, H.L., Houser, C., 2014. Perception of the rip current hazard on Galveston Island and North Padre Island, Texas, USA. Natural Hazards 72, 1123–1138.

Briggs, W.M., Levine, R.A., 1997. Wavelets and field forecast verification. Monthly Weather Review 125, 1329–1341.

Brighton, B., Sherker, S., Brander, R., Thompson, M., Bradstreet, A., 2013. Rip current related drowning deaths and rescues in Australia 2004-2011. Natural Hazards and Earth System Sciences 13, 1069–1075. doi:10.5194/nhess-13-1069-2013.

Brown, J., MacMahan, J., Reniers, A., Thornton, E., 2015. Field observations of surf zone-inner shelf exchange on a rip-channeled beach. Journal of Physical Oceanography 45, 2339–2355.

Bruneau, N., Bertin, X., Castelle, B., Bonneton, P., 2014. Tide-induced flow signature in rip currents on a meso-macrotidal beach. Ocean Modelling 74, 53–59.

Caldwell, N., Houser, C., Meyer-Arendt, K., 2013. Ability of beach users to identify rip currents at Pensacola Beach, Florida. Natural Hazards 68, 1041–1056.

Calvete, D., Dodd, N., Falqués, A., van Leeuwen, S.M., 2005. Morphological development of rip channel systems: Normal and near-normal wave incidence. Journal of Geophysical Research: Oceans 110, n/a–n/a. doi:10.1029/2004JC002803. c10006.

Castelle, B., McCarroll, R.J., Brander, R.W., Scott, T., Dubarbier, B., 2016. Modelling the alongshore variability of optimum rip current escape strategies on a multiple rip-channelled beach. Natural Hazards 81, 663–686.

Castelle, B., Reniers, A., MacMahan, J., 2014. Bathymetric control of surf zone retention on a rip-channelled beach. Ocean Dynamics 64, 1221–1231.

Chandavari, V., Palekar, S., 2014. Diffuser angle control to avoid flow separation. International Journal of Technical Research and Applications 2, 16–21.

Coco, G., Murray, A.B., 2007. Patterns in the sand: From forcing templates to self-organization. Geomorphology 91, 271–290.

Corbella, S., Stretch, D.D., 2012. Predicting coastal erosion trends using non-stationary statistics and process-based models. Coastal Engineering 70, 40 – 49. doi:https://doi.org/10.1016/j.coastaleng.2012.06.004.

Dalrymple, R.A., MacMahan, J.H., Reniers, A.J.H.M., Nelko, V., 2011. Rip currents. Annual Review of Fluid Mechanics 43, 551–581. doi:`10.1146/annurev-fluid-122109-160733`.

Dankert, H., Horstmann, J., Rosenthal, W., 2003. Ocean wind fields retrieved from radar-image sequences. Journal of Geophysical Research 108. doi:`10.1029/2003JC002056`.

De Boer, G.J., Pietrzak, J.D., Winterwerp, J.C., 2006. On the vertical structure of the Rhine region of freshwater influence. Ocean Dynamics 56, 198–216.

De Schipper, M., De Vries, S., Ranasinghe, R., Reniers, A., Stive, M., 2013. Alongshore topographic variability at a nourished beach, in: Proceedings of Coastal Dynamics, Arcachon, France. pp. 499–510.

De Schipper, M.A., De Vries, S., Ruessink, B.G., De Zeeuw, R.C., Rutten, J., Van Gelder-Maas, C., Stive, M.J.F., 2016. Initial spreading of a mega feeder nourishment: Observations of the Sand Engine pilot project. Coastal Engineering 111, 23–38.

De Vriend, H.J., Van Koningsveld, M., Aarninkhof, S.G.J., De Vries, M.B., Baptist, M.J., 2015. Sustainable hydraulic engineering through building with nature. Journal of Hydro-environment Research 9, 159–171.

De Vries, S., Radermacher, M., De Schipper, M.A., Stive, M.J.F., 2015. Tidal dynamics in the Sand Motor lagoon, in: E-proceedings of the 36th IAHR World Congress, The Hague, Netherlands.

De Winter, R.C., Sterl, A., de Vries, J.W., Weber, S.L., Ruessink, G., 2012. The effect of climate change on extreme waves in front of the Dutch coast. Ocean Dynamics 62, 1139–1152. doi:`10.1007/s10236-012-0551-7`.

De Wolf, P., Fransaer, D., Van Sieleghem, J., Houthuys, R., 1993. Morphological trends of the Belgian coast shown by 10 years of remote-sensing based surveying, in: Proceedings of the 8th Symposium on Coastal and Ocean Management.

De Zeeuw, R.C., De Schipper, M.A., De Vries, S., 2017. Sand Motor topographic survey, actual surveyed path. doi:`10.4121/uuid:3836e5a5-4fdf-4122-84bd-a9bb679fb84c`.

De Zeeuw, R.C., De Schipper, M.A., Roelvink, D., De Vries, S., Stive, M.J.F., 2012. Impact of nourishments on nearshore currents and swimmer safety on the Dutch coast, in: Proceedings of ICCE, Santander, Spain.

Dean, R.G., 2002. Beach nourishment: Theory and practice. World Scientific.

Deltacommissie, 2008. Samen werken met water: Een land dat leeft, bouwt aan zijn toekomst. Findings of the 2nd Delta Committee. In Dutch.

Do, A.T.K., De Vries, S., Stive, M.J.F., 2018. Beach evolution adjacent to a seasonally varying tidal inlet in Central Vietnam. Journal of Coastal Research 34, 6–25.

Doody, J.P., 2004. 'Coastal squeeze' - an historical perspective. Journal of Coastal Conservation 10, 129–138.

Driscoll, T.R., Harrison, J.A., Steenkamp, M., 2004. Review of the role of alcohol in drowning associated with recreational aquatic activity. Injury Prevention 10, 107–113. doi:10.1136/ip.2003.004390, arXiv:http://injuryprevention.bmj.com/content/10/2/107.full.pdf.

Dusek, G., Seim, H., 2013. A probabilistic rip current forecast model. Journal of Coastal Research 29, 909–925.

Ebert, E.E., McBride, J.L., 2000. Verification of precipitation in weather system: determination of systematic errors. Journal of Hydrology 239, 179–202.

Elias, E., Walstra, D., Roelvink, J., Stive, M., Klein, M., 2000. Hydrodynamic validation of Delft3D with field measurements at Egmond, in: Proceedings of ICCE 2000.

Elko, N.A., Wang, P., 2007. Immediate profile and planform evolution of a beach nourishment project with hurricane influences. Coastal Engineering 54, 49 – 66. doi:http://dx.doi.org/10.1016/j.coastaleng.2006.08.001.

Escoffier, F.F., 1977. Hydraulics and stability of tidal inlets. Technical Report. US Army Coastal Engineering Research Center.

Ferentinos, G., Collins, M., 1980. Effects of shoreline irregularities on a rectilinear tidal current and their significance in sediment processes. Journal of Sedimentary Petrology 50, 1081–1094.

Finkl, C.W., 1996. What might happen to America's shorelines if artificial beach replenishment is curtailed: A prognosis for Southeastern Florida and other sandy regions along regressive coasts. Journal of Coastal Research 12, III–IX.

Gallop, S.L., Bryan, K.R., Coco, G., 2009. Video observations of rip currents on an embayed beach, in: Proceedings of the 10th International Coastal Symposium, Lisbon, Portugal.

Gallop, S.L., Woodward, E., Brander, R., Pitman, S.J., 2016. Perceptions of rip current myths from the central south coast of England. Ocean & Coastal Management 119, 14–20.

Garnier, R., Calvete, D., Falqués, A., Dodd, N., 2008. Modelling the formation and the long-term behavior of rip channel systems from the deformation of a longshore bar. Journal of Geophysical Research: Oceans 113, n/a–n/a. doi:10.1029/2007JC004632. c07053.

Geyer, W.R., 1993. Three-dimensional tidal flow around headlands. Journal of Geophysical Research 98, 955–966.

Geyer, W.R., Signell, R.P., 1990. Measurements of tidal flow around a headland with a shipboard acoustic doppler current profiler. Journal of Geophysical Research 95, 3198–3197.

Gilleland, E., Ahijevych, D., Brown, B.G., Casati, B., Ebert, E.E., 2009. Intercomparison of spatial forecast verification methods. Weather and Forecasting 24, 1416–1430.

Groeneweg, J., Klopman, G., 1998. Changes of the mean velocity profiles in the combined wave-current motion described in a GLM formulation. Journal of Fluid Mechanics 370, 271–296.

Grunnet, N.M., Ruessink, B., 2005. Morphodynamic response of nearshore bars to a shoreface nourishment. Coastal Engineering 52, 119 – 137. doi:http://dx.doi.org/10.1016/j.coastaleng.2004.09.006.

Guillen, J., García-Olivares, A., Ojeda, E., Osorio, A., Chic, O., González, R., 2008. Long-term quantification of beach users using video monitoring. Journal of Coastal Research 24, 1612–1619.

Gulden, F., 2017. Automatic quantification of beach occupation using oversegmentation and a machine learning framework. Master's thesis. Delft University of Technology. Delft, The Netherlands.

Haller, M.C., Honegger, D., Catalan, P.A., 2014. Rip current observations via marine radar. Journal of Waterway, Port, Coastal and Ocean Engineering 140, 115–124.

Hamm, L., Capobianco, M., Dette, H., Lechuga, A., Spanhoff, R., Stive, M., 2002. A summary of European experience with shore nourishment. Coastal Engineering 47, 237 – 264. doi:http://dx.doi.org/10.1016/S0378-3839(02)00127-8.

Hanson, H., Brampton, A., Capobianco, M., Dette, H., Hamm, L., Laustrup, C., Lechuga, A., Spanhoff, R., 2002. Beach nourishment projects, practices, and objectives - a European overview. Coastal Engineering 47, 81 – 111. doi:https://doi.org/10.1016/S0378-3839(02)00122-9. shore Nourishment in Europe.

Hartmann, D., 2006. Drowning and beach-safety management (BSM) along the Mediterranean beaches of Israel: A long-term perspective. Journal of Coastal Research 22, 1505–1514. doi:10.2112/05-0497.1.

Hayes, M.O., 1980. General morphology and sediment patterns in tidal inlets. Sedimentary Geology 26, 139–156.

Hench, J.L., Luettich Jr, R.A., 2003. Transient tidal circulation and momentum balances at a shallow inlet. Journal of Physical Oceanography 33, 913–932.

Henriquez, M., Reniers, A.J.H.M., Ruessink, G., Stive, M.J.F., 2014. PIV measurements of the bottom boundary layer under nonlinear surface waves. Coastal Engineering 94, 33–46.

Hillen, R., Roelse, P., 1995. Dynamic preservation of the coastline in The Netherlands. Journal of Coastal Conservation 1, 17–28. doi:`10.1007/BF02835558`.

Hino, M., 1974. Theory on formation of rip-current and cuspidal coast, in: Proceedings of the 14th Conference on Coastal Engineering, Copenhagen, Denmark.

Van den Hoek, R.E., Brugnach, M., Mulder, J.P.M., Hoekstra, A.Y., 2014a. Analysing the cascades of uncertainty in flood defence projects: How "not knowing enough" is related to "knowing differently". Global Environmental Change 24, 373–388.

Van den Hoek, R.E., Brugnach, M., Mulder, J.P.M., Hoekstra, A.Y., 2014b. Uncovering the origin of ambiguity in nature-inclusive flood infrastructure projects. Ecology and Society 19. doi:`10.5751/ES-06416-190251`.

Hoekstra, R., Swinkels, C.M., Stengs, B., 2017. Mobile phone application Swimmer Safety: A multi-source information platform to control swimmer safety at the Sandmotor, in: Australasian Coasts and Ports 2017: Working with Nature, Barton, Australia.

Holman, R., 2001. Pattern formation in the nearshore. Springer Berlin Heidelberg, Berlin, Heidelberg. pp. 141–162. doi:`10.1007/978-3-662-04571-8_7`.

Holman, R., Plant, N., Holland, T., 2013. cBathy: A robust algorithm for estimating nearshore bathymetry. Journal of Geophysical Research: Oceans 118, 2595–2609. doi:`10.1002/jgrc.20199`.

Holman, R.A., Stanley, J., 2007. The history and technical capabilities of Argus. Coastal Engineering 54, 477–491.

Holman, R.A., Symonds, G., Thornton, E.B., Ranasinghe, R., 2006. Rip spacing and pesistence on an embayed beach. Journal of Geophysical Research: Oceans 111.

Hoonhout, B., De Vries, S., 2017. Aeolian sediment supply at a mega nourishment. Coastal Engineering 123, 11 – 20. doi:`https://doi.org/10.1016/j.coastaleng.2017.03.001`.

Hoonhout, B., Radermacher, M., Baart, F., van der Maaten, L., 2015. An automated method for semantic classification of regions in coastal images. Coastal Engineering 105, 1 – 12. doi:`https://doi.org/10.1016/j.coastaleng.2015.07.010`.

Houser, C., Arnott, R., Ulzhöfer, S., Barrett, G., 2013. Nearbeach circulation over transverse bar and rip morphology with oblique wave forcing. Earth Surface Processes and Landforms 38, 1269–1279.

Houser, C., Murphy, T., Labude, D., 2015. Alongshore correspondence of beach users and rip channels at Pensacola Beach, Florida. Natural Hazards 78. doi:`10.1007/s11069-015-1804-9`.

Huisman, B., de Schipper, M., Ruessink, B., 2016. Sediment sorting at the Sand Motor at storm and annual time scales. Marine Geology 381, 209 – 226. doi:`http://dx.doi.org/10.1016/j.margeo.2016.09.005`.

Huizer, S., Radermacher, M., De Vries, S., Oude Essink, G.H.P., Bierkens, F.P., 2018. Impact of coastal forcing and groundwater recharge on the growth of fresh groundwater resources in a mega-scale beach nourishment. Hydrology and Earth System Sciences 22, 1065–1080.

IPCC, 2013. Climate change 2013: The physical science basis. Contributions of working group I to the fifth assessment report of the intergovernmental panel on climate change. Cambridge University Press, Cambridge, UK.

Jiménez, J., Osorio, A., Marino-Tapia, I., Davidson, M., Medina, R., Kroon, A., Archetti, R., Ciavola, P., Aarninkhof, S., 2007. Beach recreation planning using video-derived coastal state indicators. Coastal Engineering 54, 507 – 521. doi:https://doi.org/10.1016/j.coastaleng.2007.01.012.

Kalman, R.E., 1960. A New Approach to Linear Filtering and Prediction Problems. Journal of Basic Engineering 82, 35–45.

Kammler, M., Schernewski, G., 2004. Spatial and temporal analysis of beach tourism using webcam and aerial photographs, in: Schernewski, G., Löser, N. (Eds.), Managing the Baltic Sea. Coastline Reports 2.

Kelletat, D., 1992. Coastal erosion and protection measures at the German North Sea Coast. Journal of Coastal Research 8, 699–711.

Kennedy, A.B., Zhang, Y., Haas, K.A., 2008. Rip currents with varying gap widths. Journal of Waterway, Port, Coastal and Ocean Engineering 134, 61–65.

Kim, I.C., Lee, J.I., Lee, J.Y., 2013. Verification of rip current simulation using a two-dimensional predictive model, HAECUM, in: Proceedings 12th International Coastal Symposium (Plymouth, England).

Klein, A.H.F., Mocellim, O., Thadeu de Menezes, J., Berribilli, M., Vintém, G., Dafferner, G., Diehl, F.L., Sperb, R.M., Santana, G.G., 2005. Beach safety management on the coast of Santa Catarina, Brazil. Zeitschrift für Geomorphologie Supplementary Issues 141, 47–58.

Koon, W., Rowhani-Rahbar, A., Quan, L., 2017. The ocean lifeguard drowning prevention paradigm: how and where do lifeguards intervene in the drowning process? Injury Prevention .

Kroon, A., Hoekstra, P., Houwman, K., Ruessink, G., 1994. Morphological monitoring of a shoreface nourishment, NOURTEC experiment at Terschelling, The Netherlands, in: Proceedings of ICCE 1994.

Kuenzer, C., Renaud, F.G., 2012. Climate and environmental change in river deltas globally: Expected impacts, resilience, and adaptation. Springer Netherlands, Dordrecht. pp. 7–46. doi:10.1007/978-94-007-3962-8_2.

Lesser, G.R., Roelvink, J.A., Van Kester, J.A.T.M., Stelling, G.S., 2004. Development and validation of a three-dimensional morphological model. Coastal Engineering 51, 883–915.

Lodder, Q.J., Sørensen, P., 2015. Comparing the morphological behaviour of Dutch-Danish shoreface nourishments, in: Coastal Management: Changing coast, changing climate, changing minds.

Long, J.W., Özkan-Haller, H.T., 2009. Low-frequency characteristics of wave group-forced vortices. Journal of Geophysical Research 114.

Luijendijk, A.P., Ranasinghe, R., de Schipper, M.A., Huisman, B.A., Swinkels, C.M., Walstra, D.J., Stive, M.J., 2017. The initial morphological response of the Sand Engine: A process-based modelling study. Coastal Engineering 119, 1 – 14. doi:http://dx.doi.org/10.1016/j.coastaleng.2016.09.005.

Lushine, J.B., 1991. A study of rip current drownings and related weather factors. National Weather Digest 16, 13–19.

MacMahan, J., Brown, J., Brown, J., Thornton, E., Reniers, A., Stanton, T., Henriquez, M., Gallagher, E., Morrison, J., Austin, M.J., Scott, T.M., Senechal, N., 2010. Mean lagrangian flow behavior on an open coast rip-channeled beach: A new perspective. Marine Geology 268, 1 – 15. doi:https://doi.org/10.1016/j.margeo.2009.09.011.

MacMahan, J.H., 2001. Hydrographic surveying from personal watercraft. Journal of Surveying Engineering 127, 12–24.

MacMahan, J.H., Thornton, E.B., Reniers, A.J.H.M., 2006. Rip current review. Coastal Engineering 53, 191–208.

MacMahan, J.H., Thornton, E.B., Stanton, T.P., Reniers, A.J., 2005. RIPEX: Observations of a rip current system. Marine Geology 218, 113–134. doi:10.1016/j.margeo.2005.03.019.

McCarroll, R.J., Brander, R.W., MacMahan, J.H., Turner, I.L., Reniers, A.J.H.M., Brown, J.A., Bradstreet, A., Sherker, S., 2014. Evaluation of swimmer-based rip current escape strategies. Natural Hazards 71, 1821–1846. doi:10.1007/s11069-013-0979-1.

McCarroll, R.J., Brander, R.W., Scott, T., 2017. Wave height and bathymetric controls on surfzone current velocity and dispersion across an embayed beach, in: Proceedings of Coastal Dynamics 2017, Helsingør, Denmark.

Mil-Homens, J., Ranasinghe, R., Van Thiel de Vries, J.S.M., Stive, M.J.F., 2013. Influence of profile features on longshore sediment transport, in: Proceedings of Coastal Dynamics 2013, Arcachon, France.

Morgan, D., Ozanne-Smith, J., 2013. Surf lifeguard rescues. Wilderness and Environmental Medicine 24, 285–290.

Moulton, M., Elgar, S., Raubenheimer, B., Warner, J.C., Kumar, N., 2017. Rip currents and alongshore flows in single channels dredged in the surf zone. Journal of Geophysical Research: Oceans 122, 3799–3816.

Murphy, A., Epstein, E., 1989. Skill scores and correlation coefficients in model verification. Monthly Weather Review 117, 572–581.

Nolet, C., van Puijenbroek, M., Suomalainen, J., Limpens, J., Riksen, M., 2018. UAV-imaging to model growth response of marram grass to sand burial: Implications for coastal dune development. Aeolian Research 31, 50–61. doi:https://doi.org/10.1016/j.aeolia.2017.08.006.

Nowell, A.R.M., Jumars, P.A., 1984. Flow environments of aquatic benthos. Annual Review of Ecology and Systematics 15, 303–328.

Ojeda, E., Ruessink, B., Guillen, J., 2008. Morphodynamic response of a two-barred beach to a shoreface nourishment. Coastal Engineering 55, 1185 – 1196. doi:http://dx.doi.org/10.1016/j.coastaleng.2008.05.006.

Pattiaratchi, C., James, A., Collins, M., 1986. Island wakes and headland eddies: a comparison between remotely sensed data and laboratory experiments. Journal of Geophysical Research 92, 783–794.

Pingree, R.D., 1978. The formation of the Shambles and other banks by tidal stirring of the seas. Journal of the Marine Biology Association of the United Kingdom 58, 211–226.

Plant, N., Holland, K., Haller, M., 2008. Ocean wavenumber estimation from wave-resolving time series imagery. IEEE Transactions on Geoscience and Remote Sensing 46, 2644–2658. doi:10.1109/TGRS.2008.919821.

Plant, N.G., Aarninkhof, S.G.J., Turner, I.L., Kingston, K.S., 2007. The performance of shoreline detection models applied to video imagery. Journal of Coastal Research 233, 658–670.

Plant, N.G., Edwards, K.L., Kaihatu, J.M., Veeramony, J., Hsu, L., Holland, T.K., 2009. The effect of bathymetric filtering on nearshore process model results. Coastal Engineering 56, 484–493.

Plant, N.G., Holland, K.T., Puleo, J.A., 2002. Analysis of the scale of errors in nearshore bathymetric data. Marine Geology 191, 71–86.

Plant, N.G., Holman, R.A., Freilich, M.H., Birkemeier, W.A., 1999. A simple model for interannual sandbar behavior. Journal of Geophysical Research: Oceans 104, 15755–15776. doi:10.1029/1999JC900112.

Price, T.D., Ruessink, B.G., 2011. State dynamics of a double sandbar system. Continental Shelf Research 31, 659–674.

Radermacher, M., De Schipper, M.A., Price, T.D., Huisman, B.J.A., Aarninkhof, S.G.J., Reniers, A.J.H.M., 2018a. Behaviour of subtidal sandbars in response to nourishments. Geomorphology 313, 1–12.

Radermacher, M., De Schipper, M.A., Reniers, A.J.H.M., 2018b. Sensitivity of rip current forecasts to errors in remotely-sensed bathymetry. Coastal Engineering 135, 66–76.

Radermacher, M., De Schipper, M.A., Reniers, A.J.H.M., Stive, M.J.F., under review. The impact of nearshore hydrodynamics on coastal swimmer safety: A synthesis based on the Sand Motor. Natural Hazards .

Radermacher, M., De Schipper, M.A., Swinkels, C., MacMahan, J.H., Reniers, A.J.H.M., 2017a. Tidal flow separation at protruding beach nourishments. Journal of Geophysical Research: Oceans 122, 63–79.

Radermacher, M., Geerlof, W., De Schipper, M., Huisman, B., Aarninkhof, S., Reniers, A., 2017b. Evolution of alongshore bathymetric variability around a mega-scale beach nourishment, in: Proceedings of Coastal Dynamics 2017, Helsingør, Denmark.

Radermacher, M., Wengrove, M., Van Thiel De Vries, J., Holman, R., 2014. Applicability of video-derived bathymetry estimates to nearshore current model predictions. Journal of Coastal Research 66. doi:10.2112/SI65-xxx.1.

Radermacher, M., Zeelenberg, W., De Schipper, M.A., Reniers, A.J.H.M., 2015. Field observations of tidal flow separation at a mega-scale beach nourishment, in: Proceedings of Coastal Sediments, San Diego, CA, USA.

Ralph, M.E., 1986. Oscillatory flow in wavy-walled tubes. Journal of Fluid Mechanics 168, 515–540.

Reddingsbrigade Nederland, 2017. Jaarverslag 2016: Volle kracht vooruit! in Dutch.

Reniers, A., MacMahan, J., Thornton, E., Stanton, T., 2007. Modeling of very low frequency motions during ripex. Journal of Geophysical Research 112.

Reniers, A.J.H.M., MacMahan, J.H., Beron-Vera, F.J., Olascoaga, M.J., 2010. Rip-current pulses tied to Lagrangian coherent structures. Geophysical Research Letters 37. doi:10.1029/2009GL041443. l05605.

Reniers, A.J.H.M., MacMahan, J.H., Thornton, E.B., Stanton, T.P., Henriquez, M., Brown, J.W., Brown, J.A., Gallagher, E., 2009. Surf zone surface retention on a rip-channeled beach. Journal of Geophysical Research 114.

Reniers, A.J.H.M., Roelvink, J.A., Thornton, E.B., 2004. Morphodynamic modeling of an embayed beach under wave group forcing. Journal of Geophysical Research: Oceans 109. doi:10.1029/2002JC001586. c01030.

Roberts, T.M., Wang, P., 2012. Four-year performance and associated controlling factors of several beach nourishment projects along three adjacent barrier islands, west-central Florida, USA. Coastal Engineering 70, 21 – 39. doi:`http://dx.doi.org/10.1016/j.coastaleng.2012.06.003`.

Roelvink, J.A., 1993. Dissipation in random wave groups incident on a beach. Coastal Engineering 19, 127–150.

RoyalHaskoningDHV, 2013. Evaluatie strand- en zwemveiligheid pilot zandmotor 2012. In Dutch.

RoyalHaskoningDHV, 2014. Evaluatie strand- en zwemveiligheid pilot zandmotor 2013. In Dutch.

RoyalHaskoningDHV, 2015a. Evaluatie strand- en zwemveiligheid pilot zandmotor 2014. In Dutch.

RoyalHaskoningDHV, 2015b. Evaluatie strand- en zwemveiligheid pilot zandmotor 2015. In Dutch.

RoyalHaskoningDHV, 2017. Evaluatie strand- en zwemveiligheid pilot zandmotor 2016. In Dutch.

Ruessink, B., Van der Grinten, R., Vonhögen-Peeters, L., Ramaekers, G., Lodder, Q., 2012. Nearshore evolution at Noordwijk (NL) in response to nourishments, as inferred from Argus video imagery, in: Jubilee Conference Proceedings, NCK-Days 2012.

Ruessink, B., Kroon, A., 1994. The behaviour of a multiple bar system in the nearshore zone of Terschelling, the Netherlands: 1965-1993. Marine Geology 121, 187 – 197. doi:`http://dx.doi.org/10.1016/0025-3227(94)90030-2`.

Ruessink, B., Pape, L., Turner, I., 2009. Daily to interannual cross-shore sandbar migration: Observations from a multiple sandbar system. Continental Shelf Research 29, 1663 – 1677. doi:`http://dx.doi.org/10.1016/j.csr.2009.05.011`.

Ruessink, B.G., Miles, J.R., Feddersen, F., Guza, R.T., Elgar, S., 2001. Modeling the alongshore current on barred beaches. Journal of Geophysical Research 106, 22451–22463.

Ruessink, B.G., Wijnberg, K.M., Holman, R.A., Kuriyama, Y., van Enckevort, I.M.J., 2003. Intersite comparison of interannual nearshore bar behavior. Journal of Geophysical Research: Oceans 108. doi:`10.1029/2002JC001505`. 3249.

Rutten, J., De Jong, S.M., Ruessink, G., 2017a. Accuracy of nearshore bathymetry inverted from X-band radar and optical video data. IEEE Transactions on Geoscience and Remote Sensing 55, 1106–1116.

Rutten, J., Dubarbier, B., Price, T., B, C., Ruessink, G., 2017b. Crescentic bar patterns along curved coasts: observations and modelling, in: Proceedings of Coastal Dynamics 2017, Helsingør, Denmark.

Rutten, J., Ruessink, B.G., Price, T.D., 2017c. Observations on sandbar behaviour along a man-made curved coast. Earth Surface Processes and Landforms doi:`10.1002/esp.4158`. esp.4158.

Scott, T., Austin, M., Masselink, G., Russell, P., 2016. Dynamics of rip currents associated with groynes — field measurements, modelling and implications for beach safety. Coastal Engineering 107, 53 – 69. doi:`https://doi.org/10.1016/j.coastaleng.2015.09.013`.

Scott, T., Masselink, G., Austin, M.J., Russell, P., 2014. Controls on macrotidal rip current circulation and hazard. Geomorphology 214, 198–215.

Scott, T.M., 2009. Beach morphodynamics and associated hazards in the UK. Ph.D. thesis. University of Plymouth.

Sembiring, L., Van Dongeren, A., Winter, G., Van Ormondt, M., Briere, C., Roelvink, D., 2014. Nearshore bathymetry from video and the application to rip current predictions for the Dutch coast, in: Green, A.N., Cooper, J.A.G. (Eds.), Proceedings 13th International Coastal Symposium, Durban, South Africa.

Sembiring, L., Van Ormondt, M., Van Dongeren, A., Roelvink, D., 2015. A validation of an operational wave and surge prediction system for the Dutch coast. Natural Hazards and Earth System Sciences 15, 1231–1242.

Senet, C.M., Seemann, J., Flampouris, S., Ziemer, F., 2008. Determination of bathymetric and current maps by the method DiSC based on the analysis of nautical X-band radar image sequences of the sea surface. IEEE Transactions on Geoscience and Remote Sensing 46, 2267–2279.

Shand, R., Bailey, D., 1999. A review of net offshore bar migration with photographic illustrations from Wanganui, New Zealand. Journal of Coastal Research 15, 365–378.

Shand, R.D., 2003. Relationships between episodes of bar switching, cross-shore bar migration and outer bar degeneration at Wanganui, New Zealand. Journal of Coastal Research 19, 157–170.

Sherker, S., Williamson, A., Hatfield, J., Brander, R., Hayen, A., 2010. Beachgoers' beliefs and behaviours in relation to beach flags and rip currents. Accident analysis and prevention 42, 1785–1804.

Short, A.D., 1992. Beach systems of the central Netherlands coast: Processes, morphology and structural impacts in a storm driven multi-bar system. Marine Geology 107, 103 – 137. doi:`http://dx.doi.org/10.1016/0025-3227(92)90071-O`.

Short, A.D., 2006. Australian beach systems: Nature and distribution. Journal of Coastal Research 22, 11–27. doi:`10.2112/05A-0002.1`.

Short, A.D., Aagaard, T., 1993. Single and multi-barred beach change models. Journal of Coastal Research SI 15, 141–157.

Signell, R.P., Geyer, W.R., 1990. Numerical simulation of tidal dispersion around a coastal headland, in: Cheng, R.T. (Ed.), Residual Currents and Long-term Transport. Springer-Verlag. volume 38 of *Coastal and Estuarine Studies*.

Signell, R.P., Geyer, W.R., 1991. Transient eddy formation around headlands. Journal of Geophysical Research 96, 2561–2575.

Simpson, R.L., 1989. Turbulent boundary-layer separation. Annual Review of Fluid Mechanics 21, 205–234.

Sobey, I.J., 1983. The occurrence of separation in oscillatory flow. Journal of Fluid Mechanics 134, 247–257.

Southgate, H.N., 2011. Data-based yearly forecasting of beach volumes along the Dutch North Sea coast. Coastal Engineering 58, 749 – 760. doi:`http://dx.doi.org/10.1016/j.coastaleng.2011.03.011`.

Souza, A.J., Simpson, J.H., 1997. Controls on stratification in the Rhine ROFI system. Journal of Marine Systems 12, 311–323.

Stive, M.J., Nicholls, R.J., de Vriend, H.J., 1991. Sea-level rise and shore nourishment: a discussion. Coastal Engineering 16, 147 – 163. doi:`https://doi.org/10.1016/0378-3839(91)90057-N`.

Stive, M.J.F., De Schipper, M.A., Luijendijk, A.P., Aarninkhof, S.G.J., Van Geldermaas, C., Van Thiel De Vries, J.S.M., De Vries, S., Henriquez, M., Marx, S., Ranasinghe, R., 2013. A new alternative to saving our beaches from sea-level rise: The Sand Engine. Journal of Coastal Research 29, 1001–1008. doi:`10.2112/JCOASTRES-D-13-00070.1`.

Svendsen, I.A., 1984. Wave heights and set-up in a surf zone. Coastal Engineering 8, 303–329.

Talstra, H., 2011. Large-scale turbulence structures in shallow separating flows. Ph.D. thesis. Delft University of Technology. Delft, Netherlands.

Temmerman, S., Meire, P., Bouma, T.J., Herman, P.M.J., Ysebaert, T., De Vriend, H.J., 2013. Ecosystem-based coastal defence in the face of global change. Nature 504, 79–83.

Thiébot, J., Idier, D., Garnier, R., Falqués, A., Ruessink, B., 2012. The influence of wave direction on the morphological response of a double sandbar system. Continental Shelf Research 32, 71 – 85. doi:`http://dx.doi.org/10.1016/j.csr.2011.10.014`.

Thornton, E., MacMahan, J., Sallenger, A., 2007. Rip currents, mega-cusps, and eroding dunes. Marine Geology 240, 151 – 167. doi:`https://doi.org/10.1016/j.margeo.2007.02.018`.

Tipton, M., Golden, F., 2006. The physiology of cooling in cold water, in: Bierens, J.J.L.M. (Ed.), Handbook on Drowning, pp. 485–490.

Tomczak, M., 1988. Island wakes in deep and shallow water. Journal of Geophysical Research 93, 5153–5154.

Tonnon, P.K., Briere, C., 2011. Memo 1002337-002-ZKS-0001: wave look-up table. Technical Report. Deltares.

Trygonis, V., Ghionis, G., Andreadis, O., Vousdoukas, M., Ntemogiannis, I., Rigos, A., Psarros, F., Velegrakis, A., Hasiotis, T., Poulos, S.E., 2015. Monitoring beach usage with a coastal video imaging system: an application at Paralia Katerinis, Greece, in: Proceedings of the 11th Panhellenic Symposium on Oceanography and Fisheries.

Tătui, F., Vespremeanu-Stroe, A., Ruessink, G.B., 2016. Alongshore variability of cross-shore bar behavior on a nontidal beach. Earth Surface Processes and Landforms 41, 2085–2097. doi:`10.1002/esp.3974`. esp.3974.

Uittenbogaard, R.E., Van Vossen, B., 2003. Subgrid-scale model for quasi-2d turbulence in shallow water, in: Uijttewaal, W.S.J., Jirka, G.H. (Eds.), Reserach presented at the international symposium on shallow flows, Taylor & Francis, Delft, Netherlands.

Van Dalfsen, J.A., Aarninkhof, S.G.J., 2009. Building with Nature: Mega nourishments and ecological landscaping of extraction areas, in: Proceedings of the European Marine Sand and Gravel Group Conference, Rome, Italy.

Van Dongeren, A.R., Plant, N.G., Cohen, A., Roelvink, J.A., Haller, M.C., Catalan, P., 2008. Beach Wizard: nearshore bathymetry estimation through assimilation of model computations and remote observations. Coastal Engineering 55, 1016–1027.

Van Duin, M., Wiersma, N., Walstra, D., Van Rijn, L., Stive, M., 2004. Nourishing the shoreface: observations and hindcasting of the Egmond case, The Netherlands. Coastal Engineering 51, 813 – 837. doi:`http://dx.doi.org/10.1016/j.coastaleng.2004.07.011`.

Van Enckevort, I., Ruessink, B., 2003. Video observations of nearshore bar behaviour. Part 2: Alongshore non-uniform variability. Continental Shelf Research 23, 513 – 532. doi:`http://dx.doi.org/10.1016/S0278-4343(02)00235-2`.

Van Leeuwen, B.R., McCarroll, J., Brander, R.W., Turner, I.L., Power, H.E., Bradstreet, A.J., 2016. Examining rip current escape strategies in non-traditional beach morphologies. Natural Hazards 81, 145–165.

Van Rijn, L.C., 1997. Sediment transport and budget of the central coastal zone of holland. Coastal Engineering 32, 61–90.

Voulgaris, G., Kumar, N., Warner, J.C., 2011. Prediction of rip currents using a three-dimensional numerical, coupled, wave current model, in: Leatherman, S., Fletemeyer, J. (Eds.), Rip Currents: Beach Safety, Physical Oceanography, and Wave Modeling, CRC Press. pp. 87–105.

Walstra, D., Reniers, A., Ranasinghe, R., Roelvink, J., Ruessink, B., 2012. On bar growth and decay during interannual net offshore migration. Coastal Engineering 60, 190 – 200. doi:`http://dx.doi.org/10.1016/j.coastaleng.2011.10.002`.

Walstra, D., Wesselman, D., Van der Deijl, E., Ruessink, B.G., 2016. On the intersite variability in inter-annual nearshore sandbar cycles. Journal of Marine Science and Engineering 4.

Walstra, D.J.R., Ruessink, B.G., Reniers, A.J.H.M., Ranasinghe, R., 2015. Process-based modeling of kilometer-scale alongshore sandbar variability. Earth Surface Processes and Landforms 40, 995–1005. doi:`10.1002/esp.3676`. eSP-14-0029.R2.

Wengrove, M.E., Henriquez, M., De Schipper, M.A., Holman, R.A., Stive, M.J.F., 2013. Monitoring morphology of the Sand Engine leeside using Argus' cBathy, in: Proceedings of Coastal Dynamics 2013, Archachon, France.

WHO, 2016. Global Health Estimates 2015: Deaths by cause, age, sex, by country and by region, 2000-2015.

WHO, 2017. Mortality Database. Accessed 7 November 2017.

Wijnberg, K.M., 2002. Environmental controls on decadal morphologic behaviour of the Holland coast. Marine Geology 189, 227 – 247. doi:`http://dx.doi.org/10.1016/S0025-3227(02)00480-2`.

Wijnberg, K.M., Wolf, F., 1994. Three-dimensional behaviour of a multiple bar system, in: Proceedings of Coastal Dynamics 94.

Wilmink, R.J.A., Lodder, Q.J., Sørensen, P., 2017. Assessment of the design and behaviour of nourishments in the North Sea region. Towards an NSR guideline for nourishments, in: Proceedings of Coastal Dynamics 2017, Helsingør, Denmark.

Wilson, G.W., Özkan-Haller, H.T., Holman, R.A., 2013. Quantifying the length-scale dependence of surf zone advection. Journal of Geophysical Research: Oceans 118, 2393–2407. doi:`10.1002/jgrc.20190`.

Wingeart, K.M., Herbers, T.H.C., O'Reilly, W.C., Wittmann, P.A., Jensen, R.E., Tolman, H.L., 2001. Validation of operational global wave prediction models with spectral buoy data, in: Proceedings of the Fourth International Symposium on Ocean Wave Measurement and Analysis. doi:`10.1061/40604(273)61`.

Winter, G., Van Dongeren, A.R., De Schipper, M.A., van Thiel de Vries, J., 2014. Rip currents under obliquely incident wind waves and tidal longshore currents. Coastal Engineering 89, 106–119. doi:10.1016/j.coastaleng.2014.04.001.

Wolanski, E., Imberger, J., Heron, M.L., 1984. Island wakes in shallow coastal waters. Journal of Geophysical Research 89, 10553–10569.

Woodward, E., Beaumont, E., Russell, P., Wooler, A., Macleod, R., 2013. Analysis of rip current incidents and victim demographics in the UK, in: Proceedings of the 12th International Coastal Symposium, Plymouth, UK.

Wright, L., Short, A., 1984. Morphodynamic variability of surf zones and beaches: A synthesis. Marine Geology 56, 93 – 118. doi:http://dx.doi.org/10.1016/0025-3227(84)90008-2.

Yates, M., Guza, R., O'Reilly, W., Seymour, R., 2009. Seasonal persistence of a small southern California beach fill. Coastal Engineering 56, 559 – 564. doi:http://dx.doi.org/10.1016/j.coastaleng.2008.11.004.

ACKNOWLEDGEMENTS

So I have come to the end of an inspiring, challenging, entertaining and at times tough period. Engaging in Ph.D. research has turned out to be the best decision I could have made 5 years ago. I thank Lynyrd de Wit and Han Winterwerp for motivating me to take this step, Mark Klein for bringing the NatureCoast vacancy to my attention and Stefan Aarninkhof for turning my M.Sc. graduation presentation into a job application. STW and all NatureCoast partners are gratefully acknowledged for enabling me to work on this thesis.

Matthieu, I am indebted to you for your committed supervision. This thesis and myself have greatly benefited from your truly academic nature (persevering, knowledgeable, energetic, motivating, critical and finally wearing professor glasses). I enjoyed having you as a supervisor and close colleague, hopefully I will find a good excuse to keep visiting the TU every now and then! Ad, if a distant authority in your research field suddenly moves over to Delft and becomes your promotor, you can only feel very lucky. It has been a great pleasure to work with you in the office and in the field, thank you for your guidance and inspiration. Marcel, the freedom you gave me to explore my interests and your infinite trust in my work (as a promotor and a true WaveDroid fan) are greatly appreciated and form an important contribution to my professional development. Jaap, it is a pity that I could only enjoy your presence at the department for a few months. Thank you for kick-starting my research and turning a bunch of young, enthusiastic researchers into a professional brotherhood. Many others are thanked for their major and minor contributions to this thesis: Rob Holman, Tim Price, Harmen Talstra, Stefan Aarninkhof, Jantien Rutten, Cilia Swinkels (for bringing some odd South-African current meters to my attention), Jamie MacMahan, Ap van Dongeren, Dirk Jan Walstra, Greg Wilson, Laurens van der Maaten, Fedor Baart, Ben Girwar, Yeow Chong Tan, Wilmar Zeelenberg, Wessel Geerlof, Freek Gulden and the entire MegaPEX field crew.

Without an enjoyable working environment, 4.5 years of research would have been unbearable. Bas[2] and Saulo, sharing an office with the NEMO brotherhood as an adopted son for almost 4 years has been an unforgettable experience. Although the number of generated ideas and plans (in-office face recognition system, cycling to England, running from coast to coast, Burgundian lunch, beer o'clock, etc.) always exceeded the amount of time we had available, you gave me a lot of fun, inspiration and motivation. I am looking forward to the day we can have a beer as the NEMO doctorhood! Sierd, thank you for all the serious and not-so-serious discussions over lunch, coffee, beer and 4 o'clock choco'tjes. Please keep surprising and inspiring the academic environment with bold statements and unconventional ideas. I also thank all other colleagues, near and far, for some enjoyable years: Arjen Luijendijk, Meagan Wengrove, Caroline Fredriksson, the NatureCoast Ph.D.s and post-docs, Joep van der Zanden, Johan Reyns, Ronald Brouwer, Martijn Henriquez,

ABOUT THE AUTHOR

Max Radermacher was born on November 29, 1987 in Meerssen, The Netherlands. He grew up in Maastricht and received secondary education at Sint-Maartenscollege (gymnasium), graduating mid-2006. Driven by his interest in engineering, infrastructure and geophysics, he entered the Civil Engineering B.Sc. programme at Delft University of Technology in September 2006. Gradually, he obtained a passion for the fields of coastal engineering and environmental fluid mechanics, which became his focus from September 2010 onwards in the Civil Engineering M.Sc. programme at the same university. Max graduated in January 2013 (cum laude) on a study regarding the efficiency of silt curtains under supervision of prof. Han Winterwerp. His graduation study won him the 'Young Author Award' at the 20th World Dredging Congress in Brussels, Belgium in June 2013.

Motivated by his M.Sc. thesis supervisors, he applied for a Ph.D. position at Delft University under supervision of prof. Marcel Stive in the extensive, multidisciplinary NatureCoast program. Starting in May 2013, he studied the impact of sand nourishments on nearshore hydrodynamics and swimmer safety, with a strong focus on the Sand Motor mega nourishment at the Dutch North Sea coast. The Ph.D. program offered him the opportunity to get acquainted with field measurements, numerical modelling and advanced data analysis techniques. During his 4.5-year contract, he (co-)supervised more than 10 student projects (both at M.Sc. and B.Sc. level) and was involved in pioneering the development of open online education at the department of Hydraulic Engineering.

During the MegaPEX field experiment in fall 2014, Max met Zane Thackeray, a South African geologist, inventor and entrepreneur. Together they invented, tested and commercialised the WaveDroid, a low-cost directional wave measurement buoy based on modern smartphone technology. This led to the establishment of H-max in 2015, a company focusing on marine measurements and experimental development. With the continuous development of WaveDroid and other measurement platforms, H-max has been growing steadily and is the main occupation of Max after obtaining his Ph.D. degree in 2018.

PUBLICATIONS

FIRST AUTHOR PUBLICATIONS

JOURNAL ARTICLES

M. Radermacher, M. Wengrove, J. van Thiel de Vries, R. Holman, (2014). *Applicability of video-derived bathymetry estimates to nearshore current model predictions*, Journal of Coastal Research **SI70**, 290-295.

M. Radermacher, L. de Wit, J.C. Winterwerp, W.S.J. Uijttewaal, (2015). *Efficiency of hanging silt curtains in crossflow*, Journal of Waterway, Port, Coastal, and Ocean Engineering **142** (1), 04015008.

M. Radermacher, M.A. de Schipper, C. Swinkels, J.H. MacMahan, A.J.H.M. Reniers, (2017). *Tidal flow separation at protruding beach nourishments*, Journal of Geophysical Research: Oceans **122** (1), 63-79.

M. Radermacher, M.A. de Schipper, A.J.H.M. Reniers, (2018). *Sensitivity of rip current forecasts to errors in remotely-sensed bathymetry*, Coastal Engineering **135**, 66-76.

M. Radermacher, M.A. de Schipper, T.D. Price, B.J.A. Huisman, S.G.J. Aarninkhof, A.J.H.M. Reniers, (2018). *Behaviour of subtidal sandbars in response to nourishments*, Geomorphology **313**, 1-12.

M. Radermacher, M.A. de Schipper, A.J.H.M. Reniers, M.J.F. Stive (*under review*). *The impact of nearshore hydrodynamics on coastal swimmer safety: A synthesis based on the Sand Motor*, Submitted to Natural Hazards.

CONFERENCE PROCEEDINGS

M. Radermacher, F. Van der Goot, D. Rijks, L. De Wit, (2013). *The art of screening: Effectiveness of silt screens*, in: Proceedings of WODCON XX: "The Art of Dredging" - 2013, Brussels, Belgium.

M. Radermacher, W. Zeelenberg, M. de Schipper, A. Reniers, (2015). *Field observations of tidal flow separation at a mega-scale beach nourishment*, in: Proceedings of Coastal Sediments 2015, San Diego (CA), USA.

M. Radermacher, Z.H. Thackeray, M.A. de Schipper, L. Gordon, C. Chrystal, R. Leuci, A.J.H.M. Reniers, (2015). *Tilt current meter array: Field validation*, in: E-proceedings of the 36th IAHR World Congress, The Hague, The Netherlands.

M. Radermacher, W. Geerlof, M.A. de Schipper, B.J.A. Huisman, S.G.J. Aarninkhof, A.J.H.M. Reniers, (2017). *Evolution of alongshore bathymetric variability around a mega-scale beach nourishment*, in: Proceedings of Coastal Dynamics 2017, Helsingør, Denmark.

CO-AUTHORED PUBLICATIONS

JOURNAL ARTICLES

L. Cutroneo, F. van der Goot, A. Roels, M. Castellano, **M. Radermacher**, S. Tucci, P. Povero, G. Canepa, M. Capello, (2014). *A check on the efficiency of an air-bubble screen using acoustic measurements and an artificial tracer*, Journal of Soils and Sediments **14** (9), 1626-1637.

B.M. Hoonhout, **M. Radermacher**, F. Baart, L.J.P. van der Maaten, (2015). *An automated method for semantic classification of regions in coastal images*, Coastal Engineering **105**, 1-12.

S. Huizer, **M. Radermacher**, S. de Vries, G.H.P. Oude Essink, M.F.P. Bierkens, (2018). *Impact of coastal forcing and groundwater recharge on the growth of fresh groundwater resources in a mega-scale beach nourishment*, Hydrology and Earth System Sciences **22**, 1065-1080.

CONFERENCE PROCEEDINGS

S. de Vries, **M. Radermacher**, M.A. de Schipper, M.J.F. Stive, (2015). *Tidal dynamics in the Sand Motor lagoon*, in: E-proceedings of the 36th IAHR World Congress, The Hague, The Netherlands.

B.J.A. Huisman, A. Vargas Solis, M.A. de Schipper, **M. Radermacher**, R. Ranasinghe, (2017). *Impact of beach states on alongshore transport*, in: Proceedings of Coastal Dynamics 2017, Helsingør, Denmark.